3D Simulation of Solar Cells with Integration of Optical Nanoantennas

Inês Margarida Pinheiro Caetano

Thesis to obtain the Master of Science Degree in

Electrical and Computer Engineering

Supervisor: Professor João Paulo Neto Torres

Examination Committee

Chairperson: Professor Francisco André Corrêa Alegria

Supervisor: Professor João Paulo Neto Torres

Members of the committee: Professor Carlos Alberto Ferreira Fernandes

January 2021

Declaration: I declare that this document is an original work of my own authorship and that it fulfills all the requirements of the Code of Conduct and Good Practices of the Universidade de Lisboa.

Declaração: Declaro que o presente documento é um trabalho original da minha autoria e que cumpre todos os requisitos do Código de Conduta e Boas Práticas da Universidade de Lisboa.

Acknowledgments

First, I would like to deeply thank my family for all the support, words of encouragement and advices. In particular, I would like to thank my mother, Alda Luísa Pinheiro, for all the affection and life teachings. For always believing in me, supporting my choices, and inspiring me every day to be and do better.

Secondly, I would like to thank all my colleagues and friends that I have met over the past five years, during my journey at Instituto Superior Técnico. Without their help I would not be able to reach this final goal. Thank you for the friendship and all the good times.

To my supervisor and mentor, Professor João Paulo Neto Torres, I want to express my deep gratitude for all the support and encouragement during the development of this dissertation. For always being available to help and offer guidance and motivation, providing me with all the conditions to successfully complete this work. Additionally, I want to thank Ricardo Lameirinhas, for his willingness to help, guide me through complex concepts and in solving some of the problems and setbacks that appeared during the development of this dissertation.

I would especially like to thank my boyfriend, Francisco Martins, for the endless support, patience, and friendship. For always sticking by my side, through my best and worst moments.

To all, I express my deepest and sincerest thank you.

Abstract

The evolution of nanotechnology has provided a better understanding of light-matter interaction at a subwavelength scale and has led to the development of new devices that can possibly play an important role in future applications in various fields. Nanoantennas are a prime example of such devices, having gained considerable interest in recent years for their application in the field of photovoltaic technology at visible and infrared wavelengths, due to their ability of capturing and confining energy of free-propagating waves. Some of these devices feature apertures and can benefit from unique optical properties related to the phenomenon of extraordinary optical transmission (EOT) where, due to resonant behavior, light passing through subwavelength apertures in a metal film can be transmitted in greater orders of magnitude than that predicted by classical aperture theory. Nevertheless, the successful implementation of such devices for photovoltaic applications is yet to be achieved.

During this dissertation, different 2D and 3D models featuring a metallic nanoantenna array with subwavelength holes coupled to a photovoltaic cell, are simulated using *COMSOL Multiphysics*®. These models present slight variations between them, such as the position of the nanoantenna within the structure, the geometry of the holes of the nanoantenna and type of solar cell.

The results ultimately demonstrate that the coupling of nanoantennas to solar cells can indeed be advantageous and improve the capture and absorption of solar energy by the cells.

Keywords: apertures; nanoantenna; photovoltaic; solar cells; subwavelength structures.

Resumo

A evolução da nanotecnologia tem vindo a proporcionar uma melhor compreensão da interação luz-matéria a uma escala nanométrica, e levou também ao desenvolvimento de novos dispositivos que podem vir a desempenhar um papel importante em aplicações futuras nas mais variadas áreas. As nanoantenas constituem um bom exemplo de tais dispositivos, sendo que a sua aplicação na área da tecnologia fotovoltaica, nas regiões do visível e infravermelho, tem vindo a despertar grande interesse nos últimos anos, devido à sua capacidade de capturar e confinar radiação eletromagnética. Alguns destes dispositivos apresentam determinadas aberturas e podem beneficiar de propriedades óticas relacionadas com o fenômeno de transmissão ótica extraordinária, do inglês *extraordinary optical transmission* (EOT), onde, devido a comportamentos ressonantes, a luz que passa por aberturas muito menores que o comprimento de onda da luz incidente, localizadas numa superfície de metal, pode ser transmitida em ordens de grandeza maiores que aquelas previstas pelas teorias clássicas de difração da luz. No entanto, a implementação de nanoantenas em aplicações fotovoltaicas ainda não foi alcançada com sucesso.

Ao longo desta dissertação são simulados diferentes modelos 2D e 3D de uma nanoantena metálica com buracos cilíndricos integrada numa célula fotovoltaica, recorrendo ao *COMSOL Multiphysics®.* Os modelos apresentam ligeiras alterações entre si, como a posição da nanoantena na estrutura, a geometria das aberturas da nanoantena e o tipo de célula solar.

Em última análise, os resultados demonstram que o acoplamento de nanoantenas a células solares pode de facto ser vantajoso e originar melhorias na captação e absorção de energia solar pelas células.

Palavras-chave: aberturas; células solares; estruturas nanométricas; fotovoltaicos; nanoantena.

Contents

List of figures

Acronyms

AC Alternating Current

Al Aluminium

a-Si Amorphous Silicon

Cds Cadmium Sulphide

CdTe Cadmium Telluride

CIGS Copper Indium Gallium Selenide

CPV Concentrator photovoltaics

DC Direct Current

EM Electromagnetic

EU European Union

EOT Extraordinary Optical Transmission

FEM Finite Element Method

GaAs Gallium Arsenide

IR Infrared

LSP Localized Surface Plasmon

MIM Metal-Insulator-Metal

MIIM Metal Multi-insulator Metal

NFO Near Field Optics

OPV Organic photovoltaics

PDE Partial Differential Equation

PV Photovoltaic

RF Radiofrequency

SPP Surface Plasmon Polariton

UV Ultraviolet

ZnO Zinc Oxide

1. Introduction

1.1. Motivation

Energy demand has been steadily increasing since the Industrial Revolution and it will continue to increase, as illustrated in figure 1.1, specially in non-OECD [1] countries, which will experience the biggest population growth accompanied by a rise in industrialization.

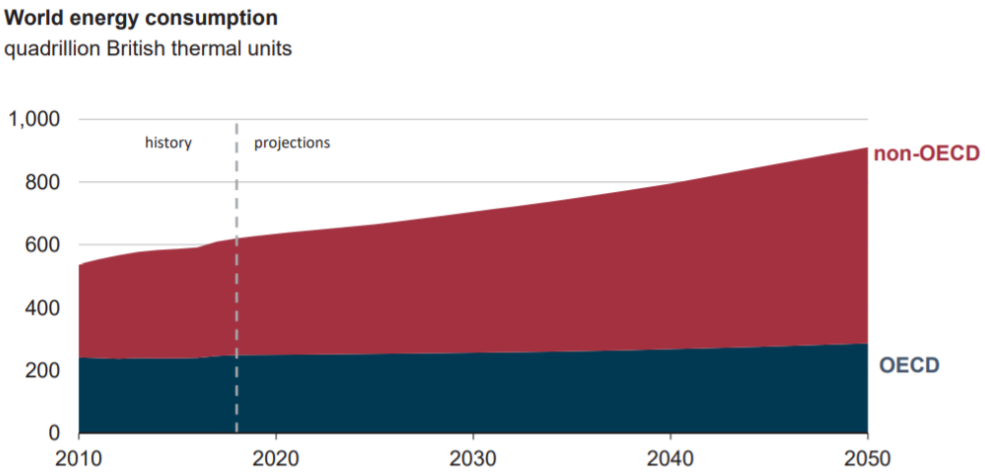

Figure 1. 1 - World energy consumption (Adapted from [1]).

Although renewable energy use is increasing globally, as of 2018 these sources of energy only accounted for less than 20% of the world's primary energy consumption [1]. Fossil fuels such as oil, coal and natural gas still meet much of the world's energy demand. These resources are limited and, with the ongoing increase in the global energy demand, will eventually be drained. Additionally, the use of fossil fuels has an extremely negative environmental impact.

Concerns over climate change and the energy demand of a rapidly growing global population, require an urgent shift towards renewable resources for energy production. Renewables are forecast to become the leading source of primary energy consumption by 2050, with wind and solar representing 70% of total renewables generation [1].

Solar panel technology has evolved from a small scale market to a mainstream electricity source. Improvements made to the technology over the years led the associated costs to decline. Nowadays, photovoltaic (PV) cells can make a direct conversion of the power associated with solar radiation into DC electric power, at a relatively low cost. In addition, the

[1] OECD stands for Organisation for Economic Co-operation and Development and it is an intergovernmental economic organisation with 37 member countries that aims to stimulate economic progress and world trade. Most developing countries are not part of the OECD.

fact that PV cells are robust structures that require very little maintenance makes them an extremely attractive technology that is rapidly expanding on the global energy market [2].

However, PV solar cells have some limitations. Only a small fraction of the incoming solar radiation can be converted to electricity by semiconductors due to the materials characteristics and electrical properties. The remaining radiation, although absorbed by the cell, it is converted into heat [3].

Even though many research efforts have been put into place in order to improve efficiency rates of PV solar panels, the optimization of these efficiency rates has yet to be achieved. Most panels present efficiency rates of around 20% or less, usually requiring a mechanical sun-tracking system to optimize conversion. Nanotechnology can be part of the solution to this problem [3].

The field of nanotechnology and optical materials has experienced a rapid advancement which has led to the emergence and development of new systems and devices, like the nanoantenna. With the implementation of this technology, PV solar devices are expected to become more efficient and inexpensive [4].

In this dissertation the use of nanotechnology in photovoltaics is going to be studied by analysing and evaluating the impact that the coupling of a nanoantenna to a solar cell has in the cell's output optical response.

1.2. Photovoltaic Technologies

Photovoltaic cells or solar cells are devices that convert incoming solar radiation into electricity by exploiting the photovoltaic effect, a phenomenon which induces an electric voltage between two electrodes attached to a material when the system is exposed to light [5].

The commercially predominant solar cells are wafer-based cells, accounting for more than 85% of the world photovoltaic market. Crystalline silicon cells (c-Si) are one of the forms of wafer-based technology. These are classified as first-generation solar cells which includes monocrystalline silicon (m-Si) cells, polycrystalline silicon (p-Si) cells, as well as gallium arsenide (GaAs) cells [6]. First generation cells are the oldest and, although they are still relatively expensive to produce, remain the most widely used type of solar cells. The use of silicon on solar cells is prevalent because the material is abundant, stable, and non-toxic. On the other hand, gallium arsenide is especially useful for multi-junction cells, those consisting of multiple p–n junctions made of different semiconductor materials [7].

The use of different semiconducting materials in multi-junction solar cells allows the absorbance of a broader range of wavelengths, improving the cell's overall efficiency. According to figure 1.2, record efficiency levels of 44.4% and 46% have been reached by three and four junction cells, respectively, under concentrated sunlight illumination. Furthermore, nowadays multi-junction cells are commercially available with efficiencies between 38% and 43% [8]. Initially these cells were developed for special applications such as space exploration, due to its high manufacturing cost. However, they are now a days being increasingly used in an emerging new technology called concentrator photovoltaics (CPV), that uses lenses or curved mirrors to

focus sunlight onto small multi-junction solar cells. Figure 1.3 shows that CPV technology efficiency has increased due to research efforts done in recent years and that higher efficiency rates are foreseen for the next years.

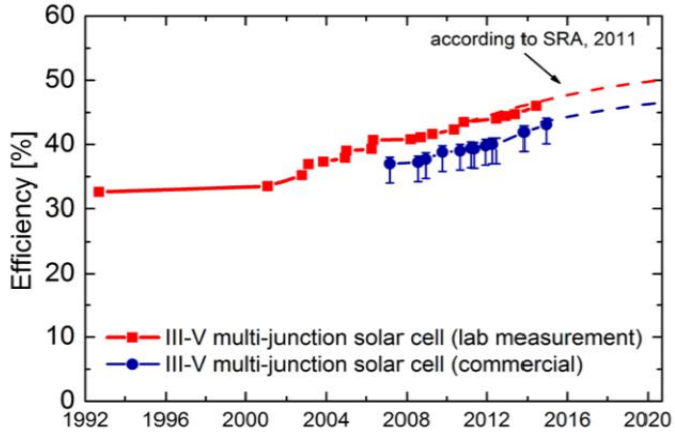

Figure 1. 2 - Development of record efficiencies of III-V multi-junction solar cells under concentrated light (Adapted from [8]).

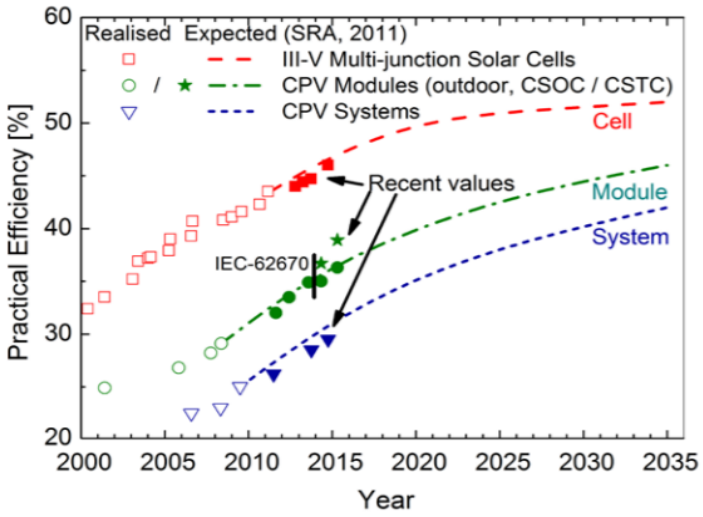

Figure 1. 3 - Development of record efficiencies of III-V multi-junction solar cells and CPV modules (Adapted from [8]).

Although silicon-based cells dominate the market, they are still relatively expensive to produce. The second generation of solar cells focuses on thin-film technologies in order to lower the high costs associated with the first generation by using inferior quality material and in lower amounts, deposited on cheap substrates [7].

Three of the most common PV technologies within the second generation are Amorphous Silicon (a-Si), Cadmium Telluride (CdTe) and Copper Indium Gallium Selenide (CIGS) thin-films. Amorphous silicon cells have a high absorption coefficient hence requiring less amount of material per cell, which can reduce production cost. However, the fact that the silicon material is not structured or crystalized on a molecular level, unlike other types of silicon-based solar

cells, can reduce the life cycle of the cell [7]. Still, this type of technology has low efficiency, with laboratory efficiencies of 10.2% [9]. The CdTe solar cells can reach a laboratory efficiency of 21% [9], but the presence of cadmium, which is a toxic substance raises health and environment concern, which contributes for the decrease in CdTe cells seen in the last few years illustrated in figure 1.4. On the other hand, CIGS technology is extremely promising and its excepted to grow over the next years, as seen in figure 1.4. Laboratory efficiency on these cells has reached 23.35% [9], making them the highest efficiency cells out of all thin-film cells, at a potentially low manufacturing price.

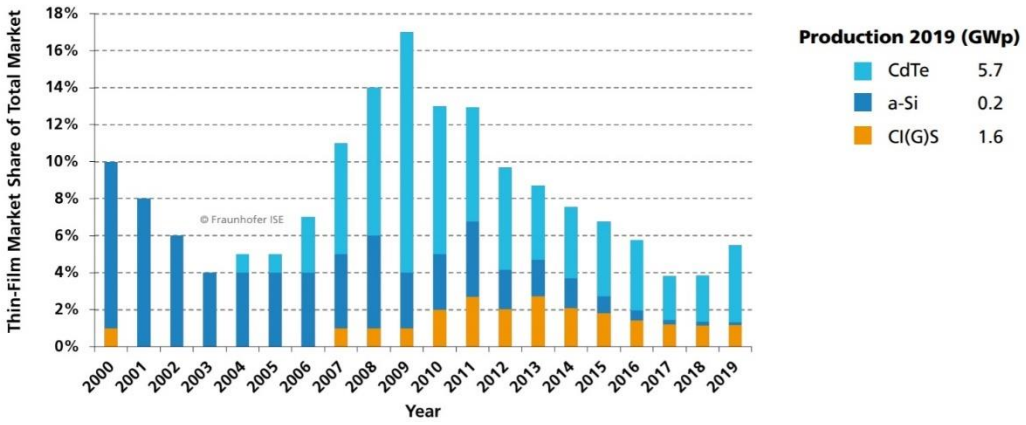

Figure 1. 4 - Global thin-film solar cells market share (Adapted from [74]).

More recently, third-generation solar cells aim to achieve high-efficiency devices while using thin-film, second-generation deposition methods and/or new techniques and materials. Like silicon based cells, third-generation cells use non-toxic and very abundant materials, hence are suitable for the large-scale implementation of photovoltaic cells [10]. Common third-generation technologies include dye-sensitized (DSSCs), organic (OPV), perovskite and quantum dot cells.

Organic photovoltaics (OPVs) display important advantages compared to previous generations including flexibility, lightweight, lower processing costs, and less environmental impact [11]. These cells have already exceeded certified efficiencies of 13%, reaching efficiency values obtained by low-cost commercial silicon solar cells. Nevertheless, the range of proposed maximum efficiency for OPVs varies from 15% to beyond 20%. While a large majority of OPV literature remains focused on efficiency values, the main issues restricting OPV commercialisation are scalability and long-term stability [12].

Quantum dot cells can involve different technologies based on semiconductor nanocrystals. This type of solar cells shares some of the same advantages as OPVs but often use rare or toxic materials. Despite some difficulties in application, efficiency rates have been risen, reaching values similar to those of OPVs, as shown in figure 1.5 [13].

Dye-sensitized solar cells are the most mature out all third-generation technologies and present the lowest cost. Based on organic dye-absorbers in a liquid electrolyte, many of their features and advantages overlap with those of OPVs [13]. However, as illustrated in figure 1.5,

record efficiency has not been exceeded since 2012, which shows low potential for further improvements.

As for perovskite solar cells, these are currently viewed as one of the most promising candidates to replace, or via a tandem device enhance, the dominant silicon photovoltaics technology [14]. They are characterized by their simple structure and high potential for cheap manufacturing. By looking at figure 1.5, it is possible to confirm that these cells have been associated with a rapid increase of efficiency values, which constitutes a substantial advantage over other third-generation technologies. Furthermore, perovskite silicon tandem solar cells have the potential to surpass the Shockley-Queisser limit[2] for single-junction solar cells, allowing for conversion efficiencies exceeding 30% [15]. According to figure 1.5 a record efficiency of 29.1% has already been reached this year, surpassing efficiencies of crystalline silicon cells.

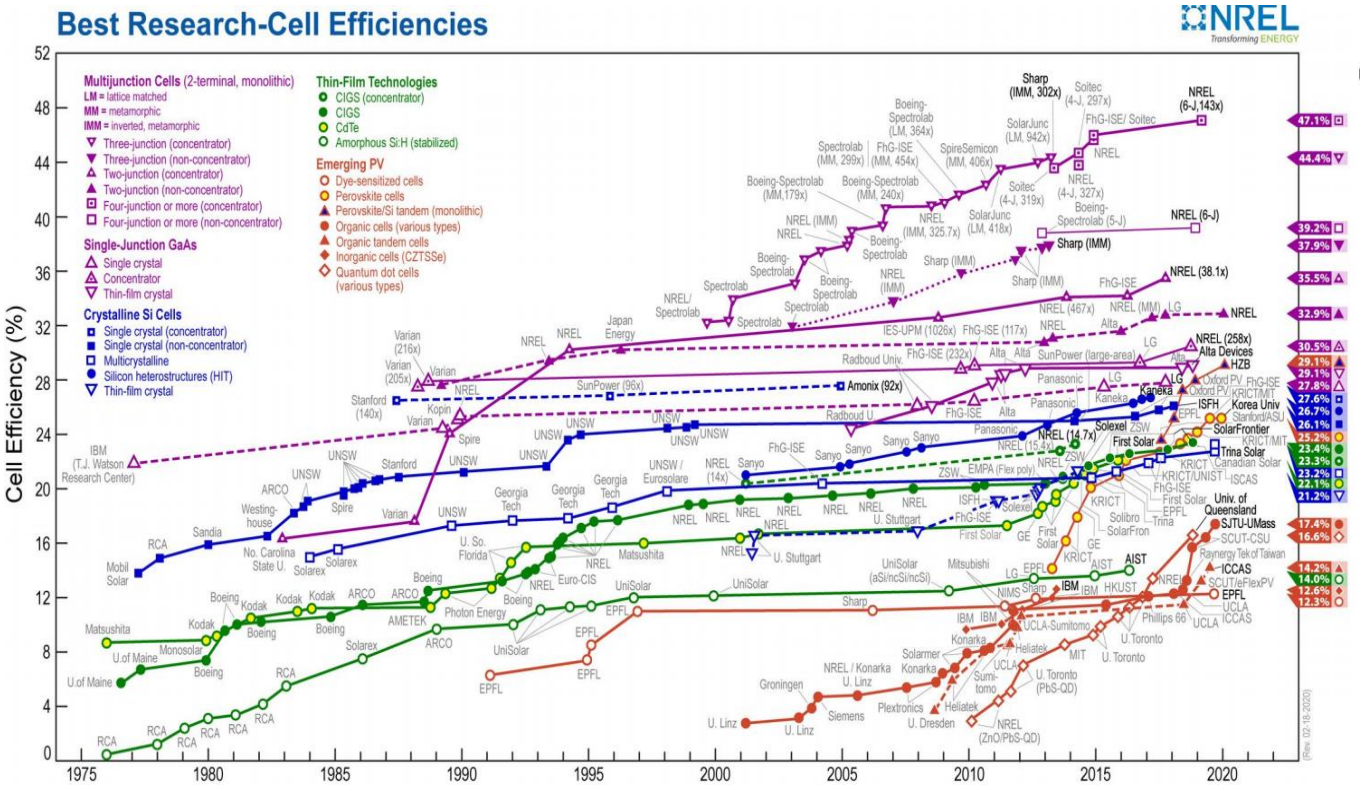

Figure 1. 5 - Best Research-Cell Efficiency Chart (Adapted from [66]).

[2] Shockley–Queisser limit refers to the maximum theoretical efficiency limit of a solar cell using a single p-n junction to collect power from the cell, where the only loss mechanism is radiative recombination in the solar cell. The maximum solar conversion efficiency is around 33.7% for a single p-n junction photovoltaic cell, assuming typical sunlight conditions [76].

1.2.1. End-of-life Management of Photovoltaic Modules

The energy industry is undergoing radical change and gradually moving towards renewable energy sourcing. Solar energy is becoming more efficient and less expensive, which is leading to an increasing number of solar panels being installed all over the world. However, this success is associated with a major challenge: solar panels will reach the end of their useful life and must be disposed of.

The life expectancy of a solar panel is around 20 to 30 years, considering a regular-loss scenario with no early problems. However, if we consider an early-loss scenario, with “infant”, “mid-life” or “wear-out” failures, the number of years drops substantially [16].

Global PV panel waste could reach 60 million tonnes by 2050, considering a regular-loss scenario and 78 million tonnes if one considers an early-loss scenario [17]. Also, improper disposal of solar modules can generate significant environmental impacts. These devices contain cadmium and lead, which can leak into the soil and consequently pollute the environment. Photovoltaic modules are typically composed by of glass, aluminium, rare earths, brominated flame retardants (BFRs) and other hazardous substances [18]. Thus, is extremely important to implement PV waste regulations that cover the collection, recovery, and recycling of the PV panels. At present, only the European Union has adopted such regulations. The EU Waste Electrical and Electronic Equipment (WEEE) Directive requires all producers supplying PV panels to the EU market (wherever they may be based) to finance the costs of collecting and recycling end-of-life PV panels put on the market in Europe [17].

Most efforts associated with solar panel recycling regard silicon based panels, since these hold the biggest market share, and aim to recover and recycle the most important parts [19].

Currently there are different recycling process applied to solar PV panels: physical, thermal, and chemical as it can be seen in figure 1.6 [19].

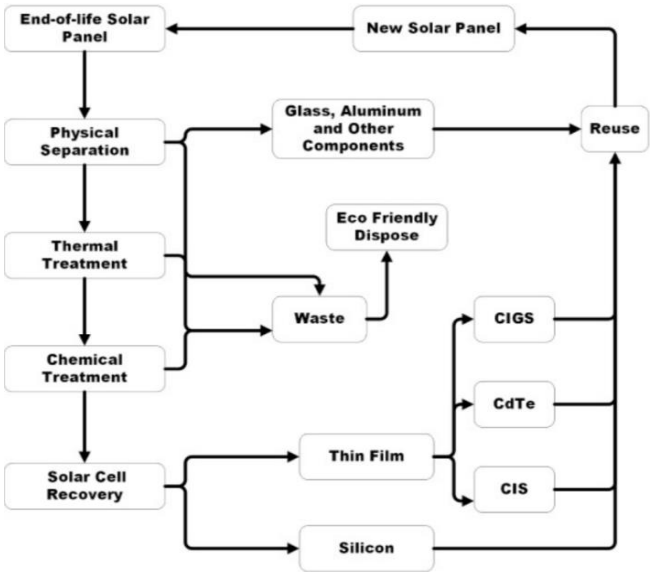

Figure 1. 6 - Different types of solar PV recycling processes (Adapted from [19]).

The goal is always to recover all sort of materials that can be reused in new solar panels and dispose of any waste in an eco-friendly manner.

During the physical separation process panels are dismantled by removing the surrounded aluminium frame, as well as junction boxes and embedded cables. The panel, junction-box and cables are then shredded and crushed to inspect the individual toxicity of each part and total toxicity of the module for disposal. The chemical and thermal treatment involves organic or inorganic solvents resulting in the separation of the cell from the glass, through the dissolution or disintegration of the ethylene-vinyl acetate (EVA) layer, recovering some valuable materials [19] [20] [21].

Besides the environmental benefits, the recycling of solar panels can become an important component of the PV value chain. Not only the recovered materials can be used to produce new PV panels, but they can also be sold into global markets, thus increasing raw material supply and consequently the manufacturing capacity. Raw materials technically recoverable from PV panels could cumulatively reach a value of up to 450 million USD (in 2016 terms) by 2030, which is equivalent to the amount of raw materials currently needed to produce approximately 60 million new panels, or 18 GW of power-generation capacity [17].

1.3. Objectives

The main objective of this dissertation is to study and assess the use of nanotechnology, more specifically, of nanoantennas, in photovoltaics.

Different 2D and 3D structures of a metallic nanoantenna array with subwavelength holes coupled to a photovoltaic cell are going to be designed and simulated. All the simulations will be carried out using the software *COMSOL Multiphysics*®. The simulated nanostructures present slight variations between each other, such as the position of the nanoantenna within the structure, the geometry of the holes of the nanoantenna and type of solar cell. The optical response of such structures is going to be computed, discussed, and compared.

Based on that analysis, the final goal is to understand whether the integration of nanoantennas in solar cells can actually bring advantages or additional improvements with regard to the process of solar energy harvesting and, of all models simulated, which one is best suited for this propose.

1.4. Outline

This dissertation will be divided into six chapters as it follows:

Chapter 1 – Introduction: In this chapter the motivation for this work is presented as well as an overview of the different photovoltaic technologies available nowadays and the undergoing research efforts and developments in that same field. The main objectives of this dissertation are also declared.

Chapter 2 – Nanoantennas for Solar Energy Harvesting: This chapter offers insight on the subject of using nanoantennas for solar energy harvesting purposes by reviewing its history and evolution, along with the specifics behind the operation of solar energy harvesting systems

containing nanoantennas. Different materials and design specifications regarding nanoantennas are also reviewed.

Chapter 3 – Theoretical Foundations: This chapter includes a theoretical review regarding the matter of this dissertation. Different classical diffraction theories are examined, the topic of light-matter interaction is explored and the photovoltaic effect, along with different types of solar cells, are described.

Chapter 4 – Model Structure and Configuration This chapter provides an overview on the software *COMSOL Multiphysics*®, which is used to perform all simulations. The different 2D and 3D structures that are simulated are described in detail, as well as the conditions and requirements regarding each model.

Chapter 5 –Simulation Results: In this chapter the results obtained from all the performed simulations are presented and analysed.

Chapter 6 –Conclusions: In this chapter, all the previously developed work is reviewed, and final conclusions are presented. In addition, possible future work topics are pointed out.

2. Nanoantennas for Solar Energy Harvesting

2.1. General Overview

Electromagnetic radiation provided by the Sun results in a constant energy source for the Earth. This radiation occurs over a wide range of wavelengths, however most of the radiation includes ultraviolet, visible, and infrared radiation [22].

Currently, photovoltaic panels are the most used technology for converting solar energy into electricity. Although PV technology has improved a lot in recent years, it is still not able to fully utilize the abundance of solar energy reaching the earth in the visible and infrared regions and the reradiated infrared energy [23]. Moreover, as a quantum device, the efficiency of PV is a function of the bandgap and the match of the bandgap to the solar spectrum and, therefore, is also restricted by it. This sets an upper limit of efficiency for single-junction solar cells of approximately 30% and, even for more complex multijunction solar cells efficiency values will not exceed 55% [24]. Furthermore, PV materials are typically only operational during daylight hours and require direct solar radiation for optimal efficiency.

Optical antennas are devices that convert propagating optical radiation into localized energy, and vice versa. They can control and manipulate optical radiation at subwavelength scales [25]. These devices show a wider angular reception characteristic than that of PV devices which optimizes the solar energy collection and eliminates the necessity of sun-tracking devices [26]. Thus, if coupled with PV solar panels, the overall efficiency of the system is expected to be higher than the current efficiency rate of solar panels.

Optical antennas are similar to microwave and radiofrequency (RF) antennas and can couple electromagnetic radiation in the visible and infrared just like other antennas do at their corresponding wavelengths [23]. Although similar, there are crucial differences between optical antennas and their microwave and RF counterparts due to their nano size and the resonant properties of metal nanostructures [27].

The concept of using optical antennas in solar energy harvesting has been intensely investigated and it seems to be a viable way of overcoming some of the main disadvantages of solar cells. The main idea behind this approach is to scale and operate antennas at extremely high frequencies, meaning very short wavelengths in the infrared or visible regime [26].

Moreover, as the fields of nanoscience and nanotechnology evolve and the available tools improve, devices such as optical antennas or nanoantennas could have several other unique applications. These antennas can be particularly efficient at selected frequencies which is a promising attribute for biological and chemical sensing and detection (near-field microscopy and high-resolution biomedical sensors) [25]. The technology may also support emerging applications such as building insulation, window coatings and heat dissipation in small electronic products [3].

2.2. Brief History

The initial rectenna concept was proposed for microwave power transmission by the Raytheon Company in 1964. Since then a lot of research has been done in order to utilize rectennas in solar power conversion by extending the concept of rectennas to other wavelength regions such as infrared and visible [3].

The idea of using nanoscale antennas to convert optical waves into electricity was introduced in 1972 by Robert L. Bailey. Alongside James C. Fletcher, Bailey patented an “electromagnetic wave energy converter", a device similar to modern day optical rectennas. The structure consisted of pairs of pyramids serving as modified dipole antennas, each pair connected to a diode, a low pass filter and a load [28] [29].

Since then research in the field of nanoantennas has increased and multiple patents have been issued related to electromagnetic energy converter devices. In 1984 Alvin M. Marks received a patent for the first device using sub-micron antennas for the direct conversion of solar energy into electrical power. The device performed significantly better than the one previously proposed by Bailey and Fletcher [28]. Marks went on to issue a number of other patents for devices that collected and converted electromagnetic energy, eventually reaching theorical efficiency rates of 80% [29].

In 1996, Guang H. Lin reported light absorption by a resonant nanostructure and rectification at frequencies in the visible range. The device was composed by a parallel dipole antenna array on a silicon substrate and used a p-n junction for rectification. In addition, the device showed antenna-like characteristics since the obtained output was resonant with the dipole length as well as dependent on light polarization and the angle of incoming light [29]. Lin invention demonstrated that rectification of light in the visible range is possible which was a substantial progress in the process of conversion of solar energy into electricity.

In 2001, the National Renewable Energy Laboratory (USA) in collaboration with the ITN Energy Systems Inc. conducted a study with the purpose of demonstrating the feasibility of high efficiency nanoantennas at a single wavelength [29]. ITN’s optical rectenna consisted of an optical antenna to efficiently absorb the incident solar radiation and a high frequency metal-insulator-metal (MIM) tunnelling diode that rectifies the AC field across the antenna, providing DC power to an external load. The device efficiency is not fundamentally limited, unlike what happens for conventional PV, with conversion efficiency rates of 85% or more being theoretically possible [24]. The device was able to reach over 50% conversion efficiency operating in the microwave range at 10 GHz frequency. Later on, ITN’s collaboration with the US National Institute of Standards and Technology (NIST) resulted in an infrared rectenna with MIM diodes between dipoles for operation at 30THz by atomic layer disposition [29].

Most of these devices presents efficiency rates for a single frequency and not an overall efficiency regarding a certain frequency range. To evaluate the performance of the whole rectenna system, the concept of an overall efficiency would be necessary since solar radiation is spread over several different frequencies, mainly in the visible and near-IR bands [30]. Thus, in 2008, Dale K. Kotter [3] defined a notion of total harvesting efficiency rates that reached levels of

60%-70% using a dipole nanoantenna, which validates the possibility of using nanoantennas for solar energy conversion into electricity with high efficiency rates [30].

Since then, lots of efforts have been undertaken to improve nanoantennas efficiency rates mainly by investigating alternative materials and different designs.

2.3. Theory of Operation

Electromagnetic waves induce time-varying electric fields in metals that exert a force on the gas of electrons inside the material, causing the charge carriers to oscillate in a collective movement. This phenomenon is known as surface plasmon and it will be discussed in detail in subchapter 3.3.2. If the resonant frequency of the designed nanoantenna matches the incoming wavelength frequency it leads to the absorption of the incoming EM radiation [28]. At these frequencies, when the antenna enters a resonance mode, the electrons flow freely along the antenna generating alternating current (AC) at the same frequency as the resonance [23]. However, for the nanoantenna to convert the collected current into DC current it needs to be complemented with a rectifying element. After the conversion, the resulting DC current can be used to power an external load. The combination of receiving antenna plus rectifying element is commonly referred to as a rectenna [28] [31].

A rectenna is essentially a circuit containing an antenna and a diode, which converts electromagnetic waves into direct current (DC). While most rectennas work with radio waves or microwaves, an optical rectenna operates in a similar way but for infrared or visible light. This presents a big challenge since working with extremely high frequencies (THz) requires using diodes with switching rates capable of performing high frequency rectification without significant loss.

Figure 2.1 demonstrates the process of solar energy harvesting using an optical rectenna system. The incoming optical radiation induces currents flowing in the nanoantenna generating AC power which is then fed through a matched rectifier to produce DC power [30].

The efficiency rate of absorption of the incident radiation depends on the design of antenna resonance and impedance matching of the antenna. Nevertheless, modelling and experimental measures performed in [23] show that nanoantennas can eventually absorb close to 90% of the available in-band energy.

The major challenges associated to nanoantennas are related with the development of economical large-scale manufacturing methods. Moreover, further research is still required to improve the efficiency of rectification of antenna induced terahertz currents to a usable DC signal [3].

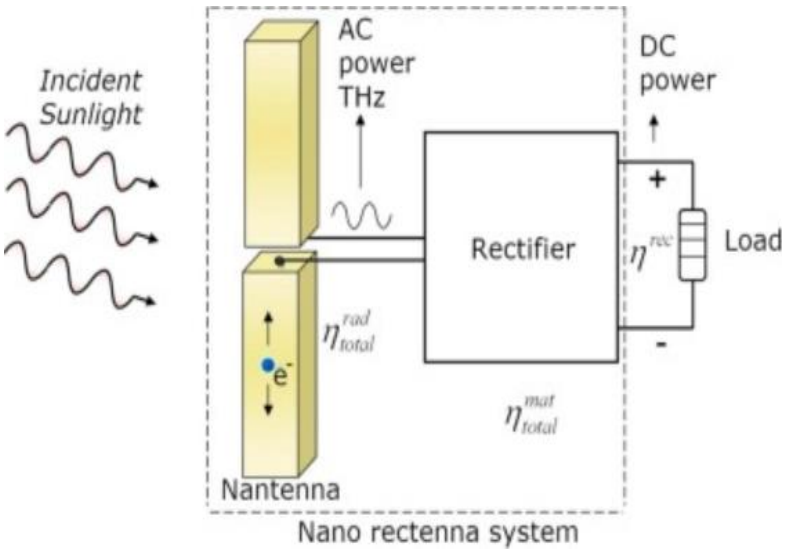

Figure 2. 1 - Schematic representation of a solar energy harvesting system (Adapted from [30]).

Nanoantennas can utilize both the visible and IR regions of the light spectrum as well as the reradiated IR energy, capturing the energy of the Sun during the day but also the radiation of the Earth at night. This fact alongside the high theoretical efficiency rates makes this technology a very promising alternative to more conventional solar energy conversion methods.

2.4. Technical Framework

In the last decade, the concept of antenna has evolved to include nanoantennas. The development of this technology is connected to the emergence of nano-optics, a science field that studies the transmission and reception of optical signals at the nanoscale [32]. During recent years, a lot of research has been developed regarding different nanoantennas designs and materials for various applications. However, these devices still face some challenges and there is a need for improvements.

In order to create an efficient rectenna system (antenna plus rectifier), the choice of materials and geometry of both the nanoantenna and the rectifying diode are crucial.

According to classical circuit theory, the impedance of the diode must match the impedance of the antenna for efficient power transfer. Since the antenna impedance usually varies from tens to hundreds of ohms at THz frequencies, and can reach a thousand ohms at visible light frequencies, the diode resistance needs to be within the same range [33]. The diode capacitance is also a key factor, as the circuit RC time constant must be smaller than the time constant corresponding to frequencies in the visible range [33]. Also, it is important that the diode presents an extremely small, if none, reverse bias leakage current (current at negative bias voltages) in order to achieve an adequate amount of energy harvested by the rectenna [33]. Finally, diodes must have a small size to be incorporated in the rectenna system, as well as small turn-on voltage,

and efficient operation at THz and IR frequencies in order to rectify the received signals. These are some of the existing difficulties regarding the rectifying diodes incorporated into the rectenna system [31].

As for the nanoantenna, although there are fewer obstacles in its production when compared to the rectifying diodes, the challenges still exist. All the elements of the antenna must be extremely small, and the device must be capable of efficiently capture all polarizations of the incident radiation [31] [33]. To do this successfully without the need for a sun-tracking system, means that the acceptance angle must always be as wide as possible. It is also important to consider the impedance and capacitance of the antenna. However, the impedance of an antenna should always be around 100 ohm and the contribution of the capacitance of the antenna to the rectenna system is a lot less significant compared to the diode capacitance [33]. Also, it is important to emphasize that the output supplied by a single nanoantenna is not sufficient to drive the rectifier and to provide DC power to an external load. Thus, nanoantennas are usually gathered in arrays to increase their output signal. The total field captured by the array corresponds to the vector addition of the fields captured by each individual nanoantenna [28].

2.4.1. Rectifier System

Conferring to what has been already discussed in subchapter 2.3, the nanoantenna device is not capable to convert the generated AC current into DC current, thus requiring a rectifying element.

Schottky diodes operation is based on the physical mechanism of the Schottky barrier which is a potential energy barrier formed when a metal and semiconductor are brought into contact as a junction. These diodes have a fast response time but are typically used for rectification and detection at the lower frequency range [4] [34]. As an alternative to the Schottky diode, the **metal-insulator-metal (MIM) diode** is the most popular rectifier to use for frequencies ranging from far-IR to visible range [4].

The **MIM** diode is a thin film device consisting of an insulator layer located between two metal electrodes. The rectification process is based on the electron tunnelling process through the insulator layer, on a femtosecond timescale [4] [31].

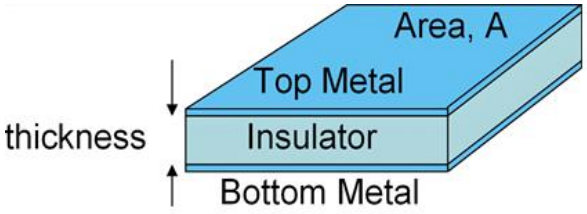

Figure 2. 2 - MIM diode (Adapted from [67]).

In order to ensure a successful rectification, the insulator layer must be extremely thin to allow sufficiently large electrical current, ensuring the occurrence of the tunnelling effect. The behaviour of the I–V characteristics of the MIM diode should be nonlinear and asymmetrical, with no external bias applied. These conditions can be fulfilled by using different metals on both sides of the insulator layer. Additionally, the diode area must be very small in order to increase the cut-off frequency, allowing rectification at THz frequencies [31] [4]. Finally, it is crucial that the antenna resistance be similar to the diode's resistance to provide good impedance matching between them, which will increase the system efficiency [4].

The high-speed characteristics and compatibility with integrated circuits of the MIM diode makes it the most appropriate choice to work with IR and visible regime. Moreover, due to the small active area required for this type of diode it is possible to obtain a large volume of devices in the same unit area [34].

Metal multi-insulator metal (MIIM) diodes are an alternative to MIM diodes with the ability to enhance the I-V nonlinearity of the MIM diodes. Larger nonlinearity in the I-V can, for a given capacitance, lower the diode secant resistance[3] so that the diode impedance is better matched to the antenna impedance. Furthermore, the addition of the second insulator improves the diode responsivity resulting in more current for a given optical power input. Also, the reverse bias leakage current of a MIIM diode is greatly reduced [33].

Even though the MIIM diode has some advantages and even a higher efficiency when compared to the MIM diode, it requires a higher bias to move the electrons out of the quantum well created by the two insulating layers [23]. This may explain the fact that MIM diodes still remain the most used type of diode in energy conversion resorting to nanoantennas.

2.4.2. Nanoantenna Designs

Nowadays most nanoantennas structures are made of plasmonic materials. These materials, usually metals, possess unique optical properties. These metals are typically gold, silver, platinum, or aluminium since, at optical frequencies, these are capable of supporting surface plasmon resonance[4]. **Plasmonic nanoantennas** can present different geometries, the most common ones are represented in figure 2.3.

[3] The secant resistance determines the coupling efficiency between the antenna and diode at optical frequencies. The diode AC resistance required for impedance matching with the antenna is given by the secant resistance [33].
[4] The phenomenon of surface plasmon is discussed in detail in chapter 3.

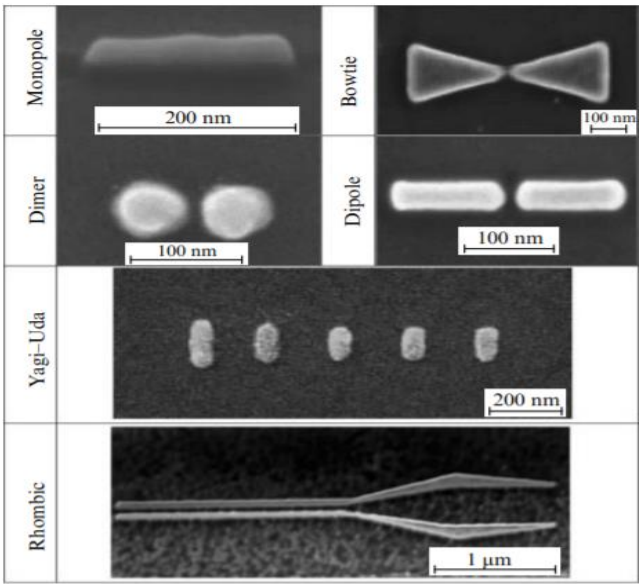

Figure 2. 3 - Main types of plasmonic nanoantennas (Adapted from [35]).

Different geometries carry different attributes and, therefore, can serve different purposes.

The authors of [35] classify and characterize in depth the different designs of plasmonic nanoantennas, illustrated in figure 2.3. For each category, literature is reviewed, and strengths and vulnerabilities of the type in question are discussed.

Most plasmonic nanoantennas constitute narrowband devices, therefore are usually tuned to operate at frequencies close to plasmon resonances. The directivity of a nanoantenna decreases when moving away from these resonances and, since most practical applications require broadband nanoantennas, it's important to further extent the bandwidth of plasmonic nanoantennas [35]. More complex structures have been designed to try to tackle this issue. The square-spiral nanoantenna is one of the most promising ones and figure 2.4 shows the geometry of this device.

Spiral nanoantennas allow the electric field to be concentrated in the feed point (gap between the two metallic arms), an ideal location to transport energy needed to supply other circuits [22]. Their broad bandwidth combined with the ability to concentrate light efficiently, make them particularly appealing for solar energy harvesting. Also, these antennas are good resonators, being expected to capture a large electric field at resonance. Moreover, the gain performance of the nanoantenna can be improved by increasing the number of arms [31].

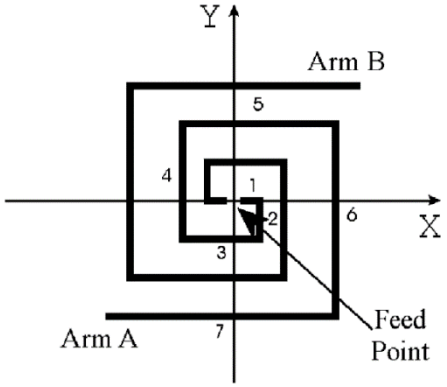

Figure 2. 4 - Two-wire square-spiral nanoantenna (Adapted from [72]).

Besides plasmonic nanoantennas, there has also been research concerning nanoantennas made with dielectric materials. **Dielectric nanoantennas** benefit from the optical response of dielectric and semiconducting particles. Usually constituted by optically transparent materials, their resonant response depends on the formation of an effective resonator inside the particle [35]. Dielectric and semiconducting materials are characterized by low dissipative losses in the optical range, unlike metallic materials that are associated with high energy dissipation [35] [36]. Metallic nanoantennas can exhibit significant gains in directivity but the losses inherent to the use of metals in the optics can sometimes be an impediment that, with the use of lossless dielectric, ceases to exist [36]. Additionally, dielectric materials such as silicon have high values for the real part of permittivity in the optical range, which means that for those wavelengths nanoparticles can exhibit electric and magnetic resonant responses, thus improving overall radiation efficiency and antenna directivity. Other than silicon (Si), materials like germanium (Ge), aluminium antimonide (AlSb) and aluminium arsenide (AlAs) are also suitable for this type of nanoantennas since they display those same properties [35].

In the simulations computed throughout this dissertation, a different type of nanoantenna is used: the **aperture nanoantenna**. Aperture nanoantennas are able to increase coupling efficiency of nearby light by focusing it onto an aperture region which enables light confinement and better control of the radiation pattern [37].

It is possible to divide aperture nanoantennas into three main types: single subwavelength aperture, single aperture surrounded by shallow surface corrugations, and subwavelength aperture arrays [38]. Examples of these nanoantennas are illustrated in figure 2.5.

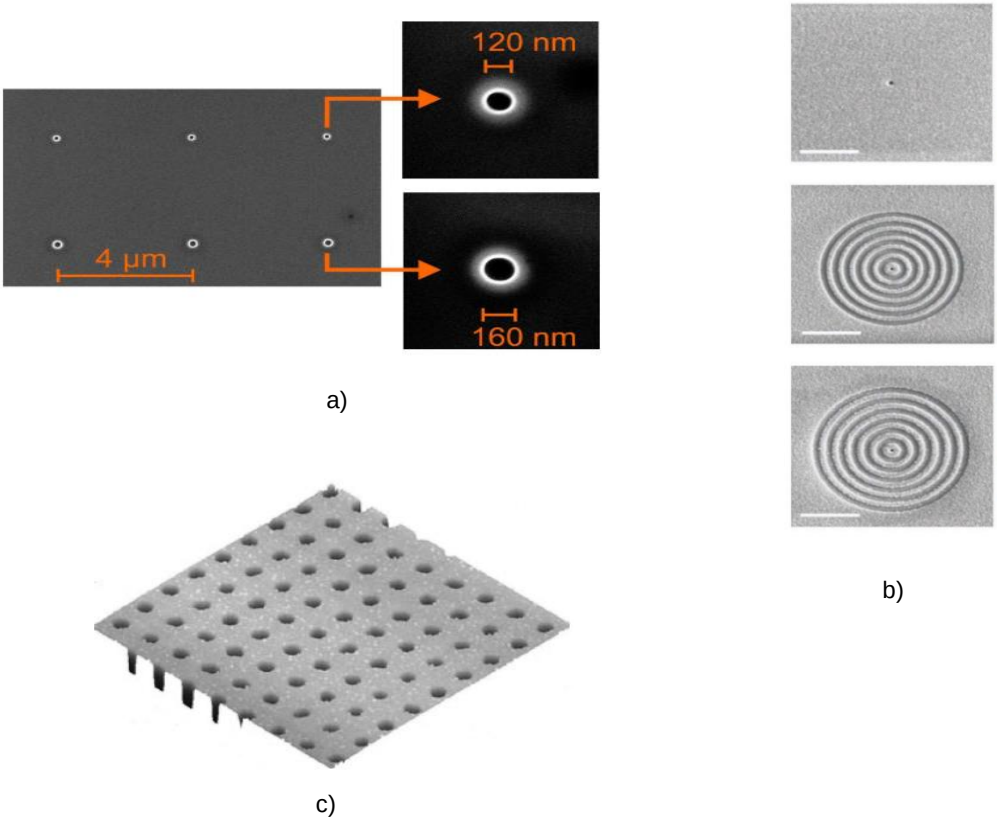

Figure 2. 5 - Main types of aperture nanoantennas (Adapted from [38]).

a) Electron microscope images of 120 and 160 nm single apertures milled in gold.

b) Scanning electron microscope images of corrugated apertures (scale bar 2 µm).

From top to bottom: single 120 nm aperture, antenna with concentric grooves of 350 nm period and antenna with a larger groove period of 420 nm.

c) AFM images of 200 nm diameter aperture array with 1 µm period.

Since the practical use of subwavelength apertures to enhance light-matter interaction first took place, the interest in the Extraordinary Optical Transmission (EOT)[5] phenomenon keeps increasing and has already led to much research on the origin of the phenomenon, the influence of several design parameters (aperture shape and dimensions, metal permittivity, metal adhesion layer) and the development of practical applications [38].

Single apertures are perforated on metal films which are typically made from aluminium, gold, or silver, depending on the wavelength at which the antenna will operate. The first studies on this matter were performed using circular holes as apertures, though in more recent years several different aperture shapes have been considered such as slits, rectangles and triangles [38]. Figure 2.6 shows the transmission spectra for single circular holes perforated on a suspended

[5] The Extraordinary Optical Transmission phenomenon is reviewed in detail in subchapter 3.3.3

silver film, demonstrating the presence of a transmission resonance with an intensity that decreases with the increasing h (thickness of the metal film). The resonance derives from the excitation of a localized surface plasmon at the edges of the hole [39].

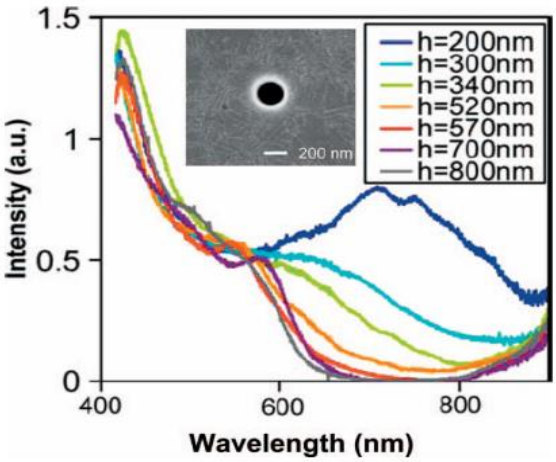

Figure 2. 6 - Transmission spectra for single circular holes for a range of film thicknesses h (Adapted from [39]).

Circular hole of radius r=135 nm perforated on a suspended silver film.

Each curve is an average of spectra obtained for several isolated holes of the same size.

Adding concentric surface corrugations (or grooves) on the metal around the central aperture helps to increase the effective aperture area while keeping the subwavelength dimensions of the aperture. The **corrugated apertures nanoantenna** design takes advantage of both the extended near to far-field conversion capabilities of the grooves and the light confinement of the nanoaperture. By providing local intensity enhancement and emission directionality, this type of antenna constitutes an excellent option to control radiation from single quantum emitters [38].

Arranging the apertures in a subwavelength array with a periodic pattern is another alternative design for aperture nanoantennas, the **subwavelength aperture array**. Although this design provides extra coupling capabilities, there are dependencies regarding hole size, lattice spacing, metal film thickness, and angular dispersion. Several other parameters also have significant importance such as type of metal, symmetry in the dielectric-metal-dielectric layer stack, finite-size effects of the lattice, and the hole shape [39]. The transmission peaks observed in the far-field and the intensity enhancement in the near-filed, characteristic of the aperture array, are consequence of two different resonant phenomena: the resonant excitation of surface plasmon waves at the metal-dielectric interface and the localized plasmon modes on properly shaped apertures [38].

2.4.3. Efficiency

The efficiency of a rectenna system is a combination of the efficiencies of the two main components of the system: the antenna and the rectifying element. The thermodynamic cap on the efficiency of a rectenna solar cell is given by the Landsberg[6] efficiency limit of 93%. Several factors can limit the achievable efficiency, including the antenna radiation efficiency, resistive losses in the antenna, antenna-to-diode power transfer, and diode efficiency in converting AC to DC current [40].

Although most efficiency rates are a function of a single frequency and not an overall efficiency regarding a certain frequency range, a notion of total harvesting efficiency of a nanoantenna has been developed and according to the authors of [23] is given by (2.1), where λ is the wavelength of the incident light and the upper and lower integration limits, λ_{start} and λ_{stop}, correspond to the optical range for the solar energy harvesting [30].

$$\eta_{tot}^{rad} = \frac{\int_{\lambda_{start}}^{\lambda_{stop}} P_{inc}(\lambda) * \eta^{rad}(\lambda) d\lambda}{\int_{\lambda_{start}}^{\lambda_{stop}} P_{inc}(\lambda) d\lambda} \tag{2.1}$$

The antenna radiation efficiency as a function of the wavelength, $\eta^{rad}(\lambda)$, is given by (2.2) where P^{rad} is the radiated power, P^{inj} is the injected power available at the antenna input port and P^{loss} is the power dissipated by the material of the antenna [30].

$$\eta^{rad} = \frac{P^{rad}}{P^{inj}} = \frac{P^{rad}}{P^{rad} + P^{loss}} \tag{2.2}$$

The incident power, $P_{inc}(\lambda)$ given by (2.3), follows Planck's law for black body radiation,

$$P_{inc}(\lambda) = \frac{2\pi hc^2}{\lambda^5} * \frac{1}{e^{hc/\lambda KT} - 1} \tag{2.3}$$

where T is the absolute temperature of the surface of the Sun in Kelvin (K), h is the Planck's constant (6.626x10^{-34} J.s), c is the speed of light in vacuum (3x10^{8} m/s) and K is the Boltzmann constant (1.38x10^{-23} J/K) [30].

Based on the total radiation efficiency defined in (2.1), it is possible to define the total matching efficiency regarding the rectifying element connected to the nanoantenna as

[6] When the solar cell is considered to be a black body converter absorbing radiation from the Sun, a black body itself, without creating entropy, an efficiency limit of about 93% is obtained, known as the Landsberg efficiency limit.

$$\eta_{tot}^{mat} = \frac{\int_{\lambda start}^{\lambda stop} P_{inc}(\lambda) * \eta^{rad}(\lambda) * \eta^{mat}(\lambda) d\lambda}{\int_{\lambda start}^{\lambda stop} P_{inc}(\lambda) * \eta^{rad}(\lambda) d\lambda} \quad (2.4)$$

where $\eta^{mat}(\lambda)$ is the matching efficiency of the rectenna system, defined by (2.5), where Z_{rec} is the impedance of the rectifier, Z_{ant} is the input impedance of the nanoantenna, R_{rec} is the real part of the rectifier impedance, and R_{ant} is the real part of the nanoantenna input impedance [30].

$$\eta^{mat} = \frac{4 * R_{rec} * R_{ant}}{|Z_{rec} + Z_{ant}|^2} \quad (2.5)$$

Combining (2.1) and (2.4) the rectenna efficiency, η^{rec}, can be defined by [30]:

$$\eta^{rec} = \eta_{tot}^{rad} * \eta_{tot}^{mat} \quad (2.6)$$

Theoretically, the energy conversion efficiency for a rectenna with an ideal rectifying element is only limited by the Landsberg limit. However, if a rectenna can eventually be compared with a solar thermal collector, the solar energy conversion efficiency limit drops to 85,4%, which is the limit for a non-energy-selective collector with ideal concentrating properties. However, this limit may increase, as in the case of multicolour thermal converters that use multiple materials with different bandgaps, increasing the efficiency limit to 86,8%. An infinite number of frequency-selective filters in a rectenna would offer a similar advantage [29].

A more conservative analysis can still be made regarding the energy conversion efficiency limit for a rectenna. Conventional semiconductor solar cells efficiency has a limit of 44% corresponding to the old Trivich-Flinn efficiency limit, that was later incorporated into the Shockley-Queisser limit. These cells operate at a single bandgap energy and therefore cannot absorb photons with energy lower than the bandgap and use only a bandgap energy's worth of high energy photons. Since a rectenna can only function at a single operating voltage, only photons at the operating voltage can be used in an effective manner. Just like for conventional solar cells, lower energy photons are wasted, and the potential of higher energy photons is only partially utilized. Thus, the operating voltage limits the efficiency of the rectenna similarly to the way bandgap limits the efficiency in conventional solar cells. Hence, one can argue that the broadband rectenna efficiency limit is also 44% [33].

Till this date, the experimentally obtained results regarding power conversion efficiencies of rectennas systems are still low. This can be attributed to the main obstacles in the performance of rectennas at the infrared and visible regions: the fact that metals are no longer perfect conductors at these wavelengths, the efficiency rate of power conversion from AC to DC and the impedance mismatch between the nanoantenna and the diode used for rectification.

2.5. Applications

Nanoantennas can possibly be advantageous in improving the solar energy conversion efficiency when coupled with solar cells. Nonetheless, large-scale commercialization of these devices could offer a diversity of other applications in the field of energy conversion.

Structures combining nanoantennas and rectifying elements could be integrated in consumer electronic devices and provide for the continual charging of their batteries. Additionally, buildings or roofs could be coated with these devices and the produced energy could feed the power grid [3].

Nanoantennas could also be implemented in double-sided panels. One side of the panel would absorb a broad spectrum of energy from the Sun during the day, while the other side could absorb radiation in the narrow frequency of energy from Earth's radiated heat. The double-sided panels could also be used to take in the residual heat from electronic devices [3] [23].

Infrared and multi-spectral imaging is also a field of application for optical antenna devices. As infrared imaging moves towards multi- and hyper-spectral imaging, the authors of [41] propose the use of optical antennas with fractal geometry for this emerging field.

Another point of interest for optical antennas is in the field of near-field optics (NFO). NFO is a branch of nanometre-scale science and technology regarding the optical properties of nano-sized structures as well as optical processes occurring on that scale. The excitation and properties of surface plasmon polaritons (SPPs) play a prominent role in this field, and the combination of antenna resonances and SPPs resonances holds promise for localized field enhancement. Structures like small apertures and scattering particles have already been used for optical imaging beyond the diffraction limit by means of scanning near-field optical microscopy (SNOM) [41].

Finally, the same advantages that nanoantennas provide for infrared imaging can also be applied in the development of optical antenna sensors. The ability that optical antennas have to detect polarization can be fully integrated in new designs of sensors for spectroscopic applications [41].

3. Theoretical Foundations

3.1. Concept of Light

In the XVII century, Isaac Newton developed his corpuscular theory stating that light is composed by particles of matter (corpuscles) emitted in all directions by a certain source. Christiaan Huygens, on the other hand, proposed a mathematical wave theory of light, defining light as a series of waves emitted in all directions. At the time, Newton's corpuscular theory was the dominant one regarding the model of light. In 1803, Thomas Young introduced the concept that light waves could interfere with each other and, with his double-slit experiment, showed that light has wave like characteristics. Later on, Augustin-Jean Fresnel reformulated Huygens' theory and the Huygens-Fresnel principle was developed. Fresnel was also able to calculate the distribution of electromagnetic waves in diffraction patterns. These accomplishments significantly contributed to the establishment of the wave theory and the classical particle theory was finally abandoned, only to partly re-emerge in the XX century [42].

In the XIX century, James Clerk Maxwell concluded that light is a form of electromagnetic radiation and published a mathematical description of the behaviour of electric and magnetic fields, known as the Maxwell's equations. Soon after, Maxwell's theory was confirmed experimentally by Heinrich Hertz who generated and detected radio waves in the laboratory, demonstrating that these waves behaved exactly like visible light, exhibiting properties such as reflection, refraction, diffraction, and interference.

In the XX century, with the development of quantum mechanics, the debate over the nature of light resurfaced. Max Planck introduced the idea of light-quanta[7] and later, De Broglie explored the reconciliation of the light-quanta, which Einstein then used to explain the photovoltaic effect. Einstein believed that light is a particle referred to as photon and the flow of photons is a wave [43] [42]. Eventually, the concept of wave–particle duality emerged, and light came to be defined as both a particle and a wave since, according to this concept, every particle or quantum entity may be described as either a particle or a wave.

3.2. Diffraction Theories

3.2.1. Huygens-Fresnel Principle and Young's Experiment

During the XVII century, Christiaan Huygens developed a principle based on the wave theory of light. The Huygens principle states that every point on a primary wave front can be considered as a continuous emitter of secondary wavelets and these secondary wavelets combine each other

[7] *Quanta*, plural of *quantum*, is a term used in physics to define the minimum amount of any physical entity involved in an interaction. For example, a photon is a single quantum of any form of electromagnetic radiation.

in order to produce a new spherical wave front in the direction of the propagation, as illustrated by figure 3.1 [44]. In the specific case of a plane wave with normal incidence to an array of slits, each slit will behave as a punctual source. Therefore, after the array there will be formed as many waves as the number of slits in the array [45].

However, the principle could not explain the deviations from rectilinear propagation that occur when light encounters edges or apertures, commonly known as diffraction effects. Augustin-Jean Fresnel later reformulated Huygens's principle for a curve wave front since, near slits or apertures, the wave is not plane [45]. Fresnel was able to show that the combination of both principles could explain both the rectilinear propagation of light and also the diffraction effects.

The Huygens Principle and Fresnel's modification are collectively known as the Huygens-Fresnel Principle and constitute the baseline of diffraction theories that can be applied to various problems regarding wave propagation, diffraction, and reflection.

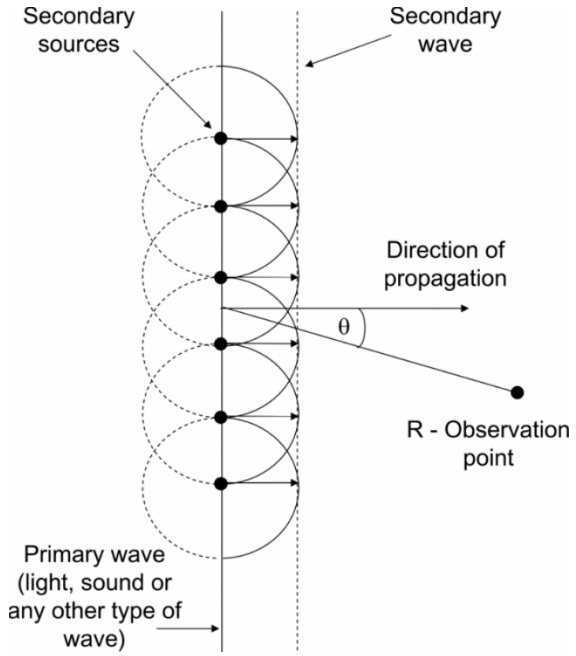

Figure 3. 1 - Huygens-Fresnel principle (Adapted from [44]).

Thomas Young was the first to demonstrate the phenomenon of light waves interference with the double-slit experiment, thus confirming the Huygens-Fresnel principle. As seen in figure 3.2, light is incident on a perfect conductive plane (metal sheet) with two slits, and a target (screen) is placed in parallel to the plane. Once the light passed through the slits, the waves spread out and interact with one another. Where the waves meet crest-to-crest, they interfere constructively and leave a brighter spot on the screen. Where the waves meet crest-to-trough, the interference is

destructive, cancelling each other out and leaving a dark spot on the screen. That process eventually produces what it is called an “interference pattern” as shown in figure 3.3 [46].

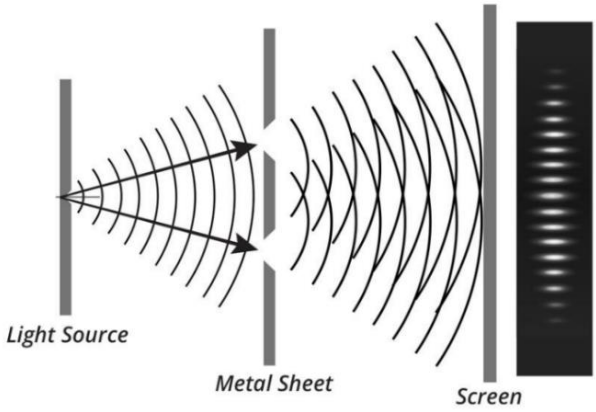

Figure 3. 2 - Young's experiment geometry (Adapted from [46]).

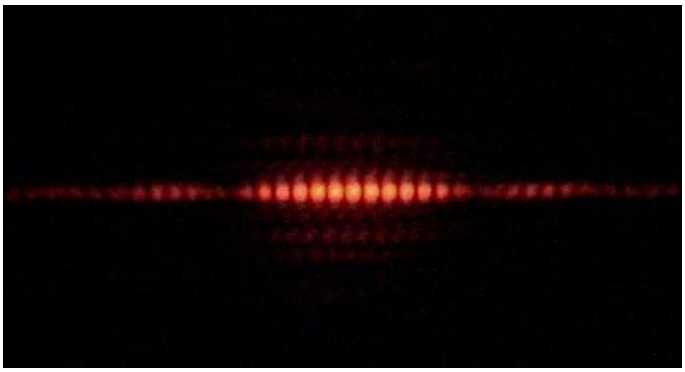

Figure 3. 3 - Double-slit pattern (Adapted from [46]).

3.2.2. Fraunhofer Diffraction Theory

When studying the diffraction of light through a slit, irradiance $I(\theta) \propto \langle E^2 \rangle$, is often an important parameter since it can be easily measured and used to compare theory and simulation results.

If a monochromatic plane wave passes through a slit with normal incidence, in a metal that is assumed to be a perfect conductor, according to Fraunhofer theory it is possible to characterize the irradiance on the y' axis, represented in figure 3.4. The irradiance will be defined by [47]:

$$I(\theta) = I(0)\left(\frac{sin(\beta)}{\beta}\right)^2 \tag{3.1}$$

Where $\beta = (kb/2)sin\theta$, b is the size of the slit, $k = 2\pi/\lambda_0$ is the wave vector and λ_0 is the wavelength of the incident plane wave [47].

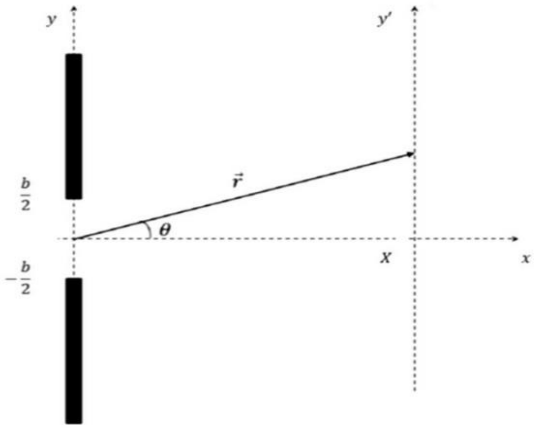

Figure 3. 4 - Representation of a perfectly conductive metal with a slit (Adapted from [47]).

Furthermore, this theory, under the same conditions, can also be applied to an array of N equally spaced slits instead of one single slit. The Fraunhofer theory is then mathematically formulated as [45]:

$$I(\theta) = I_0 \left(\frac{sin(\beta)}{\beta}\right)^2 \left(\frac{sin(N\alpha)}{sin(\alpha)}\right)^2 \tag{3.2}$$

where I_0 is the contribution of each individual slit to the overall irradiance [45].

3.2.3. Kirchhoff Diffraction Theory

Huygens–Fresnel diffraction results can be obtained from the Kirchhoff theory, considering the scalar wave equation approximation. The scalar Kirchhoff wave equation is as follows [48]:

$$\nabla^2\psi + k_0^2\psi = 0 \tag{3.3}$$

Resorting to the Green theorem

$$\boldsymbol{\psi}(r) = \frac{1}{4\pi}\int\left[\frac{\partial\bar{\psi}}{\partial\boldsymbol{n}}\frac{e^{ik_0 r}}{r} - \bar{\psi}\frac{\partial}{\partial\boldsymbol{n}}\frac{e^{ik_0 r}}{r}\right]dS \tag{3.4}$$

where S represents the entire surface, considering that it extends to ±∞, as presented in figure 3.4, is usually the standard approach for finding solutions [47][48].

Based on the equation above, Kirchhoff considered an approximation where $\psi = 0$ and $\partial\bar{\psi}/\partial n = 0$ on the right side of the surface, and that $\psi = \psi_0$ in the slit region, where ψ_0 is the field intensity of the incident wave without any disturbances [47] [48].

The Kirchhoff approximation assumes that the field inside the aperture is the same as the excitation field without the presence of the aperture. The approach works for apertures that are

large compared to the wavelength of the incident radiation, however the assumption fails near the edges of the aperture, and consequently the Kirchhoff approximation becomes inaccurate for small apertures [48] [49].

3.2.4. Bethe-Bouwkamp Diffraction Theory

In an effort to overcome the shortcomings of Kirchhoff's theory when it came to subwavelength slits, in 1944, Hans Albrecht Bethe derived an analytical solution for the electromagnetic field near a subwavelength circular aperture, in a perfect conductive metal surface, propagating along z and polarized along the x direction. The theory is based on three main assumptions: the incident and reflected waves coexist over the metal surface; the metal's conductivity is infinite so that the electromagnetic wave does not penetrate the surface; the electric field component, $\overline{\boldsymbol{E}}$, is tangential to the surface and the magnetic field component, $\overline{\boldsymbol{H}}$, is perpendicular to it [45].

If x, y and z correspond to the rectangular coordinates originating at the center of the circular aperture, and the z axis is perpendicular to the aperture plane, the aperture region can be defined by $x^2 + y^2 \leq a^2$, where a corresponds to the aperture's radius. According to Bethe, it is possible to calculate the electromagnetic field inside and around the circular hole. The expressions that characterize the electromagnetic fields are defined by [47]:

$$\begin{cases} \bar{E}_z = 2jkz - \dfrac{4}{\pi} jkau\,(1 + v\,arctan(v)) \\ \bar{E}_x = jkx - \dfrac{2}{\pi} jkx\left(arctan(v) + \dfrac{v}{1+v^2}\right) \end{cases} \tag{3.5}$$

$$\begin{cases} \bar{H}_z = -\dfrac{4ayu}{\pi a^2(u^2+v^2)\,(1+v^2)} \\ \bar{H}_y = 1 - \dfrac{2}{\pi}\left\{arctan(v) + \dfrac{v}{u^2+v^2}\right\} + \dfrac{2(x^2 - y^2)v}{\pi a^2(u^2+v^2)(1+v^2)^2} \\ \bar{H}_x = -\dfrac{4xyu}{\pi a^2(u^2+v^2)\,(1+v^2)} \end{cases} \tag{3.6}$$

where $x = a\sqrt{(1-u^2)(1+v^2)}cos\varphi$, $y = a\sqrt{(1-u^2)(1+v^2)}sin\varphi$ and $z = auv$, with $0 \leq u \leq 1$, $-\infty < v < +\infty$ and $0 \leq \varphi \leq 2\pi$ [47].

The theory claimed to satisfy Maxwell's equations as well as the boundary conditions everywhere, however, in 1950 Bouwkamp concluded, upon reviewing Bethe's theory that, in the near field region the results were not correct due to discontinuities in the considered boundary conditions. Bouwkamp then proceeded to modify the boundary conditions defined by Bethe and redefine the expressions for both the electric field and magnetic field. While the latter remained equal to that of Bethe, the expression for the electric field was modified as follows [47]:

$$\begin{cases} \bar{E}_x = -\dfrac{4jk}{3\pi}\dfrac{2a^2 - x^2 - 2y^2}{\sqrt{a^2 - x^2 - y^2}} \\ \bar{E}_y = -\dfrac{4jk}{3\pi}\dfrac{xy}{\sqrt{a^2 - x^2 - y^2}} \\ \bar{E}_z = 0 \end{cases} \tag{3.7}$$

In essence, when light passes through a hole, it drives surface current and accumulates charge at the edges of that hole. The accumulated charge enhances the electric field inside the hole, thus enhancing the far field diffracted light. Therefore, a metallic aperture can focus and transmit electromagnetic waves with increased efficiency, acting as an antenna. This occurrence was first contemplated by Bethe leading to the development of his theory of light diffraction, which was then corrected by Bouwkamp [37]. For this reason, the Bethe-Bouwkamp diffraction theory has revealed to be of great importance, especially in recent years, due to the increasing interest in optical antennas with a subwavelength size (optical nanoantennas) for various applications in different fields.

However, classic diffraction theories do not predict the existence of extraordinary optical transmission (EOT) nor the generation and propagation of surface plasmon polaritons (SPPs) that give rise to the unique optical properties that nanoantennas are associated with. Hence, these phenomena cannot be analysed or supported by such theories. Wave propagation theories regarding light-matter interactions can better describe the overall phenomenon.

3.3. Light-matter Interactions

3.3.1. Drude-Lorentz Model

The Drude-Lorentz model relates the dielectric function to the incident wavelength or frequency. By analysing the value of $\bar{\epsilon}_{DL(w)}$ it is possible to locate the wavelengths associated to the excitation of surface plasmon polaritons [45].

The behavior of the free electrons in a metal can help to characterize the interaction between the EM radiation and the metal in question. According to the classical Drude model, free electrons oscillate 180º out of phase relative to the driving electric field and, as a result, most metals have a negative dielectric constant at optical frequencies. Also, at optical frequencies, the free electron gas in the metal can sustain surface charge oscillations also known as plasmon polaritons, which are characteristic of the interaction between light and metal nanostructures [50].

In the XX century, the Drude-Sommerfield model was developed by Arnold Sommerfeld, combining the classical Drude model with quantum mechanical Fermi-Dirac statistics. The model describes the free electrons movement in a metal, assuming the conductive material (metal) as neutral since the negative electron charge is compensated by the positive ions charge [47].

However, the Drude-Sommerfield model is only accurate for applications in the infrared region of the spectrum. For other wavelengths, the contribution of the bound electrons must be

considered. The Drude-Lorentz model characterizes the dielectric function of the metal considering the contribution of the free electrons as well as the harmonic oscillations caused by the bound electrons, making this model a much better representation of the reality. The bound electrons and interband transitions are responsible for the resonant behavior of the imaginary part of the dielectric function and for the dispersive behavior of the real part [47] [50]. Considering all the phenomena contemplated by the previous models, the Drude-Lorentz model leads to the following equation [47]:

$$\bar{\epsilon}_{DL(w)=}\varepsilon_{\infty} - \sum_{n=0}^{\infty} \frac{f_n {w_p}^2}{(w^2 - {w_n}^2) + jw\gamma_n} \tag{3.8}$$

where ε_{∞} represents the asymptotic value of the function when the frequency approaches infinity, w_p is the metal plasma frequency, w_n is the n-th resonance frequency, f_n is the oscillator strength of the n-th resonator and γ_n is the n-th damping coefficient [47].

3.3.2. Surface Plasmon

A plasmon is defined as a quantum of a plasma oscillation. In the same way that light consists of photons, plasmon oscillation consists of plasmons. Thus, plasmons are collective oscillations of the electrons in a plasma. These oscillations are traveling waves with a well-defined frequency and wave vector. When such oscillations exist at the interface between a conductor and a dielectric, such as a dielectric-metal interface, they are called surface plasmons (SPs).

It is important to emphasize that, at optical frequencies, metals are highly dispersive materials with finite conductivity. Plasmon oscillations can couple the light in the form of a surface wave creating surface plasmon polaritons (SPPs). Hence, surface plasmon polaritons are surface EM waves that propagate along a dielectric-conductor interface, constituted by free electrons of the conducting material that collectively oscillate in resonance with the incident light [47].

A polariton is in fact the result of strong coupling between electromagnetic waves and an electric or magnetic dipole [45]. For a dipole structure, such as an array of slits, an aperture or even a corrugation on the surface, where light is incident on, the photons can excite coherent fluctuations of free electron charges at the metal boundary, creating plasmon oscillations. Such oscillations can couple with the incident light creating polaritons that will propagate at the interface [45].

The resonant interaction between the surface charge oscillation and the electromagnetic field of the light gives rise to unique properties. The presence of SPPs helps to concentrate and channel light using subwavelength structures, which leads to an electric field enhancement that can be used to manipulate interactions between light and matter and improve the transmission of light by the structure [51]. However, for polaritons to be created, the metal needs to exhibit an electric permittivity with a negative real part at the frequency of the incident light. Hence gold, silver, platinum, or aluminum are typically the materials of choice since all of them satisfy this

condition. Also, the vector component of the incident light parallel to the interface should be matched with the wave number of the SPP [47].

In a metallic nanoparticle, on the other hand, the confined geometrical boundaries support a localized surface charge oscillation, a phenomenon known as localized surface plasmon (LSP). Localized surface plasmons are therefore the result of the confinement of a surface plasmon in a nanoparticle smaller or of the same size of the wavelength of the incident light that excited the plasmon. LSPs are non-propagating excitations of the electron plasma coupled with the electromagnetic field and can be excited by direct light illumination.

As already mentioned, the excitation of surface plasmons can result in resonance and, consequently, in the creation of their polaritons. Surface plasmon resonance (SPR) depends on the size, shape, and index of refraction of the metal as well as the optical constants of its surrounding [52].

There are a few different methods to excite surface plasmons, to create polaritons. One way is to use electron beams in order to exploit the electrons scattering energy, transferred to the plasma's bulk, and originating a wave vector parallel to the surface [45]. A surface plasmon is created with this wave vector, and since it interacts with any electromagnetic wave, the polariton is generated [45]. An additional possibility is to use photons to excite a surface plasmon polariton, which is going to have the same frequency and momentum. However, the excitation of a free electron on the surface by an incident photon does not lead to the creation of polaritons, only to the creation of surface plasmon. Since the photon has more momentum than a surface plasmon polariton they cannot couple, thus no polariton is created. Still, if the momentum of the photon is reduced, which can be achieved by using a grating - an array of slits, grooves, apertures, holes, or a rough surface – incident photons will scatter at the surface, creating a surface plasmon with the same wave vector than the parallel component of the scattered wave, but that also interacts with the scattered wave, originating the polaritons [45].

Both LSPs excited in metal nanoparticles and SPPs propagating at the dielectric-conductor interface are of interest since both phenomena can lead to resonant behavior and thereby to light concentration and increase in absorption. These exceptional properties led the field of plasmonics, a subfield of nanophotonics studying the manipulation of light coupled with electrons at the nanoscale, to rapidly expand as an area for materials and devices research [53].

3.3.3. Extraordinary Optical Transmission (EOT)

Light passing through a small aperture is a phenomenon that has been attracting scientific interest ever since the discovery of the concept of diffraction in the XVII century. An opaque screen with an aperture can be considered as the simplest form of an optical element, which is one of the main reasons for the large interest in the phenomenon. Also, its interaction with EM radiation can lead to a wide range of physical phenomena [38].

Eventually, during the XX century, the scientific interest started to turn towards light passing through apertures of subwavelength dimensions. The first diffraction theory by a single slit with subwavelength dimensions was developed by Bethe and later by Bouwkamp, resulting in the

Bethe-Bouwkamp diffraction theory. The theory predicted that the power transmitted through the slit would decrease as the diameter of the slit decreased far below the radiation wavelength. However, these predictions were refuted in 1998 when Ebbesen observed the so-called extraordinary optical transmission (EOT) phenomenon for the first time [47].

Extraordinary optical transmission (EOT) is defined as an optical phenomenon in which a structure, containing subwavelength apertures in an opaque screen, transmits more light than would be expected. In EOT, the nanostructure enables a several orders of magnitude larger transmission efficiency than that predicted by the classical aperture theory [32]. In Ebbesen experiments, this nanostructure was an array of cylindrical holes, with a certain periodicity constant, hole diameter, and thickness. The array displayed sharp peaks in transmission for wavelengths as large as ten times the diameter of the holes. For these wavelengths, the transmission efficiency (normalized to the total area of the holes) could even exceed unity. These unique optical properties are due to plasmons coupling with light on the surface of the metal film thus creating polaritons (SPPs) [54].

The EOT phenomenon offers the possibility of a variety of applications due to the high transmission efficiencies and the high local field enhancements that can be achieved [39]. The discovery has already led to major developments in the nano-optics area, such as the creation of the optical nanoantenna, and can certainly serve as a base for other new optical devices and technologies.

3.4. Photovoltaic Effect and the Solar Cell

The photovoltaic effect was first observed by Henri Becquerel in 1839 and constitutes the foundation of photovoltaics, the most direct way to convert solar radiation into electricity. Solar cells are photovoltaic devices that use semiconducting materials to convert radiation into electrical energy through the photovoltaic effect. When incident light reaches the device, the absorption of photons occurs in the semiconductor material, so this material must be able to absorb a large part of the solar spectrum [5].

These cells are composed by two different types of semiconductors with different values of electron concentration: the n-type semiconductor, that has an excess of electrons and the p-type semiconductor, with a lack of electrons having more holes than electrons. The semiconductors are joined, forming a p-n junction across which the photovoltage is developed.

Once the incident photons are captured by the electrons, the electrons jump from the valence band to the conduction band, leaving behind a hole and creating an electron-hole pair, as exemplified in figure 3.5. The incident light will break the thermal equilibrium condition of the junction and the free electrons in the depletion zone will flow to the n-type side of the junction. In a similar manner, the holes will move to the p-type side of the junction. As the concentration of electrons becomes larger in one side (n-type side) and the concentration of holes becomes larger in the other (p-type size), the p-n junction will start to behave similarly to a battery cell and a voltage is set up (photovoltage). Finally, electric current can be generated if a small load is connected across the junction [55].

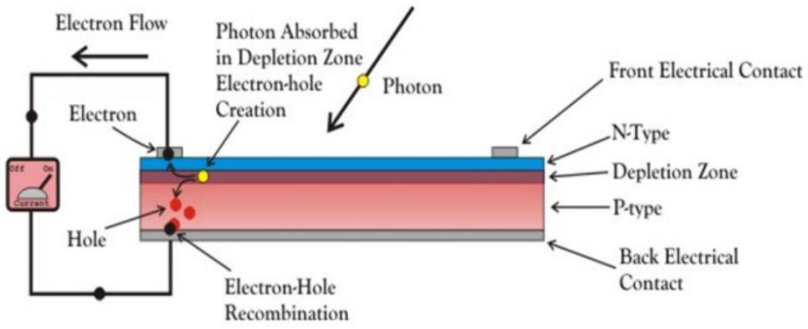

Figure 3. 5 - Solar cell structure (Adapted from [55]).

3.4.1. PIN Junction Solar Cell

The PIN structure consist of three differently doped regions: an n-doped region, a p-doped region and an intrinsic or undoped region in between the n- and p-doped regions. Figure 3.6 shows a simplified structure of a PIN junction.

For a certain semiconductor to become doped, extra materials commonly called dopants need to be added to the semiconducting material in question. Dopants can be classified as p-type dopants or acceptors, if they originate p-type semiconductors or n-type dopants or donors, if they originate n-type semiconductors. The materials used as dopants depend on the semiconducting material one is trying to dope.

Silicon is a material with four electrons in the valence band. When doping silicon with a n-type dopant, extra valence electrons that are unbonded from individual atoms are added to the material. If doped with a p-type dopant, which usually have only three valence electrons, a hole is left where the fourth electron would exist if the semiconductor was pure (intrinsic) silicon. The concentration of the dopant used correlates with the charge carrier concentration of the material. In general, increasing doping results in increasing conductivity, due to the higher concentration of charge carriers. The intrinsic semiconductor, in the middle layer of the structure, has under thermal equilibrium, equivalent concentrations of both electrons and holes.

Electrons and holes generated by photons absorbed in the doped layers typically recombine before reaching the contacts and being collected. Thus, it is assumed that the carriers originated in the doped layers do not contribute to the generation of photocurrent in the solar cell [56]. The active absorption of light occurs mainly in the intrinsic layer, that is typically much larger than the doped layers.

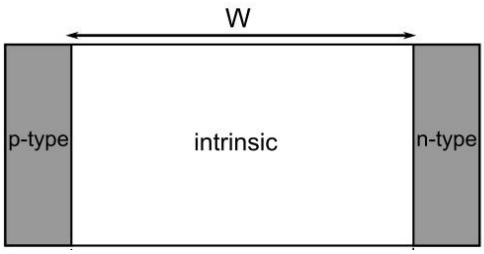

Figure 3. 6 - Simplified structure of a PIN junction (Adapted from [56]).

In the frequency domain, the electron and hole current densities in the *i*th layer, $J_{ip(x,w)}$ and $J_{in(x,w)}$, respectively, follow the continuity equations (3.9) and (3.10) [57]. The v_{in} and v_{ip} are the electron and hole drift velocities, respectively, and $G_i(x,w)$ refers to the electron-hole optical generation rate [57].

$$\frac{iw}{v_{in}} J_{in(x,w)} = \frac{d\,J_{in(x,w)}}{dx} + G_i(x,w) \tag{3.9}$$

$$\frac{iw}{v_{ip}} J_{ip(x,w)} = \frac{d\,J_{ip(x,w)}}{dx} + G_i(x,w) \tag{3.10}$$

The authors of [57] discuss and define in greater detail the expressions and specifications that relate to the modelling of a PIN photodiode. Although the article depicts a structure slightly different from the PIN solar cell portrayed in this subchapter and subsequently implemented and simulated in chapter 5, the validity of certain requirements regarding, for example, the materials used, still holds.

3.4.2. CIGS Solar Cell

The CIGS (copper indium gallium selenide) solar cell has a complex multiplayer structure exemplified in figure 3.7, usually composed of 6 different layers: a glass substrate, a metallic molybdenum (Mo) layer, a p-type CIGS absorber, a n-type buffer layer of cadmium sulphide (Cds), a thin layer of highly resistive intrinsic zinc oxide (ZnO) and a layer of aluminum doped zinc oxide (ZnO:Al) [58].

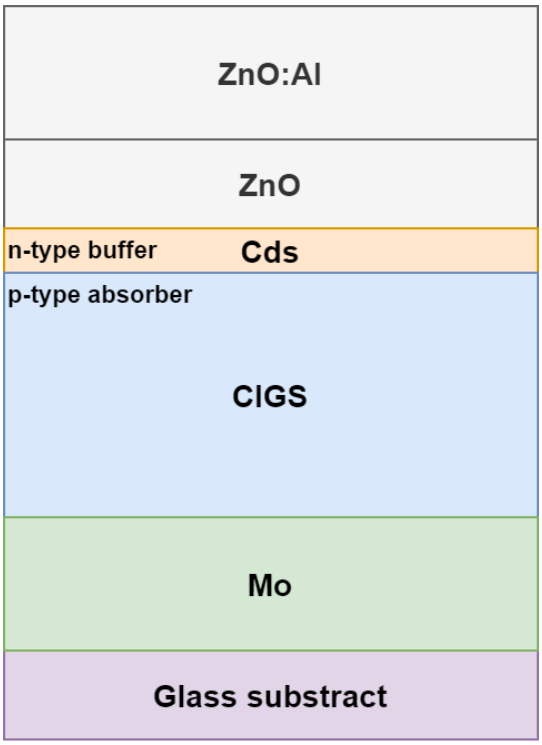

Figure 3. 7 - CIGS solar cell structure.

The aluminum doped zinc oxide (Zno:Al) and molybdenum (Mo) layers allow the cell to have good conducting abilities without disturbing other processes in the cell. The thin layer of highly resistive ZnO helps to protect the surface from possible damage in subsequent process steps. The n-type Cds buffer layer provides structural stability to the structure and fixes the electrostatic conditions within the following absorber layer. These two layers, the n-type Cds buffer layer and the p-type CIGS absorber layer, constitute the p-n junction of the cell, where most of the incident sunlight is absorbed. The CIGS absorber layer is considered to be the most vital in the entire solar cell since it is a direct band gap semiconductor material and has a large absorption layer [58].

4. Model Structure and Configuration

4.1. COMSOL Multiphysics® Software

To study the problem submitted in this dissertation, 2D and 3D models of different solar cell structures are established, and the corresponding optical response of each model is computed. All the simulations are developed using *COMSOL Multiphysics*®, a software platform where is possible to model real life designs and processes in a virtual environment. It incorporates all the steps in the modelling workflow such as defining geometries, material properties, and the physics that describe specific phenomena in order to solve the models and produce accurate results.

The software allows simulation of physics-based systems described by partial differential equations (PDEs). However, in most of the problems these equations cannot be solved by analytical methods. Thus, different types of discretization methods can be used to approximate the PDEs with numerical model equations, which can then be solved by numerical methods. Hence, the solution obtained by these methods is simply an approximation of the real solution to the PDEs. Those approximations are computed using the Finite Element Method (FEM) [59].

The FEM solves the PDE in an integral form, in which unknowns are discretized as sums over a set of basic functions defined on finite elements. The finite elements are assembled by using a mesh, which is a tessellation of the geometry resulting in the division of the model into small, simpler geometrically shaped elements, such as triangles for 2D or tetrahedra in 3D [60].

The physical phenomena involved in each model is incorporated in *COMSOL Multiphysics*® through “physics interfaces”, which consist of pre-built packages of physical equations and a choice of associated boundary conditions. Since *COMSOL Multiphysics*® is designed for “multiphysics” purposes, the software allows the incorporation and coupling of several different physical phenomena, *i.e.,* multiple physics interfaces. Also, despite the use of pre-built methods, it is possible to alter default numerical settings and there is total flexibility to combine and couple the pre-built methods with user-defined variables or equations [60].

4.2. 2D Model

Initially, the electromagnetic analysis is conducted on a 2D solar cell model, using the Finite Element Method (FEM) in *COMSOL Multiphysics*®.

In *COMSOL Multiphysics*®, when time variations are in place, the time dependent problem is usually solved by using a *Time Dependent* study or a *Frequency Domain* study. The first one is likely the most straightforward way to solve the problem, however this approach can be time consuming if small time steps are necessary to achieve the desired accuracy. On the other hand, if a *Frequency Domain* study is used, it can be assumed that all variations in time occur as sinusoidal signals which significantly simplifies the problem [61].

Electromagnetic analysis on a macroscopic level involves solving Maxwell's equations subject to certain boundary conditions [61]. To solve the modelling problem in question, which involves the time-harmonic Maxwell's equations, it is assumed that all material properties are constant with respect to field strength, and that the fields will change sinusoidally in time at a known frequency or range of frequencies. Thus, the problem can be treated as *Frequency Domain*. Moreover, as the effective wavelength is comparable to the sizes of the objects that are present in the model, then the problem can be treated as a *wave electromagnetic* problem [62].

The **physics interface** available in *COMSOL Multiphysics*® for this type of modelling is the *Electromagnetic Waves, Frequency Domain* interface, which uses FEM to solve the frequency domain form of Maxwell´s equations. For this interface, the dependent variable is the total electrical field and the governing equation being solved for is given by [61]:

$$\nabla\, x\, (\mu_r^{-1} \nabla\, x\, \boldsymbol{E})\, - k_0^2\, \varepsilon_{rc}\, \boldsymbol{E} = 0 \tag{4.1}$$

where μ_r is the relative permeability, ε_{rc} is the relative permittivity, k_0 is the wave number, and $\boldsymbol{E}$ is the electric field. The wave number of free space, k_0, is defined as [61]

$$\mathrm{k_0} = \mathrm{w}\sqrt{\varepsilon_0 \mu_0}\, = \frac{\mathrm{w}}{\mathrm{c_0}} \tag{4.2}$$

where c_0 is the speed of light in vacuum.

In 2D models, the electric field varies with the out-of-plane wave number k_z as presented in expression 4.3 [61].

$$\boldsymbol{E}(x, y, z) = \widetilde{\boldsymbol{E}}(x, y) e^{-ik_z z} \tag{4.3}$$

The **geometry** of the 2D model is represented in figure 4.1 and is constituted by an amorphous silicon (a-Si) cell (in blue) and by a dielectric layer on top, which in this case is air. Although a typical solar cell is composed by n-type and p-type layers, as previously explained in subchapter 3.4, the three layers represented in the nanostructure are all composed of intrinsic amorphous silicon. The absorption of light in a solar cell occurs mainly in the intrinsic region of the cell hence, it can be assumed that the n-type and p-type doped layers do not contribute significantly to the generation of photocurrent in the solar cell [56]. Therefore, for the purpose of simplifying the following simulations the nanostructure illustrated in 4.1 is considered as an actual a-Si PIN solar cell. The three layers have heights of 80 nm, 200 nm and 150 nm.

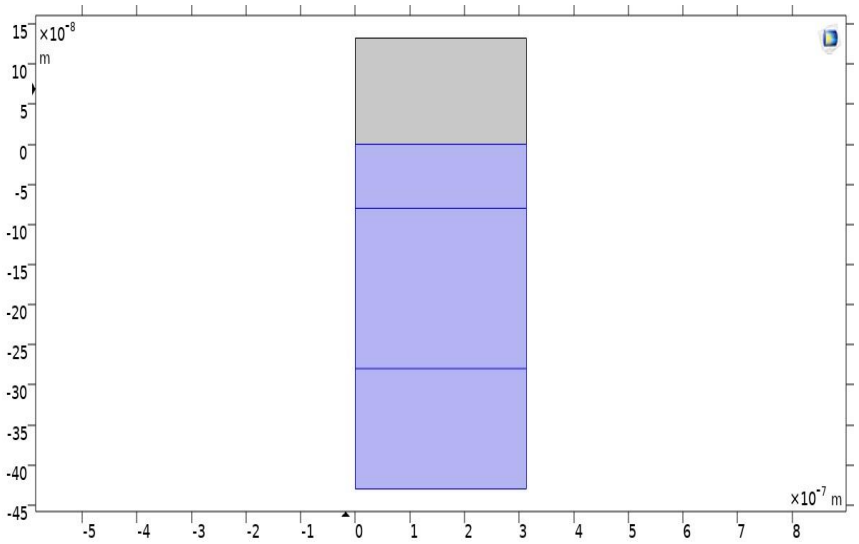

Figure 4. 1 - Schematic representation of the simulated 2D structure.

The choice of **materials** and corresponding models is a key part of the modelling process since the governing equations and the constitutive relations of the mathematical model depend on the physical properties of the material [63]. The selected physics interface, *Electromagnetic Waves, Frequency Domain*, is an optical module thus it is necessary to characterize the optical constants n and k of each material, where n is the refractive index and k the extinction coefficient. They relate to the interaction between a material and incident light, where n is associated with refraction and k with absorption.

For the 2D model in question, the air is modelled by the 1996 Ciddor model and the amorphous silicon (a-Si) is modelled by Pierce and Spicer in 1972. The complex refractive index function $(n + ik)$ of both materials is represented in figures 4.2 and 4.3. The window plot was adjusted to the wavelength simulation range*, i.e.,* $[250\ 1500]$ nm, in order to display the wavelength values that are going to influence the simulations. The models used for each material are retrieved from an online database [64], which presents the same models as the ones available on *COMSOL Multiphysics*®.

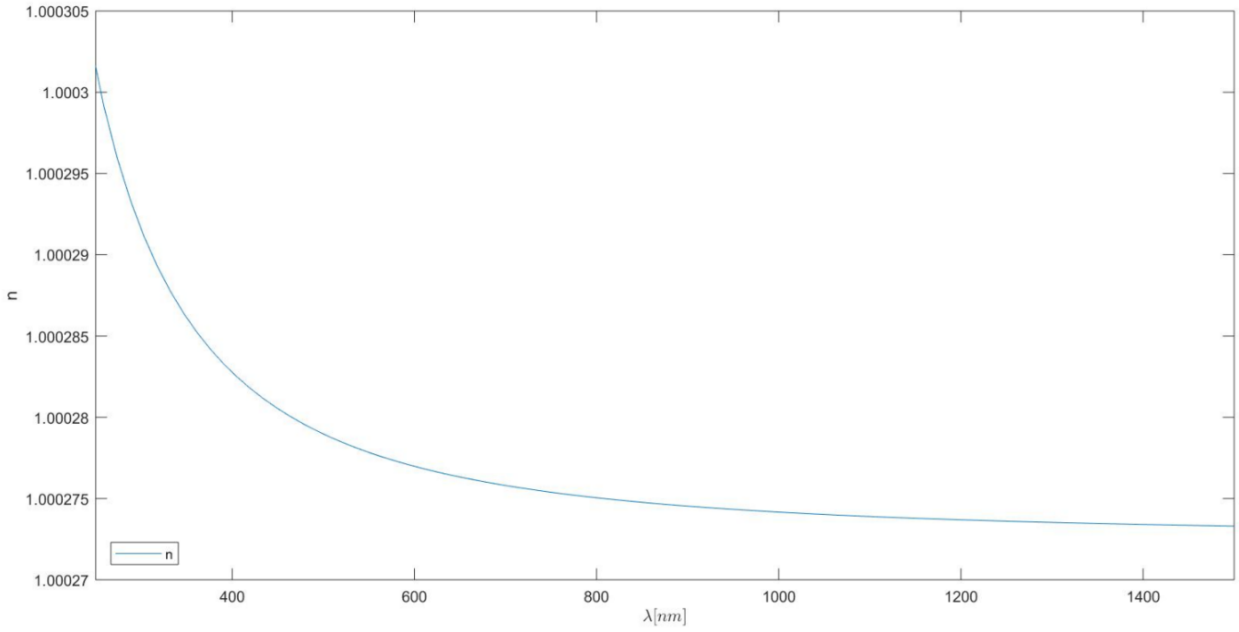

Figure 4. 2 - Air complex refractive index function from the 1996 Ciddor model.

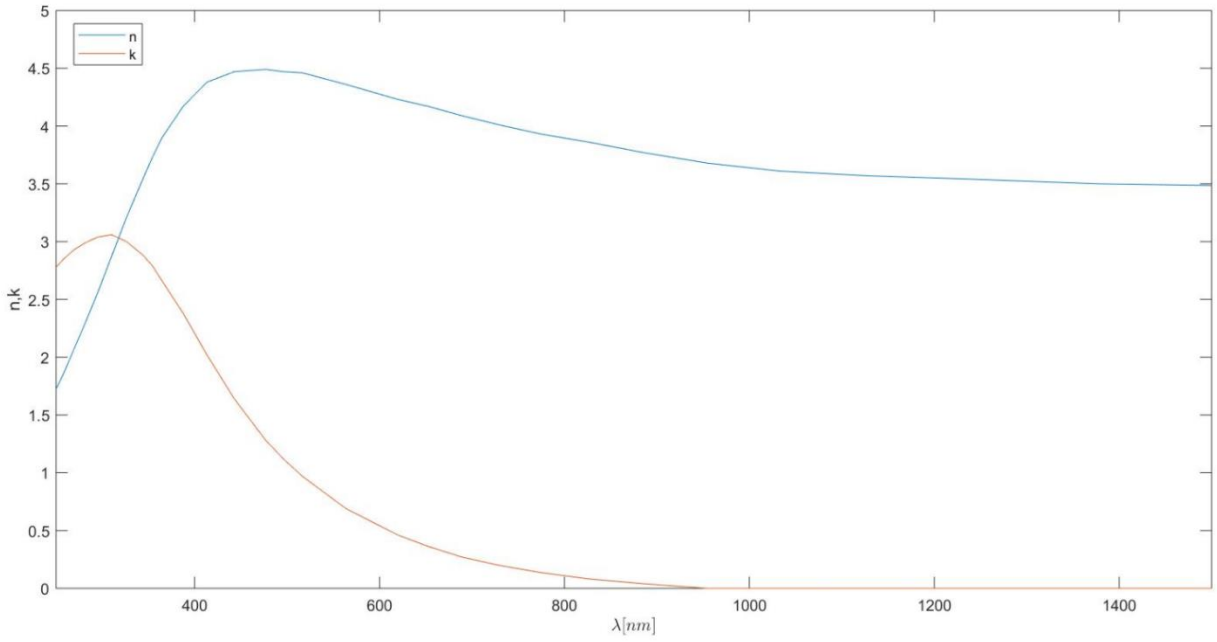

Figure 4. 3 - Amorphous silicon (a-Si) complex refractive index function from the 1972 Pierce and Spicer model.

It is also vital to define the **boundary conditions** when developing the model. The boundary conditions represent certain constraints that are imposed on the real system. The boundary conditions along with the governing equations are used to obtain a numerical solution for the modelling problem.

The physics interface in use for this model includes several types of boundary conditions that can be implemented, with different characteristics thus serving distinct purposes. When

dealing with photonic devices, the *Scattering Boundary Condition* is usually the most common choice. This boundary condition serves as a condition for absorbing scattered waves propagating normally to the boundary. This attribute is important since it does not allow for internal reflections to take place, meaning that any field amplification verified in the structure is due to the structure's elements and not to any type of reflection with the boundaries. Since this was the type of boundary condition that best suited the model in question, two different scattering boundary conditions were defined.

In the scattering boundary condition 1 represented in figure 4.4, the incident electric field, defined by $|E_0| = 1\mu\,\mathrm{V/m}$, is generated on top of the structure. The electric field amplitude should be parallel to the nanoantenna array that is later going to be added to the cell, in order to reach the nanoantenna apertures in a tangential manner. For a metal nanoantenna in the visible and near-infrared regions, the EM field wave vector must have a parallel component to the surface of the metal in order for polaritons to be originated and therefore, for the EOT phenomenon to take place [45]. Hence, the incident electric field amplitude is defined in the x axis direction, as $|\mathrm{E_x}| = \mathrm{E_0\ V/m}$ and $|\mathrm{E_y}| = |\mathrm{E_z}| = 0\ \mathrm{V/m}$. The EM field amplitude will vary in the x direction, but the EM field wave will propagate in the y axis direction.

The scattering boundary condition 2, represented in figure 4.5, involves all the remaining external limits of the structure and has no electric field defined. With a null electric field and no incident electric field either, this boundary condition is going to absorb any scattered waves propagating normally to the boundary itself. When the wave is not completely perpendicular to the boundary, the perpendicular component of the wave will still be absorbed but the wave will be partially reflected.

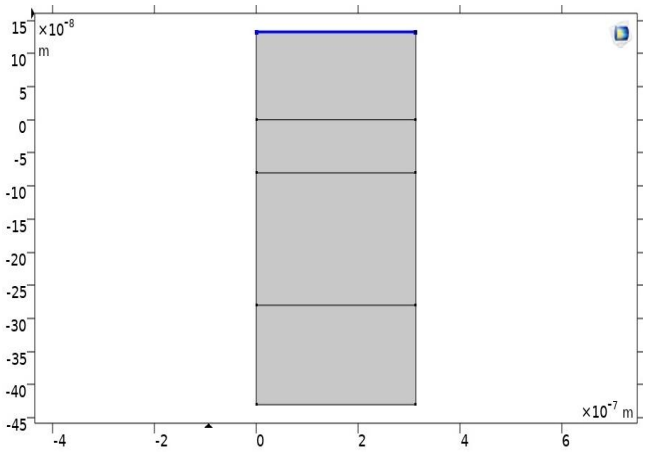

Figure 4. 4 - Scattering Boundary Condition 1.

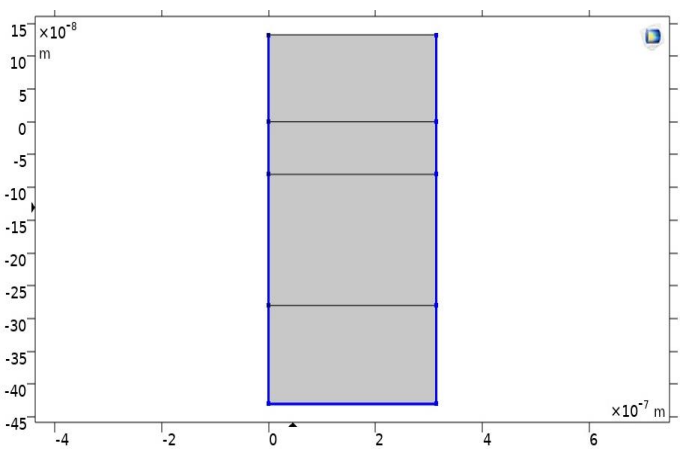

Figure 4. 5 - Scattering Boundary Condition 2.

The waves emitted at scattering boundary condition 1 are vertically propagating in the y axis direction. Hence, they are not perpendicular to the side limits of the scattering boundary condition 2, so they will not be absorbed by those limits and can propagate throughout the entire structure.

However, it is noteworthy that in passing between layers the electric field waves can have components that are perpendicular do the side limits of boundary condition 2. Also, the electric

field waves are in fact perpendicular to the bottom limit of the scattering boundary condition 2, which will absorb them, resulting in a decreasing value of the electric field along the structure as the waves reach closer to that bottom limit. Ultimately, this occurrence leads to the value of the electric field in that area being close to zero (but not null).

The finite element method (FEM) is used to solve the PDEs and, like any other discrete numerical method, will introduce some numerical error [60]. The accuracy of the obtained solution is related to the defined **mesh**. Assuming there are no singularities, a denser, finer mesh would generate a more accurate solution. However, this type of mesh will require increased computer memory usage and slower simulation time [63]. Thus, it is important to define an appropriate mesh by locating a balance between accuracy and velocity of simulation.

The software supplies a *physics-controlled mesh,* which automatically refines the mesh in the required regions. This was the form of mesh chosen to be implemented in the models, in order to improve computational accuracy and obtain a more precise result.

4.2.1. Introduction of the Nanoantenna

At this time, an aluminium (Al) nanoantenna with apertures is introduced on top of the silicon cell, in order to study the differences in the optical response of the cell with and without a nanoantenna.

The aluminium model that was used is the Rakic, obtained through a Drude-Lorentz fitting of experimental data [64]. The complex refractive index function $(n + ik)$ is illustrated in figure 4.6.

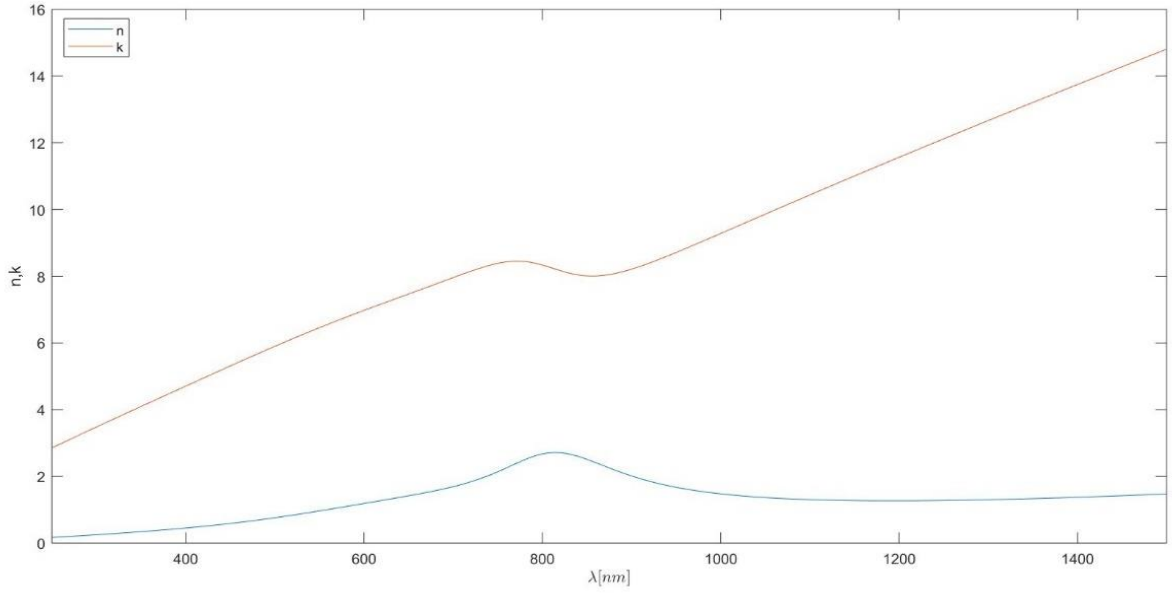

Figure 4. 6 - Aluminium complex refractive index function from Rakic's Drude-Lorentz fitting.

Aluminum was chosen since it is usually considered to be the best material to obtain gain along all visible region, mainly due to its complex refractive index function $(n + ik)$ [65]. When

analysing figure 4.6, it is possible to verify that throughout the entire wavelength range the extinction coefficient, k, has a greater value than the refractive index, n. The complex dielectric function is related to the complex refractive index function by $\bar{\epsilon} = \epsilon' + j\epsilon'' = \bar{n}^2 = (n + ik)^2$ such as $\epsilon' = n^2 - k^2$ and $\epsilon'' = 2nk$. Taking this into account, this material's dielectric function will have a large negative real part and a an almost null imaginary part until around 400 nm. These characteristics make this material the best choice to secure gain along the visible region of the light spectrum [65].

The aluminium nanoantenna implemented in the 2D model, illustrated in figure 4.7, is an array with 9 slits, each of them with a diameter d_NA equal to $(120/9)$ nm, and a periodicity of $a0\_NA$ equal to $(0.3/9)$ μm. Also, the height of the nanoantenna is equal to $a0\_NA$.

Moreover, the width is the same along the entire structure and was defined as $x\_n\_disp * a0\_NA + d\_NA$, where x_n_disp is equal to the number of slits in the nanoantenna. However, as seen in figure 4.7 the width of the nanoantenna is slightly different from the rest of the structure and equal to $a0\_NA - d\_NA$. Although surface plasmons propagate in the metal's surface, surface plasmon polaritons propagate in the interface between surfaces. If the nanoantenna was placed right next to the structure's boundary condition, it would not be possible to witness the presence of surface plasmons and consequently, of polaritons as accurately. So much so, that the first slits would probably present underwhelming results.

It is important to reference that all of the previously mentioned measurements were based on the optimized version of a 3D aluminium nanoantenna structure presented in [65], designed to sustain gain along the visible region of the light spectrum. Since the structure in question was a 3D model, the dimensions were altered in order to fit a 2D reality and be implemented in this specific solar cell model.

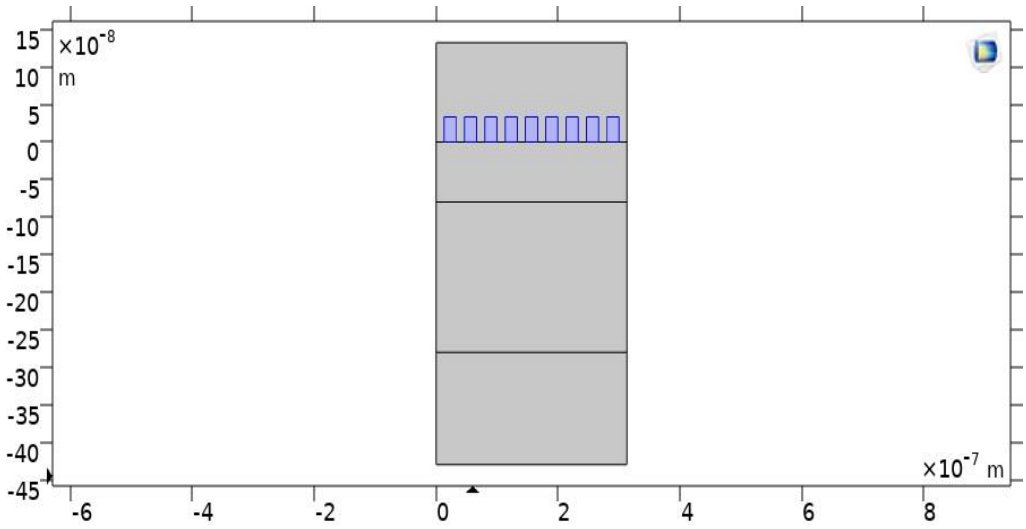

Figure 4. 7 - Schematic representation of the simulated 2D structure with nanoantenna.

The remaining measurements of the structure are the same for both 2D models (with and without the nanoantenna) to make the models consistent and be able to have a reference structure throughout all the simulations.

The simulation environment and conditions regarding materials, physics interface, boundary conditions and mesh are the exact same as the ones used for the 2D model without the nanoantenna. Thus, it is possible to meet the main purpose of the simulations presented in chapter 5, which is to identify and analyse the changes that occur when introducing a nanoantenna in a solar cell. Moreover, the focus of that analysis will be to try to detect the occurrence of the EOT phenomenon when the nanoantenna is added to the solar cell.

4.3. 3D Model

4.3.1. Amorphous Silicon (a-Si) Solar Cell Structure

To further deepen the study of a solar cell coupled with a nanoantenna it is important to analyse the performance of 3D models. The environment and conditions defined in a 3D model resemble actual reality in a more truthful way, so the optical response given by the cell and the occurrence of the EOT phenomenon can be examined in a more detailed and accurate manner. To do so, a 3D model of a solar cell structure is developed.

Similarly to what was established in 2D, two versions of the 3D model are created: without and with a nanoantenna, as represented in figures 4.8 and 4.9, respectively. As seen in figures 4.9 and 4.10, the nanoantenna is squared arrayed, composed by circular holes, with a periodicity of $a0\_NA$ equal to $0.3\mu m$ and a total number of 9 holes forming a 3x3 array. The nanoantenna thickness, t_NA, is equal to 50 nm and the diameter of the holes, d_NA, is equal to 120 nm.

The dielectric layer on top of the structure has a thickness of 200 nm and includes the nanoantenna layer, since the nanoantenna holes must contain the dielectric material in question, in this case air. The thickness of the solar cell layers, located bellow the nanoantenna, was based on the measurements of the 2D model layers but modified and adapted to a 3D reality, thus being substantially reduced in a proportional manner. The set of three layers has a total thickness of 21.5 nm.

The geometry of both 3D models (with and without nanoantenna) is the exact same except for the nanoantenna layer, which is not implemented in one of the models (without the nanoantenna).

Finally, it is important to mention once more that, alike what was established for the 2D model, all of the previously mentioned dimensions were based on the optimized version of an aluminium nanoantenna structure presented in [65].

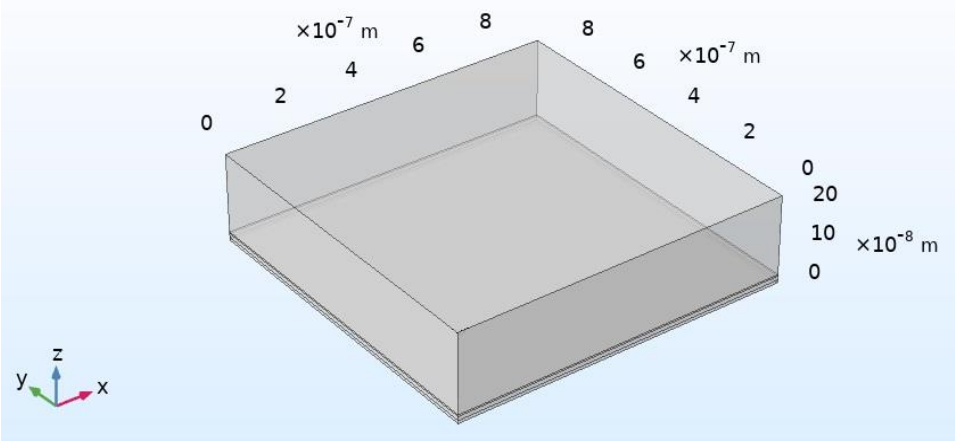

Figure 4. 8 - Schematic representation of the simulated 3D a-Si solar cell structure.

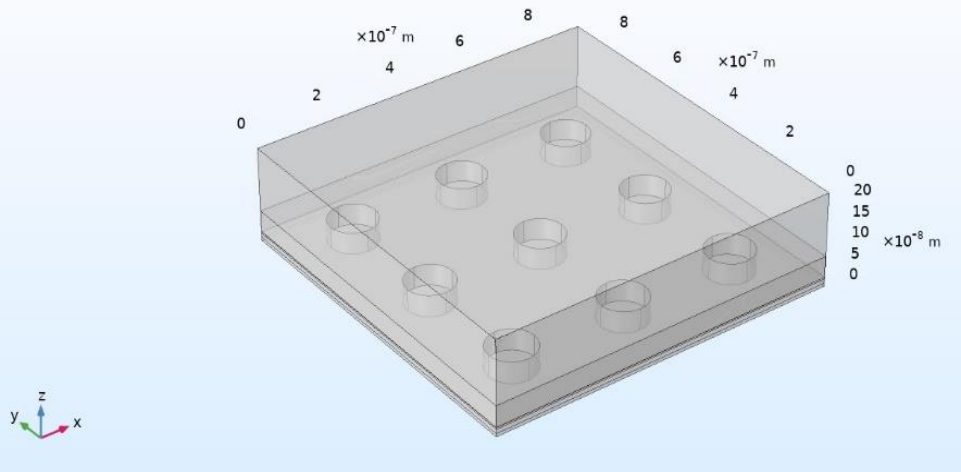

Figure 4. 9 - Schematic representation of the simulated 3D a-Si solar cell structure with nanoantenna.

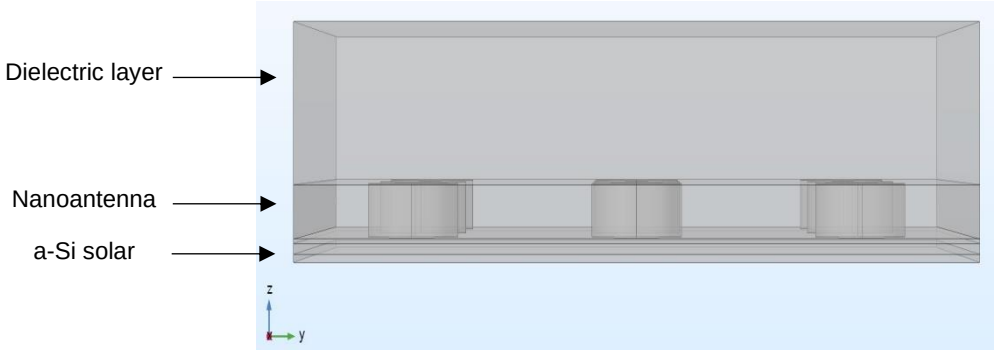

Figure 4. 10 - Side view of the simulated 3D a-Si solar cell structure with nanoantenna.

The materials of the 3D model are the same as those implemented in the 2D model. Therefore, the dielectric material is air, the solar cell material is amorphous silicon (a-Si), and the nanoantenna material is aluminium (Al).

An electric field, defined by $|\mathrm{E}_0| = 1\mu\,\mathrm{V/m}$, is generated on the top external boundary of the dielectric layer of the 3D structure, in both 3D models. The EM field is perpendicular to the

nanoantenna, having the opposite direction of the z axis, and it is defined in the generation port by $|\mathrm{E_x}| = |\mathrm{E_y}| = \frac{E_0}{\sqrt{2}}\ \mathrm{V/m}$ and $|\mathrm{E_z}| = 0\ \mathrm{V/m}$.

The remaining requirements regarding physics interface, boundary conditions and mesh are equivalent to the ones applied in both 2D models, described in subchapter 4.2. Also, those specifications are the same for both 3D models, with and without the nanoantenna. Once more, it is important to stress that in order to study the impact of combining a nanoantenna to a solar cell both in 2D and 3D, the assembled models must maintain a certain degree of similarity between them. Only in this way can it be possible to focus on the detection and assessment of possible field amplification and the EOT phenomenon.

4.3.2. PIN Solar Cell Structure

As previously mentioned, the solar cell implemented in the nanostructure described in the subchapters 4.2 and 4.3.1 is composed of only intrinsic amorphous silicon, since it is presumed that the n- and p-doped regions of solar cells do not significantly contribute to the production of photocurrent. Nevertheless, in an attempt to substantiate this assumption an a-Si PIN solar cell structure is developed and posteriorly subjected to several simulations to ultimately compare the results with the original 3D model (described in 4.3.1).

The model in question has the exact same geometry and dimensions as the original 3D a-Si solar cell structure characterized in subchapter 4.3.1. The specifications related to physics interface, boundary conditions and mesh are also equivalent to the ones defined for the original 3D a-Si solar cell structure and the electric field will be generated under the exact same conditions, already depicted in subchapter 4.3.1.

Figure 4.11 shows the dopant distribution in the different layers of the structure. The signed doping concentration is positive for net donor doping and negative for net acceptor doping. The intrinsic layer has equivalent concentrations of both electrons and holes, so the doping concentration should be close to zero. Hence, the top layer corresponds to the n-type layer, the bottom layer corresponds to the p-type layer, and the middle layer corresponds to the intrinsic layer.

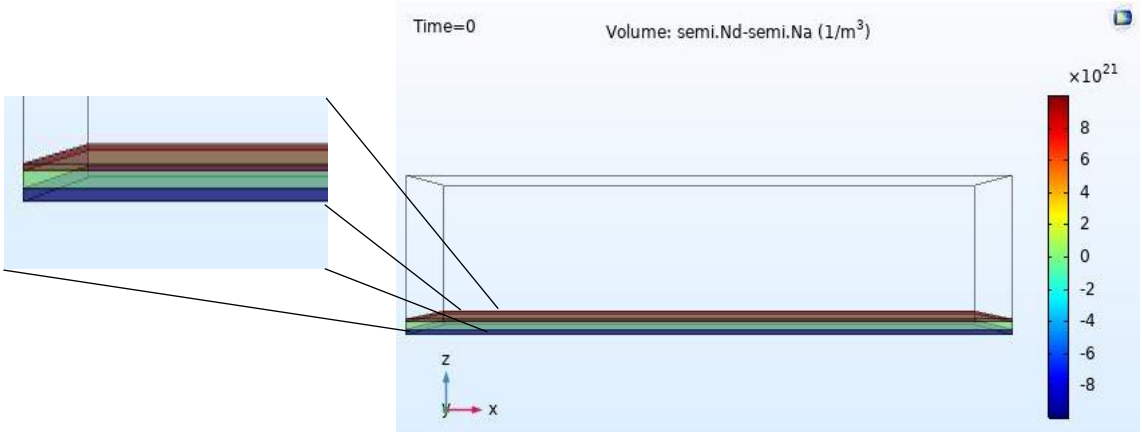

Figure 4. 11 - Dopant distribution of the PIN solar cell structure.

4.3.3. CIGS Solar Cell Structure

All the models depicted in this chapter have been, up to this point, constituted by an amorphous silicon (a-Si) cell. This type of cell is classified as a second-generation solar cell, also known as thin-film solar cells. However, there are other types of cells within this category, such as copper indium gallium selenide (CIGS) solar cells, characterised in subchapter 3.4.2.

The study and assessment of the output optical response of a 3D model using a different type of solar cell would be noteworthy. Therefore, based on the original 3D model characterized in subchapter 4.3.1, a 3D model with a CIGS solar cell structure is developed as exemplified in figure 4.12. It is important to note that, since the CIGS solar cell has a complex multiple layer structure, the thickness of the original 3D solar cell structure had to be increased in order to accommodate all the different layers. Nevertheless, the remaining specifications and conditions that were imposed, are the same as those defined for the previous models in 4.3.1. and 4.3.2.

As seen in figure 4.12, during the simulations of the CIGS solar cell structure with and without nanoantenna, the layer of aluminum doped zinc oxide (ZnO:Al) typically present in all CIGS solar cells is not considered. The optical constants of this particular material available in [64] have a defined wavelength range smaller than the one intended to be utilized in the subsequent simulations of all models, *i.e.,* $[250\ 1500]$ nm. Hence, if this layer had been maintained the study would have been conditioned by the smaller incident wavelength range and would not be comparable to results obtained by other models.

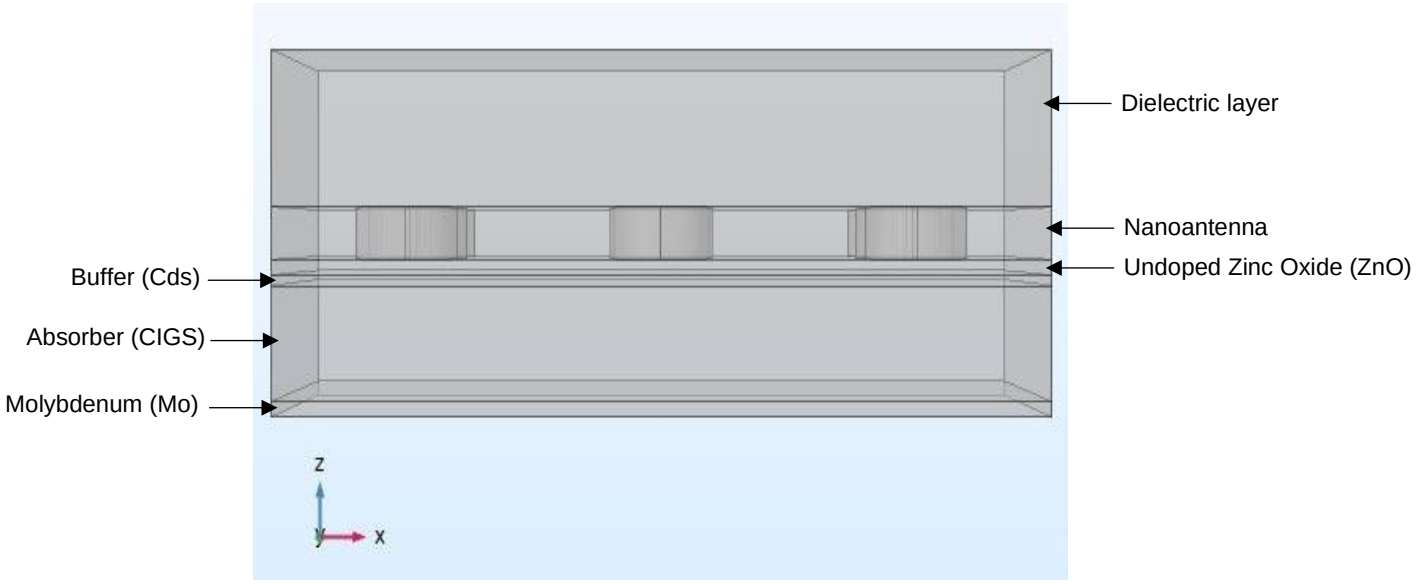

Figure 4. 12 - Side view of the simulated 3D CIGS solar cell structure (with nanoantenna).

5. Simulation Results

5.1. 2D Simulations

Initially, the output optical response of the 2D model without the nanoantenna is computed and analysed. Only later is the nanoantenna added to the model in order to compare the results obtained for both scenarios, with and without the nanoantenna.

The simulations that follow are accomplished using four different boundary probes, one at the end of each layer of the structure, as represented in figure 5.1. These probes analyse the maximum ratio between the electric field norm and the incident electric field norm, $\left|\frac{E}{E_0}\right|$. Moreover, the simulations are developed for a range between 250 nm and 1500 nm, with 250 equidistant wavelength points.

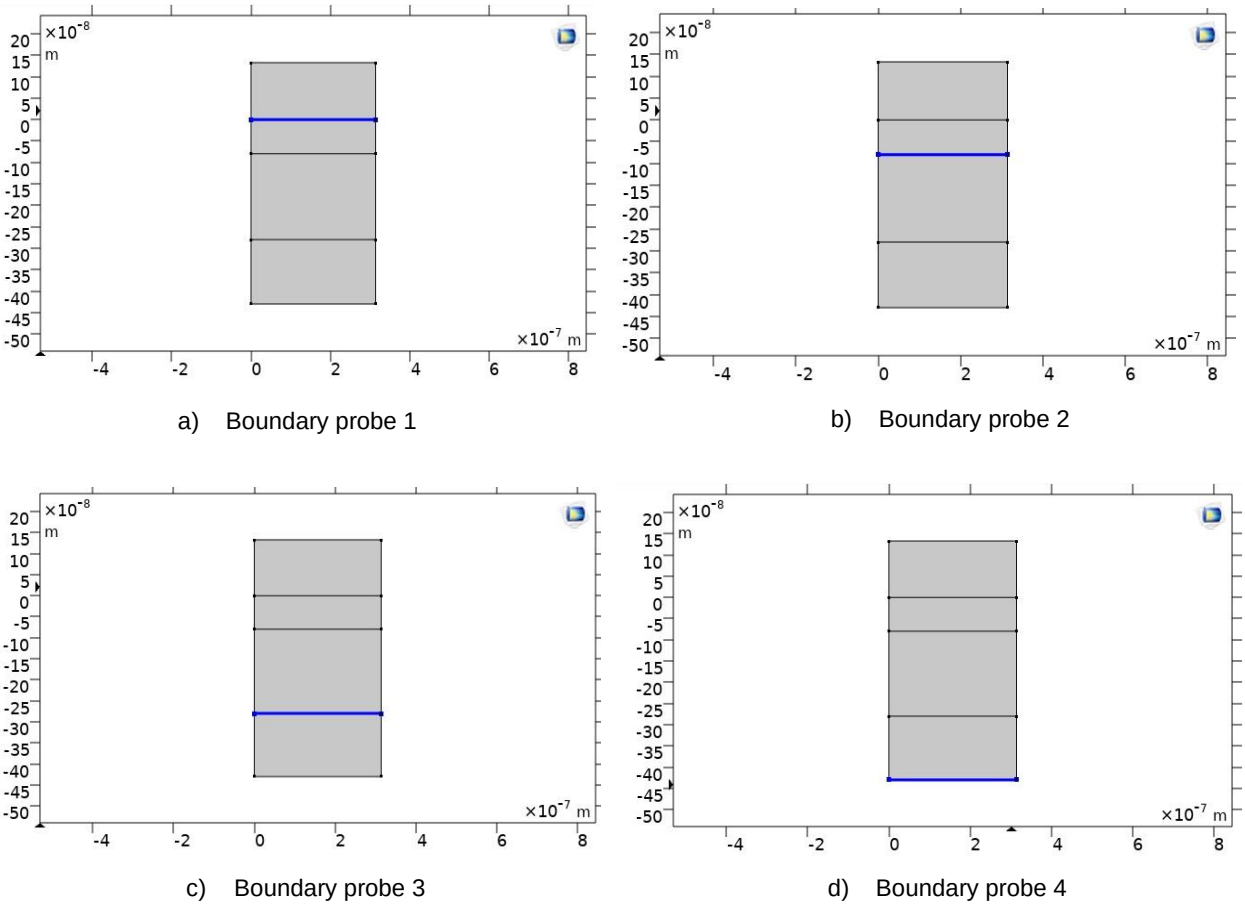

a) Boundary probe 1

b) Boundary probe 2

c) Boundary probe 3

d) Boundary probe 4

Figure 5. 1 - Boundary probes defined for the 2D model.

Figure 5.2 illustrates the optical response generated by the model without nanoantenna. Furthermore, figure 5.3 shows the normalized electric field for an incident wavelength of 775 nm, which corresponds to the energy gap value of a-Si (approximately 1.6 eV corresponding to 775 nm).

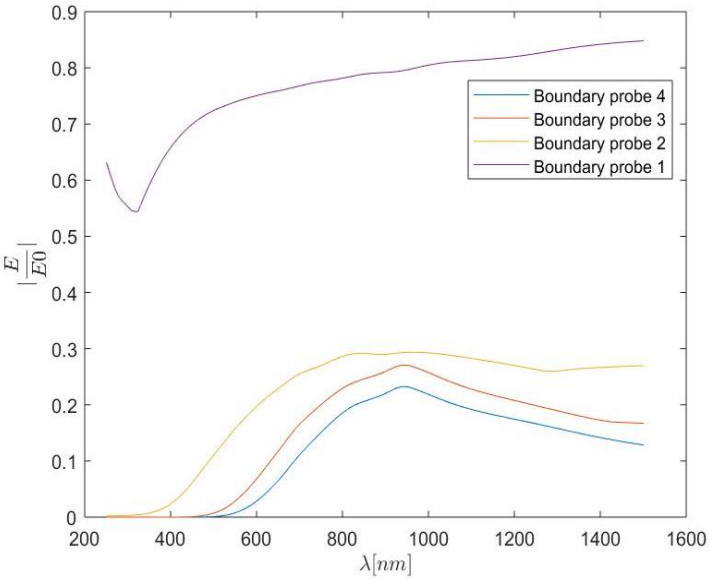

Figure 5. 2 - Optical response of the 2D a-Si solar cell structure.

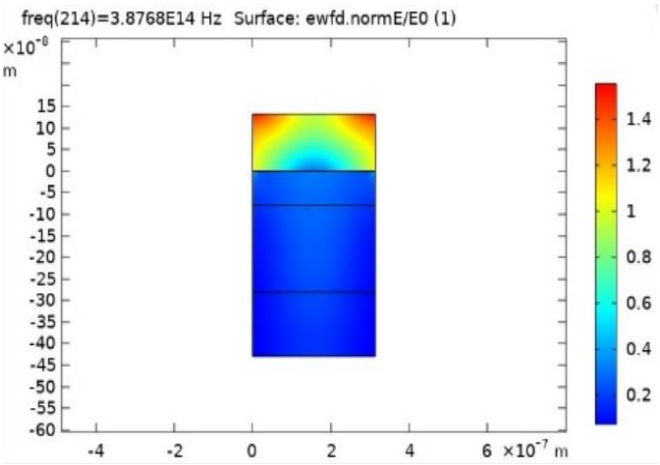

Figure 5. 3 – Electric field of the 2D a-Si solar cell structure for an incident wavelength of 775 nm.

As seen in figure 5.2, the ratio between the electric field norm and the incident electric field norm, $\left|\frac{\mathrm{E}}{\mathrm{E_0}}\right|$, does not reach values above or even equal to 1.

If the simulated structure had the ability to transmit more light than its incidence, then the value obtained for the ratio is equal or greater than 1, indicating the occurrence of Extraordinary Optical Transmission. The fact that this does not happen for the 2D model in question, means that the EOT phenomenon did not take place. However, this result is to be expected since without the presence of any subwavelength aperture, SPP's will not be generated, and extraordinary transmission cannot happen. It is important to underline that SPP's constitute the main agents of the EOT phenomenon in metallic nanoantennas functioning in the visible and near-infrared region of the light spectrum.

Since the amplification of the electric field is not verified in any of the layers of the structure, the electric field will simply decay along the propagation distance. As seen in figure 5.3, there is a substantial decrease of the electric field value as the EM waves propagate throughout the air layer of the structure, reaching the solar cell with values much lower than those initially generated. Therefore, it is plausible that boundary probe 1 presents the highest normalized electric field values since it is located in the border between the air layer and the a-Si solar cell.

Boundary probes 2, 3 and 4 produce similarly shaped responses since they refer to the same material: amorphous silicon (a-Si). Quite distinct is the spectrum produced by boundary probe 1, this one, as previously mentioned, located between two different materials: air and amorphous silicon (a-Si).

At this point, the metallic nanoantenna array is coupled to the solar cell to analyse the behaviour of the nanostructure upon the integration of the nanoantenna and compare the results with those obtained for the nanostructure without the nanoantenna.

5.1.1. Introduction of Nanoantenna

The output optical response regarding the 2D model with nanoantenna is presented in figure 5.4, and it was obtained in the same way and under the same conditions as the output spectrum for the previously simulated model without the nanoantenna, in subchapter 5.1. Additionally, figure 5.5 shows the normalized electric field which helps to visualize how the electric field propagates along the structure and to identify the occurrence of field amplification as well as the regions of the nanostructure where the phenomenon occurred in a more significant manner.

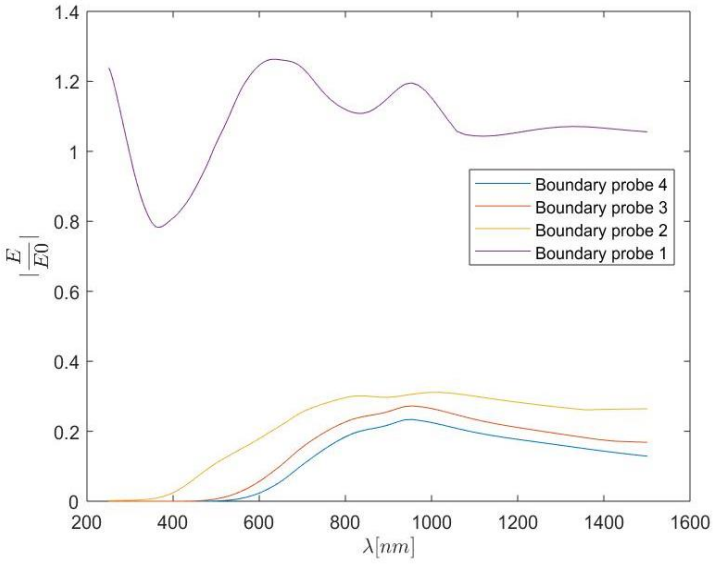

Figure 5. 4 – Optical response of the 2D a-Si solar cell structure with nanoantenna.

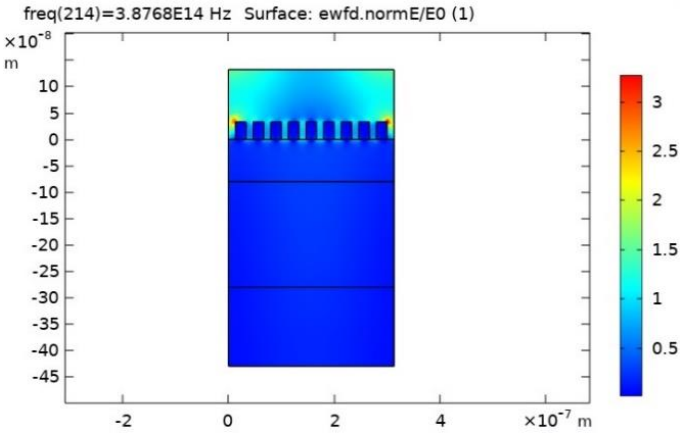

Figure 5. 5 - Electric field of the 2D a-Si solar cell structure with nanoantenna for an incident wavelength of 775 nm.

When analysing figure 5.4, it is possible to determine that the EOT phenomenon did in fact occur, since values greater than 1 were obtained for boundary probe 1. Naturally, this will be the boundary that presents the best results since it is located directly underneath the nanoantenna array, which is where surface plasmon polaritons are going to be generated and propagate, specially at the dielectric-metal interface as illustrated in figure 5.5. Even though, according to the results produced by boundary probe 1, the EOT phenomenon occurred, this occurrence did not influence the results of the remaining boundary probes. In fact, the values obtained by these probes are quite similar to those obtained by the model without the nanoantenna, as it will be confirmed later, during the analysis of figure 5.8.

However, it is important to stress that the results obtained for the boundary probes located within the a-Si solar cell represent the electric field that was not absorbed by the cell being that, at the cell's output, this value should be as low as possible. It is crucial to establish that, the greater the difference between the input electric field in the cell or in a certain layer and its output electric field, the greater the absorption. Thus, one can presume that the greater the gap between

the normalized electric field values from one probe to the next, the greater the absorption that occurred in that specific layer of the cell, bounded by those probes. Plus, evidently, the more photons are absorbed by the cell, the more electric power can be generated, due to the photoelectric effect.

Figure 5.6 illustrates the squared normalized electric field values along the incident wavelength spectrum, regarding the produced radiation intensity or irradiance. The time-averaged magnitude of the Poynting vector, $< S >$, relates to the squared value of the complex amplitude of the electric field. Therefore, when discussing abortion in the solar cell one should perhaps consider the produced intensity values. However, as figure 5.6 portrays, the results and subsequent analysis of the squared normalized electric field values, $\left|\frac{\mathrm{E}}{\mathrm{E_0}}\right|^2$, do not differ in a significant manner from those represented in figure 5.4, regarding the normalized electric field values, $\left|\frac{\mathrm{E}}{\mathrm{E_0}}\right|$. Thus, the following simulations will continue to depict the models optical responses by illustrating that exact ratio, $\left|\frac{\mathrm{E}}{\mathrm{E_0}}\right|$, since the analyses resulting from both ratios are analogous.

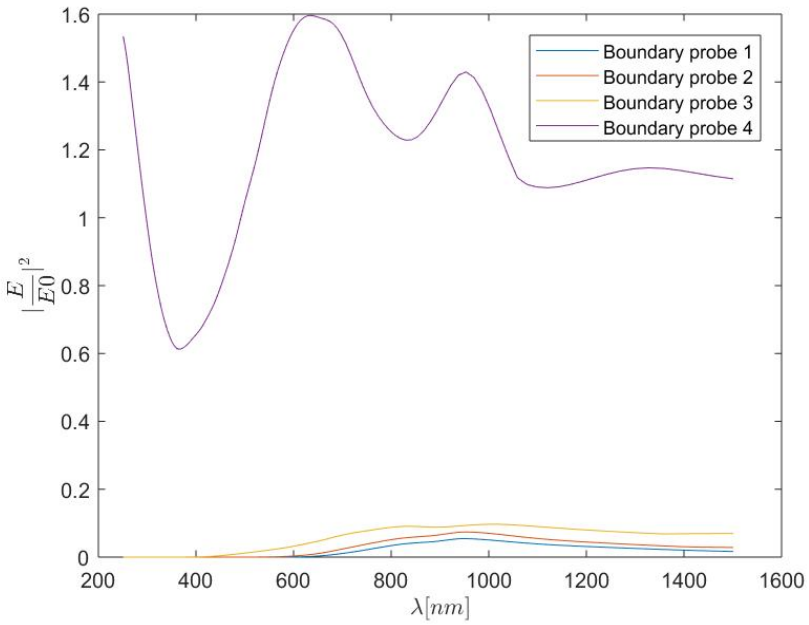

Figure 5. 6 - Optical response of the 2D a-Si solar cell structure with nanoantenna: produced radiation intensity.

Based on the aforementioned premise that the greater the gap between the normalized electric field values from one probe to the next, the greater the absorption that occurred in the layer bounded by those probes, figure 5.7 illustrates the absorption occurring in each layer of the cell. For each layer of the cell, the difference between the intensity values of the output probe and the input probe is computed. Thus, for layers where absorption occurs, these values will be negative. Therefore, according to figure 5.7, photons are going to be absorbed essentially in the first layer of the cell (Layer 1), particularly for the incident wavelength regions where field amplification is verified in figure 5.4, such as 600 nm and 1000 nm.

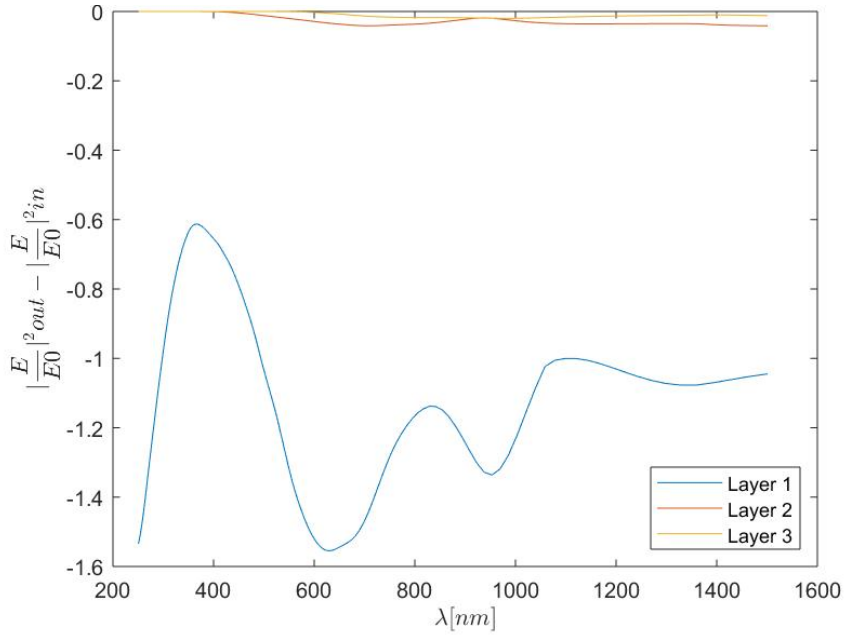

Figure 5. 7 - Absorption curves of the simulated 2D a-Si solar cell structure with nanoantenna.

The following graphics, represented in figure 5.8, allow the comparison between the results obtained for the simulated 2D structure, with and without the nanoantenna, to be made in a more precise way. Each figure shows the optical response obtained for both 2D models regarding a specific boundary probe.

Figure 5.8a, regarding boundary probe 1, illustrates a considerable difference between the electric field results obtained for the model with and without the nanoantenna. The occurrence of EOT is clear in the model coupled with the nanoantenna and can be identified almost throughout the entire wavelength range. In figure 5.8b, regarding boundary probe 2, the model with nanoantenna produces slightly better results for certain incident wavelengths where field amplification can be confirmed. However, overall, for boundary probes 2, 3 and 4 the optical response of both models was essentially the same, with or without the nanoantenna's presence. In order for the results of those probes, that regard the second and third layer of the a-Si cell, to be almost unaltered, the majority of the absorption had to have occurred in the cell's first layer, where boundary probe 1 is located. This is corroborated by the results already presented in figure 5.7.

Taking into account the fact that, due to field amplification, the introduction of the nanoantenna implies that more electrons are available in the cell's first layer and that the majority of the absorption takes place in this exact layer, then more electrons are going to be absorbed, resulting in greater generation of electric current. Overall, the 2D results show that the implementation of the nanoantenna in the structure was valuable, leading to field amplification and increased absorption of photons, particularly in the cell's first layer.

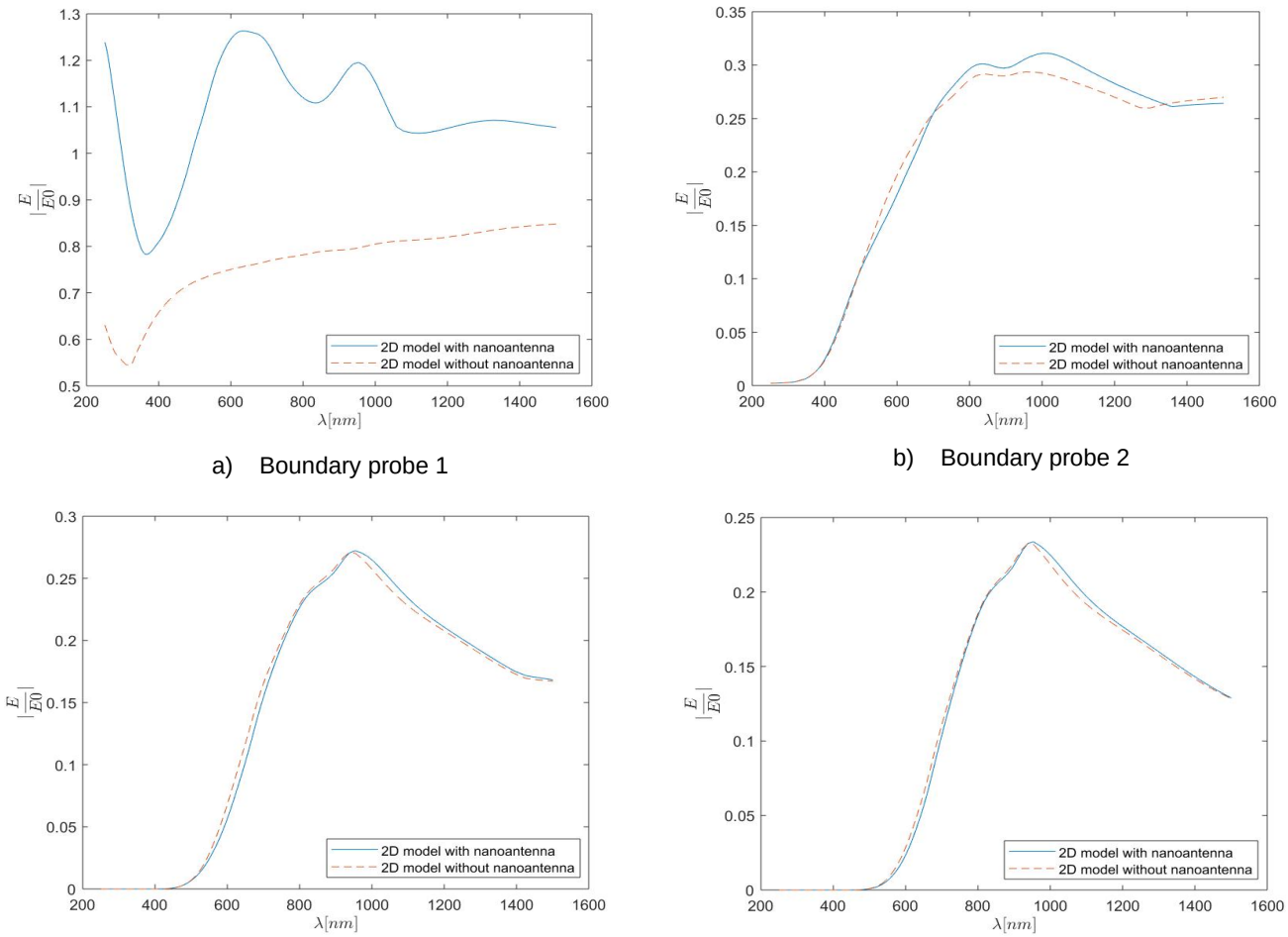

a) Boundary probe 1

b) Boundary probe 2

c) Boundary probe 3

d) Boundary probe 4

Figure 5. 8 - Optical response of the 2D a-Si solar structure with and without nanoantenna.

However, although the findings of the 2D simulations are legitimate, the 2D model and, consequently, the results produced by it, do not represent reality in an accurate manner. The 2D model disregards the edge effect over the electric field, which simplifies the problem in question, but at the same time makes the model less realistic and reliable. Therefore, it is important to study the integration of nanoantennas in solar cells in a 3D setting, an environment that is closest to actual reality. The 3D model allows the nanoantenna's periodicity to be depicted in two directions (x and y directions) which will guarantee that the generation of SPP's is portrayed in a truthful manner, since it is actually influenced by the electric field component parallel to the nanoantenna, that has x direction and y direction components.

5.2. 3D Simulations

The procedures and conditions applied to carry out the simulation of the 3D models with and without the nanoantenna are identical to those described in subchapter 5.1.

Therefore, the maximum absolute values of the normalized electric field, $\left|\frac{E}{E_0}\right|$, are computed and analysed. Alike to what was defined for the 2D models, the boundary probes are located at the end of each layer of the nanostructure. Moreover, the simulations are also developed for a range of $[250\ \ 1500]$ nm, with 250 equidistant wavelength points.

5.2.1. Amorphous Silicon (a-Si) Solar Cell Structure

The simulation results in figure 5.9 regarding the amorphous silicon solar cell model without the nanoantenna (figure 4.8), show that EOT does not occur.

Similarly to what was already observed in the 2D simulations, without the presence of a subwavelength nanostructure like the nanoantenna array, the conditions for the occurrence of extraordinary transmission are not met hence the EOT phenomenon does not take place. Instead, due to losses endured throughout the air layer and the absorption endured throughout the a-Si cell, the electric field will simply decay along the structure as illustrated in figure 5.10.

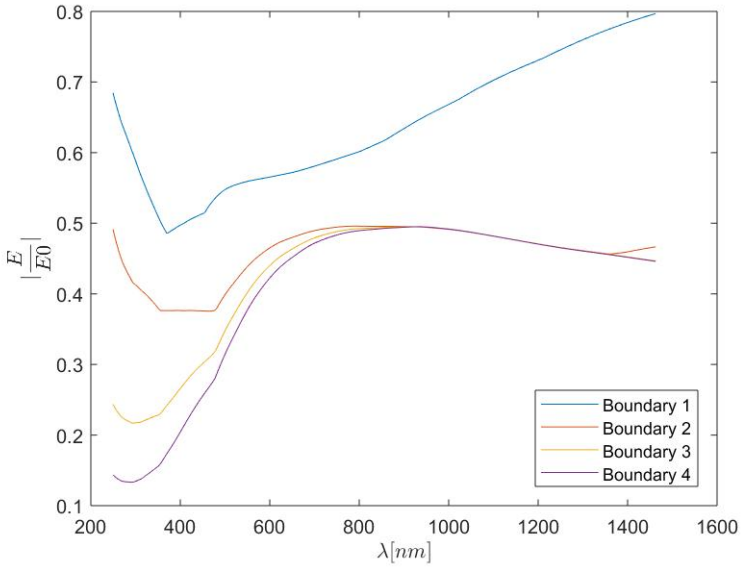

Figure 5. 9 - Optical response of the 3D a-Si solar cell structure.

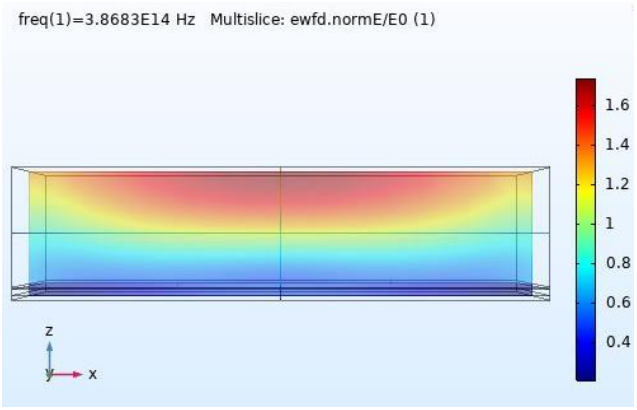

Figure 5. 10- Electric field of the 3D a-Si solar cell structure for an incident wavelength of 775 nm.

The impact that the introduction of the nanoantenna has in the optical response of the a-Si cell 3D model is assessed and discussed in the following subchapter.

5.2.1.1. Amorphous Silicon (a-Si) Solar Cell Structure: Introduction of Nanoantenna

The simulation results in figure 5.11, regarding the a-Si solar cell 3D model with nanoantenna (figure 4.9), clearly show the presence of EOT, though only for boundary probe 1 located underneath the nanoantenna array, at the beginning of the solar cell. This is possibly due to the reduced propagation distance of the SPP's (around nm). Boundary probe 1 also shows two identifiable peaks in the normalized electric field values, which were not present in the optical response of the model without the nanoantenna. These peaks are obtained for the incident wavelengths of 700 nm and 1000 nm, located in the visible and near-infrared regions, respectively. However, the extraordinary transmission verified in boundary probe 1 did not affect the remaining boundary probes, as the obtained electric field ratio values are quite small, never reaching unitary values.

The dispersion of the generated SPP's is associated with a propagation distance along two different directions: parallel to the nanoantenna (x and y direction) and parallel to the electric field propagation (z direction). The electric field penetration depth along the z axis depends on the dielectric function of the dielectric material (air) and of the nanoantenna's material (Al). Nonetheless, the dielectric function of the substrate in question, which in this case is an amorphous silicon solar cell, can also influence that propagation distance. The real part of the dielectric function of a-Si shows quite high values, imposing significant losses that can result in shorter propagation distances along the z direction for the generated SPP's.

A 3D plot of the normalized electric field is illustrated in figure 5.12 and shows the generation and propagation of the surface plasmon polaritons throughout the nanostructure. It is possible to verify that on the area surrounding the nanoantenna holes, specially at the dielectric-metal interface, the field amplification is greater than in the rest of the structure. In the remaining parts of the structure the field amplification, though present in some points, is not as substantial. These results corroborate what is suggested by the simulation in figure 5.13 regarding the four different boundary probes, that consider different sections of the nanostructure.

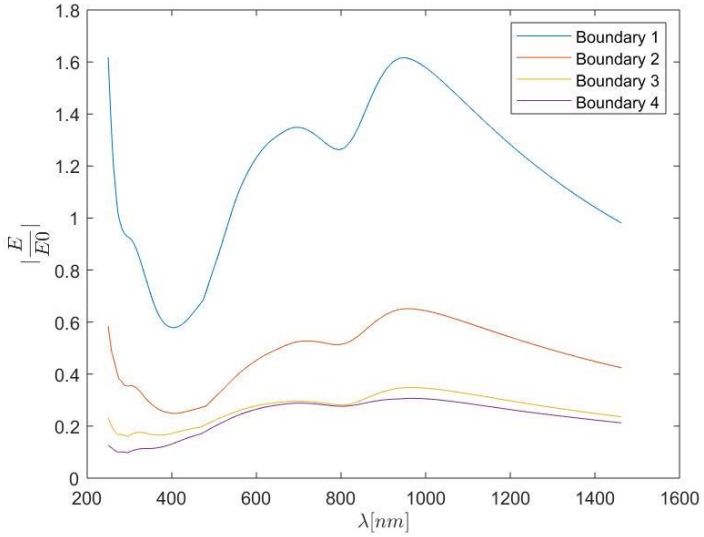

Figure 5. 11 - Optical response of the 3D a-Si solar cell structure with nanoantenna.

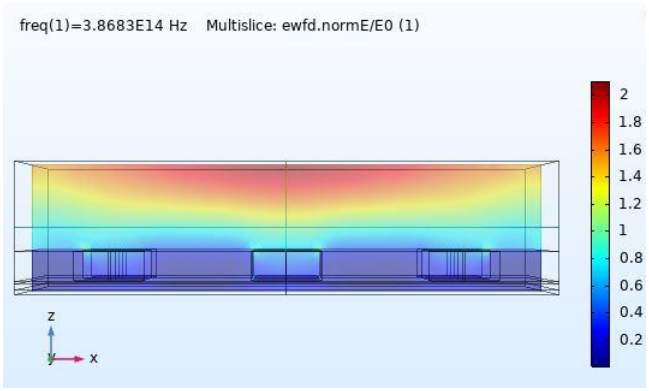

Figure 5. 12 - Electric field of the 3D a-Si solar cell structure with nanoantenna for an incident wavelength of 775 nm.

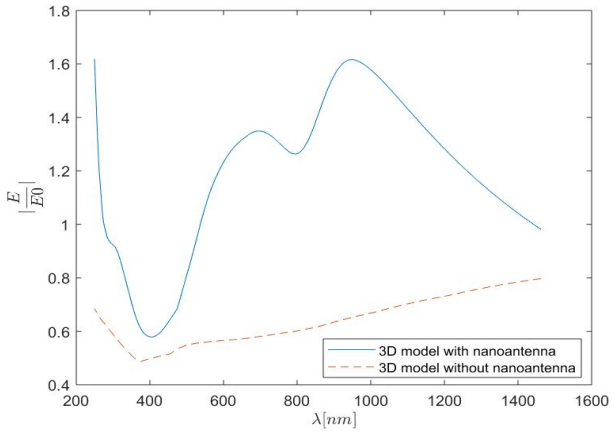

a) Boundary probe 1

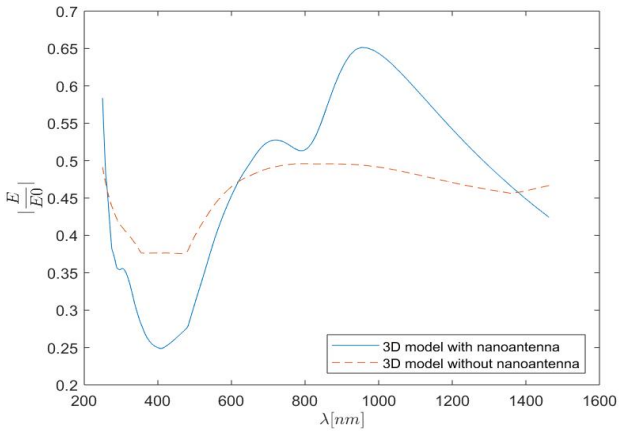

b) Boundary probe 2

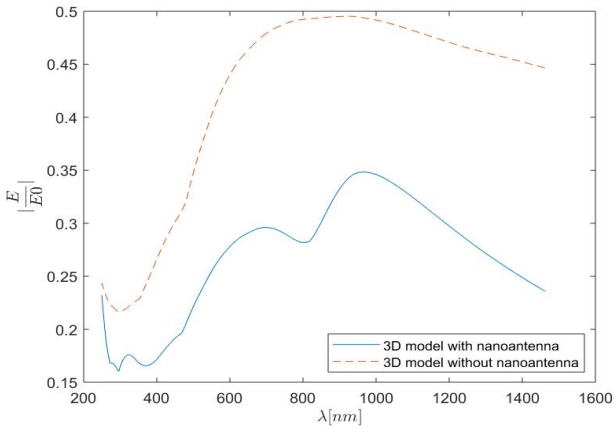

c) Boundary probe 3

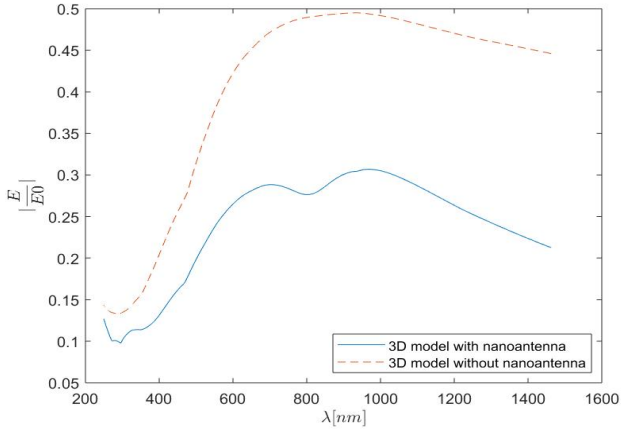

d) Boundary probe 4

Figure 5. 13 - Optical response of the 3D a-Si solar cell structure with and without nanoantenna.

Figure 5.13a, regarding boundary probe 1, can clearly demonstrate the substantial difference in the electric field values when using a model with or without the implementation of a nanoantenna. EOT is present throughout almost the entire incident wavelength range meaning that the conditions required for the generation of surface plasmon polaritons, previously mentioned in subchapter 3.3.2, are met for different regions of the incident light spectrum such as the visible and the infrared region. On the other hand, figure 5.13b shows that, although EOT is not verified in boundary probe 2, field amplification still exists as can be seen for the incident wavelength interval between 600 nm and 1400 nm. As for figures 5.13c and 5.13d, these demonstrate that the in the model with nanoantenna the electric field absorption all through the cell is greater since the normalized electric field values obtained for boundary probes 3 and 4 are much smaller than those obtained by the model without nanoantenna. This conclusion is supported by figures 5.14 and 5.15, where absorption curves for both scenarios (with and without nanoantenna) are illustrated. By analysing those figures, it becomes clear that for the model with the nanoantenna the absorption of photons is greater. The increase in absorption is visible in all layers of the cell but specially accentuated in the first layer of the cell (layer 1), where EOT occurs. Moreover, peaks in absorption correspond to peaks in field amplification observed in figure 5.11, for incident wavelengths of 700 nm and 1000 nm. Once again, it is important to stress that greater absorption ultimately results in greater amount of electric power supplied by the cell.

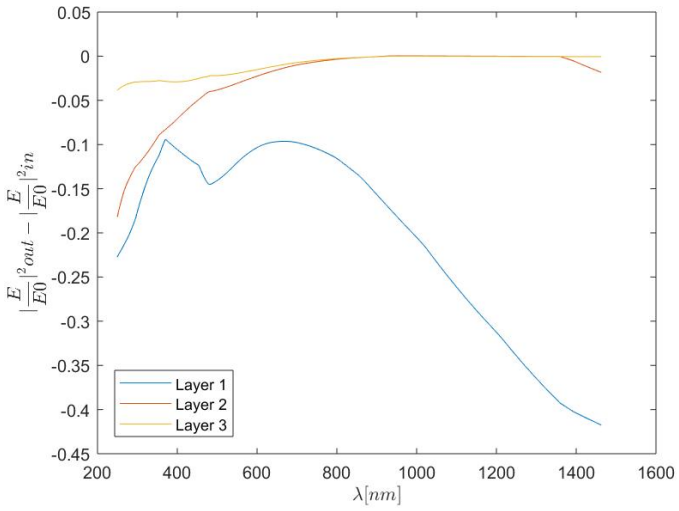

Figure 5. 14 - Absorption curves for the 3D a-Si solar cell structure without nanoantenna.

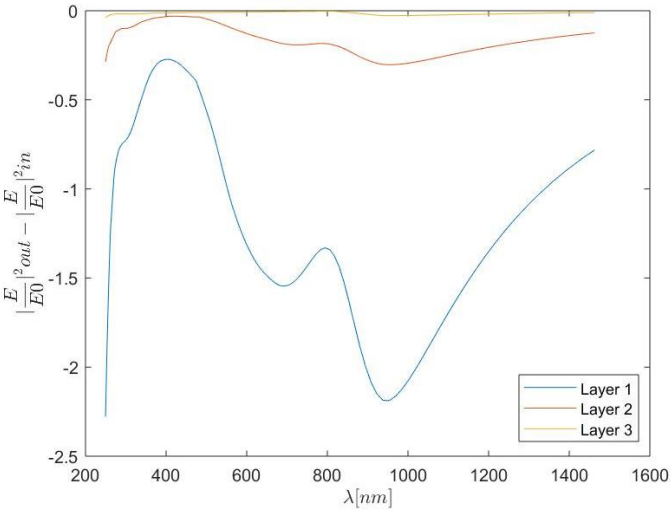

Figure 5. 15 - Absorption curves for the 3D a-Si solar cell structure with nanoantenna.

The results obtained in the simulations of the 3D model (with and without the nanoantenna) can, overall, corroborate the findings acquired by the previously established 2D simulations. Although the 2D and 3D simulation results differ, both lead to the conclusion that the integration of the nanoantenna in the structure results in better capture and absorption of electromagnetic radiation by the a-Si cell.

5.2.1.2. Amorphous Silicon (a-Si) Solar Cell Structure: Introduction of Nanoantenna Within the Solar Cell

The variation of certain parameters like periodicity, thickness, number of holes and diameter of holes, can certainly affect the output optical response of a structure containing a nanoantenna. The 3D model described in subchapter 4.3 was developed based on an optimized version of an aluminium nanoantenna structure presented in [65], where the authors explore the influence that such structure parameters can have on nanoantennas' optical response. However, the nanoantenna position in the nanostructure may also be an important factor when it comes to the optical response produced by the model. Hence, a study regarding the introduction of the nanoantenna within the solar cell, between the a-Si layers, is carried out.

For the nanoantenna to be positioned between the layers of the solar cell, the cell's dimensions had to be modified. Since the nanoantenna array has a thickness of 50 nm and the original amorphous silicon solar cell has a thickness of 21.5 nm, in order to place the nanoantenna layer within the solar cell, its thickness was increased to 150 nm with each layer having an equal thickness value of 50 nm. The resulting model is illustrated in figure 5.16.

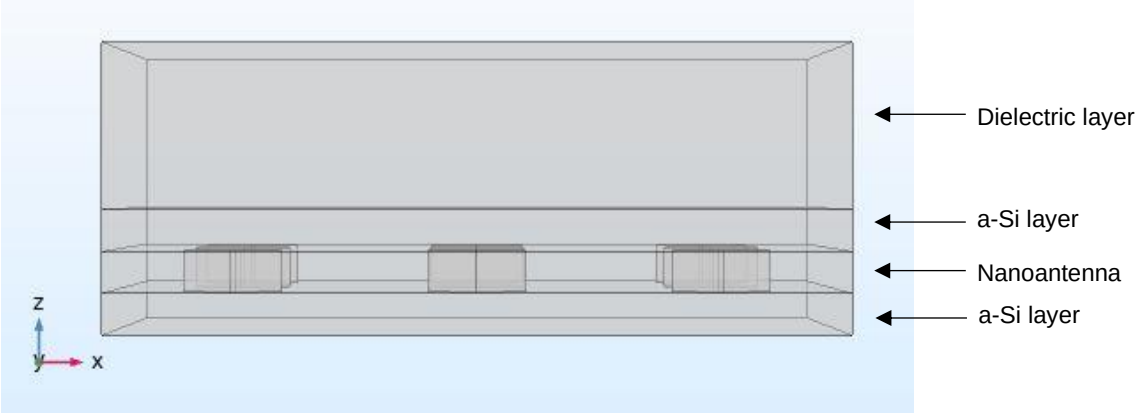

Figure 5. 16 - Side view of the 3D a-Si solar cell structure with nanoantenna within the solar cell.

The output optical response of this model, illustrated in figure 5.17, shows a significantly different spectrum than the one obtained for the original 3D model, simulated in 5.2.1.1, implying that the position of the nanoantenna in the structure can have a substantial influence in the produced results. However, it is worth noting that, since the cells in those models have different dimensions, their optical responses cannot be directly compared.

Figure 5.18 shows the electric field distribution for an incident wavelength of 775 nm, for this particular model.

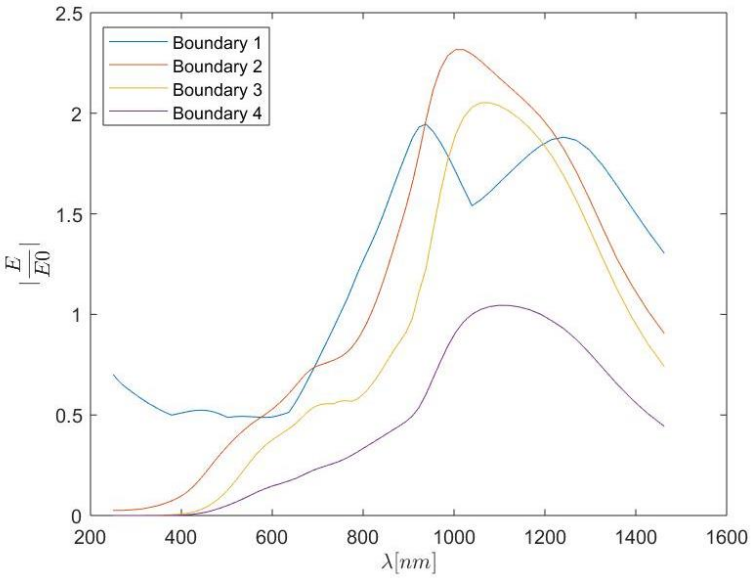

Figure 5. 17 – Optical response of 3D a-Si solar cell structure with nanoantenna within the solar cell.

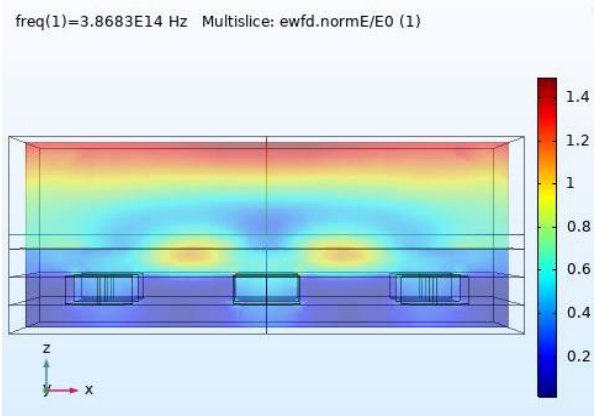

Figure 5. 18 - Electric field of the 3D a-Si solar cell structure with nanoantenna within the solar cell for an incident wavelength of 775 nm.

According to figure 5.17, extraordinary transmission can be identified for boundary probes 1, 2 and 3. Although the nanoantenna is located between probes 2 and 3, probe 1 is also influenced by the EOT phenomenon that occurs in the nanoantenna. By inserting the nanoantenna inside the solar cell, extraordinary transmission can occur within the cell and influence the electric field values, mainly in the cell's second layer. Nevertheless, the presence of EOT or any field amplification is confined to the infrared region, as demonstrated by the distinguishable peaks produced by all boundaries in that exact region of the wavelength spectrum.

Due to the location of the nanoantenna, the incident light reaches the device having already propagated trough one layer of a-Si (the first layer of the cell), meaning that absorption of photons with energy levels equal or higher than the energy gap level (for wavelengths equal or lower) of a-Si which is 1.6 eV corresponding to 775 nm, has already occurred. This ultimately implies that the radiation influenced by the nanoantenna will be mainly located in incident wavelengths after the 775 nm mark, regarding the infrared region. Figure 5.19 corroborates this reason, since absorption is verified within the first layer of the cell (layer 1) until the 600 nm mark, followed by a substantial increase in absorption for the second and last layers of the cell (layer 2 and layer 3) already in the infrared region of the spectrum which is also the region that presented greater field amplification.

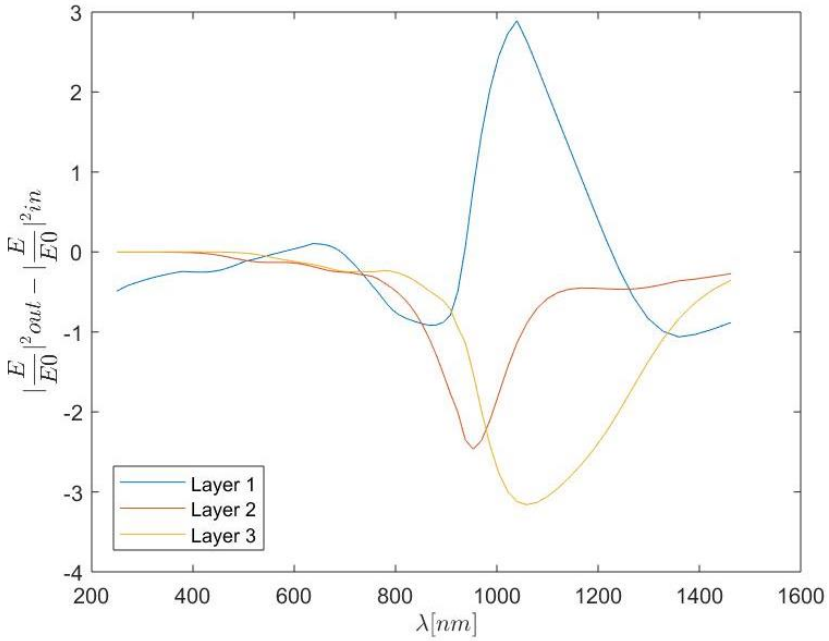

Figure 5. 19 - Absorption curves of the 3D a-Si solar cell structure with nanoantenna within the solar cell.

Figure 5.20 shows the comparison between the obtained results for this particular model with and without the nanoantenna. It confirms that a considerable increase in electric field values does take place upon the coupling of the nanoantenna to the solar cell, which can be observed in the responses produced by all defined boundary probes.

Ultimately, it can be concluded that the main effect that this type of structure configuration has is the displacement of the electric field amplification peak from the visible region, where it is typically located, to the infrared region. This specific characteristic can be extremely valuable for certain devices that must work in the infrared region of the light spectrum. Considering that silicon is a relatively common material and easy to acquire, for applications in the IR region, it may be advantageous to use this type of structure instead of investing in new designs or materials for new devices.

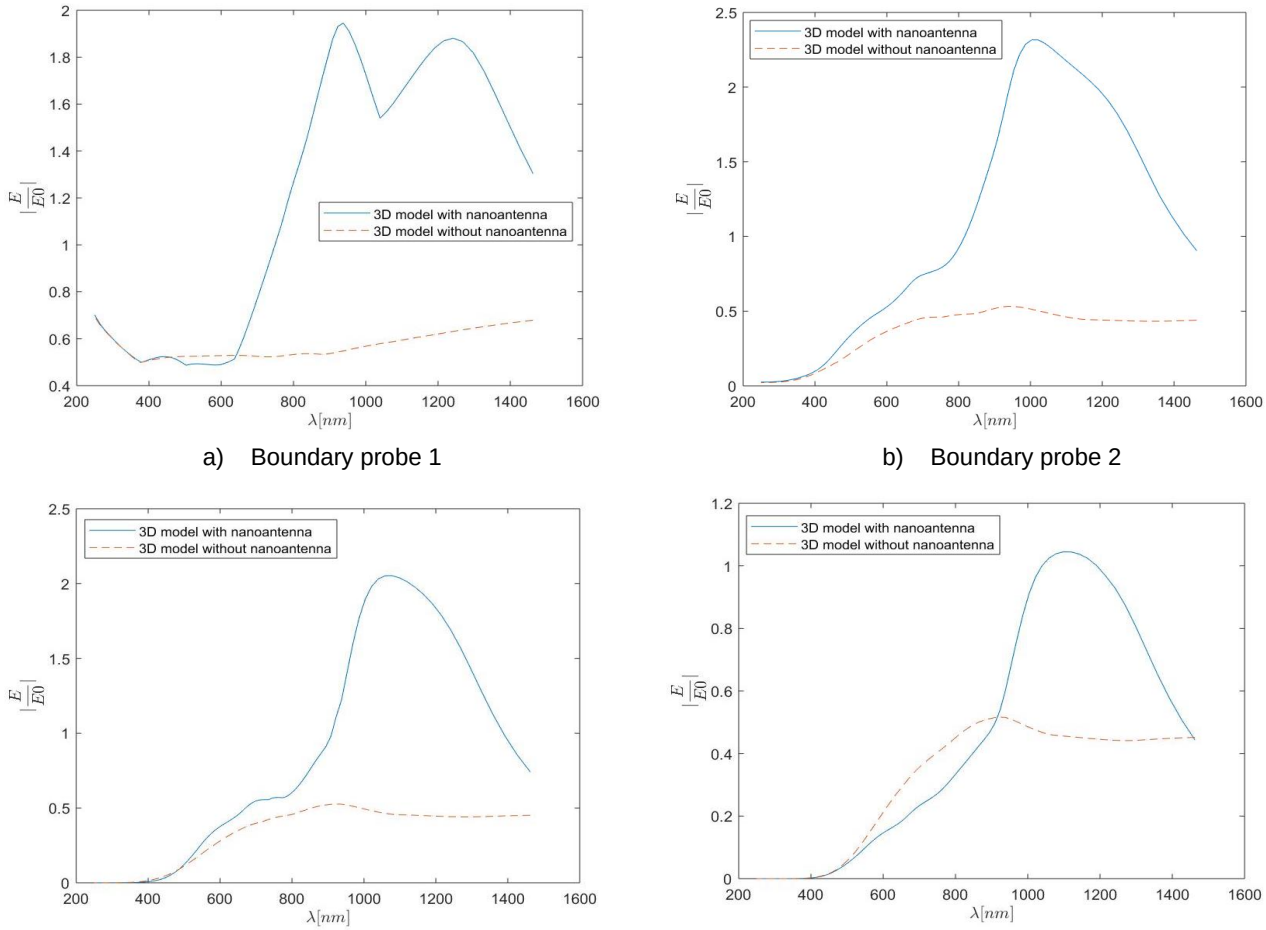

a) Boundary probe 1

b) Boundary probe 2

c) Boundary probe 3

d) Boundary probe 4

Figure 5. 20 - Optical response of the 3D a-Si solar cell structure with and without nanoantenna (for a a-Si cell of 150nm).

5.2.1.3. Amorphous Silicon (a-Si) Solar Cell Structure: Introduction of Nanoantenna with Conical Holes

The geometry of the holes in the nanoantenna is also an important element to take in consideration since it can have an impact in the output optical response of the model. Therefore, to study the influence of this factor, another type of geometrical shape was chosen for the holes in the nanoantenna: the cone. The conical geometry of the nanoantenna holes could perhaps result in improved concentration of incident radiation which could lead to greater field amplification.

Conical holes were then implemented in the nanoantenna layer of the original structure. The top circle of the cone maintained the same dimension as the cylindrical holes previously defined in subchapter 4.3.1, and for the bottom circle of the cone that value was halved. The resulting 3D structure is illustrated in figure 5.21.

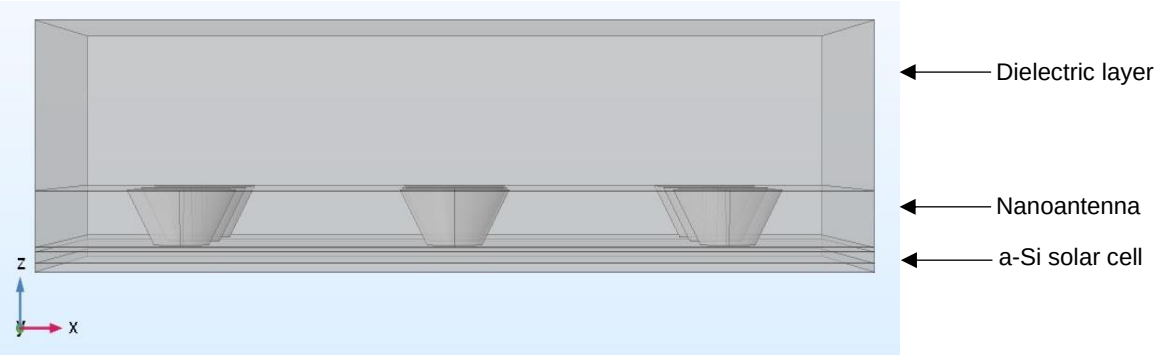

Figure 5. 21 - Side view of the 3D a-Si solar cell structure with nanoantenna with conical holes.

The optical response of the model, illustrated in 5.22, shows the presence of EOT in the results obtained for boundary probe 1, for the incident wavelength region around 600 nm and 1000 nm, which appear as clear peaks of electric field amplification. These wavelengths still represent peak values for the remaining boundary probes however, extraordinary optical transmission does not occur. As seen in previous simulations, the electric field clearly decays as it propagates throughout the nanostructure, leading to the decreasing electric field values observed for the different boundaries. This is also corroborated by the normalized electric field distribution, represented in figure 5.23.

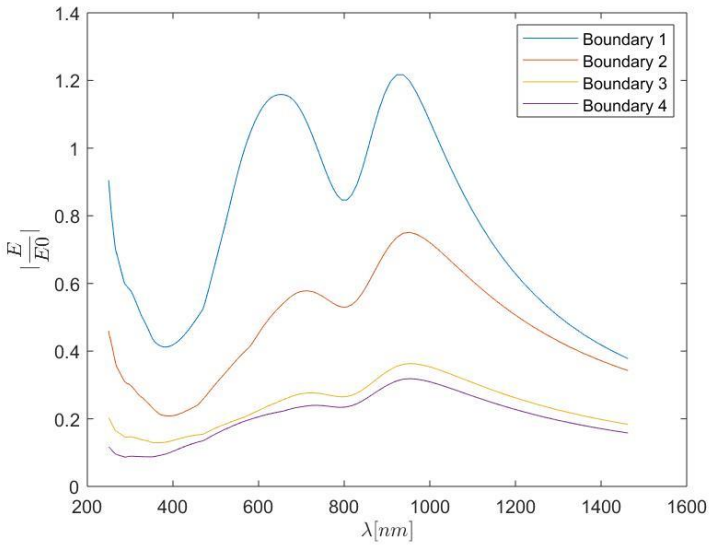

Figure 5. 22 – Optical response of the 3D a-Si solar cell structure with nanoantenna with conical holes.

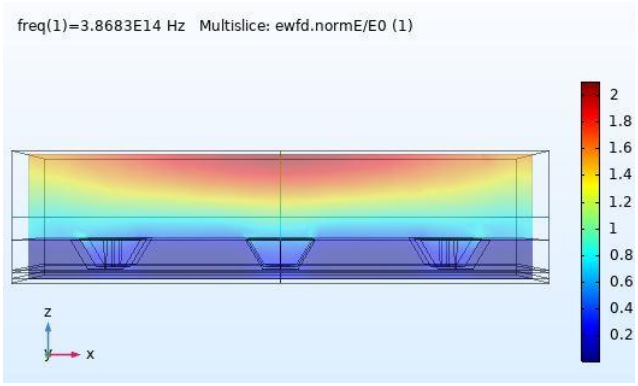

Figure 5. 23 – Electric field of the 3D a-Si solar cell structure with nanoantenna with conical holes for an incident wavelength of 775 nm.

Figure 5.24 makes the comparison between the optical response of the a-Si solar cell structure with the nanoantenna with cylindrical holes and with conical holes.

Since the geometry of the nanoantenna holes may eventually influence the occurrence of EOT, the results in boundary probe 1 are particularly relevant since this boundary is located directly underneath the nanoantenna, where EOT takes place. However, according to figure 24a, the use of conical holes, instead of cylindrical holes, does not result in greater extraordinary transmission since, for the model with cylindrical holes, results clearly show greater field amplification in boundary probe 1. Regarding the remaining boundary probes, the output optical spectra produced by both models, although not equal, show no significant differences.

Therefore, it can be concluded that this type of hole geometry is perhaps not the most appropriate to use in nanoantennas coupled to solar cells. In order to concentrate the incident radiation and amplify the electric field, a nanoantenna with cylindrical holes seems to be a better option.

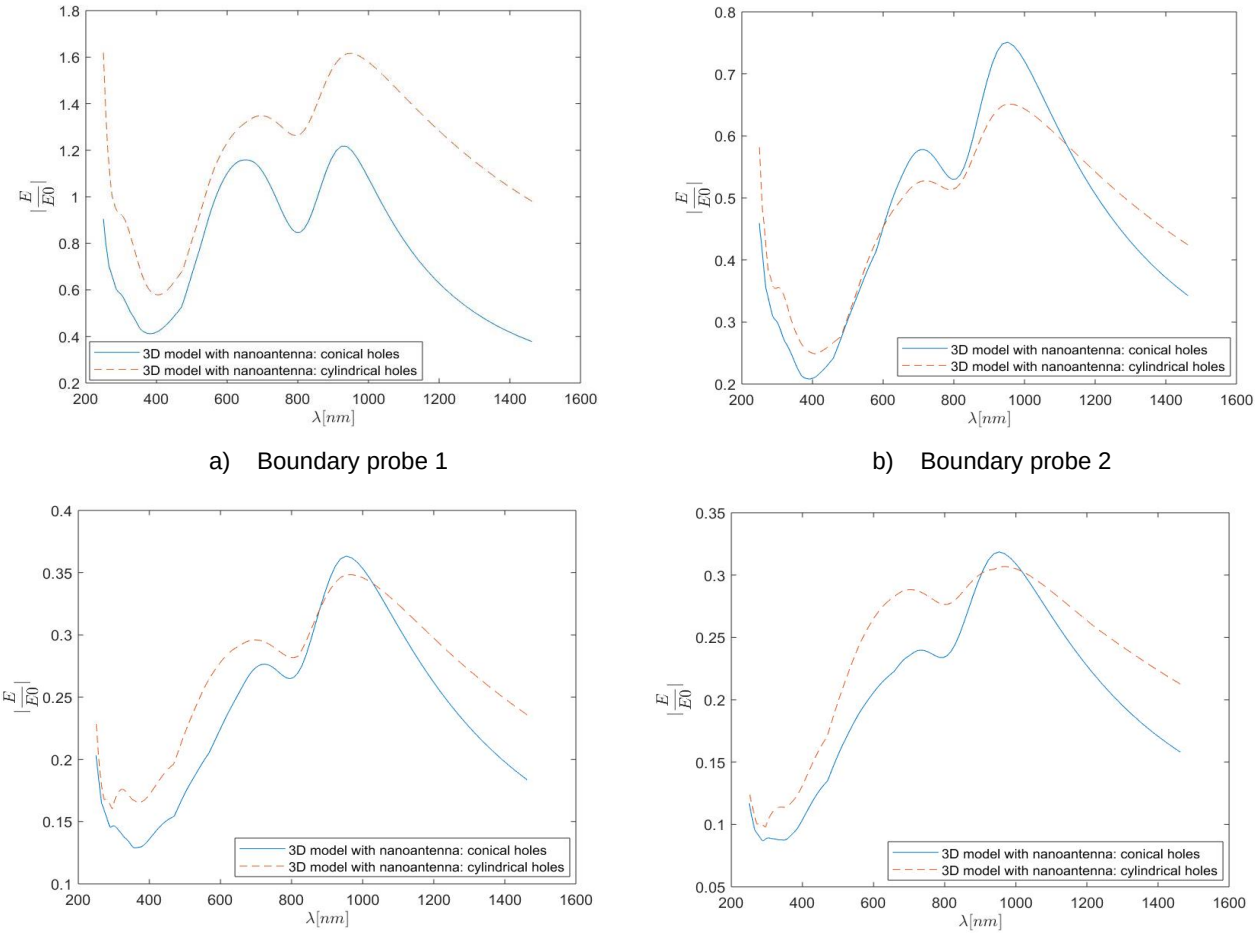

a) Boundary probe 1

b) Boundary probe 2

c) Boundary probe 3

d) Boundary probe 4

Figure 5. 24 - Optical response of the 3D a-Si solar cell structure with nanoantenna with conical holes versus nanoantenna with cylindrical holes.

5.2.2. Amorphous Silicon (a-Si) PIN Solar Cell Structure

The 3D a-Si PIN solar cell structure, characterized in 4.3.2, is simulated under the exact same conditions as prior simulations, already depicted throughout this chapter.

The comparison between the output optical response of the a-Si PIN solar cell structure without nanoantenna, and the output optical response of the a-Si solar cell structure also without nanoantenna is illustrated in figure 5.25. It is possible to verify that the generated spectra of both models are extremely similar, since these overlap along the entire incident wavelength range, with the exception of the minor divergence that occurs at the end of that range, around 1400 nm.

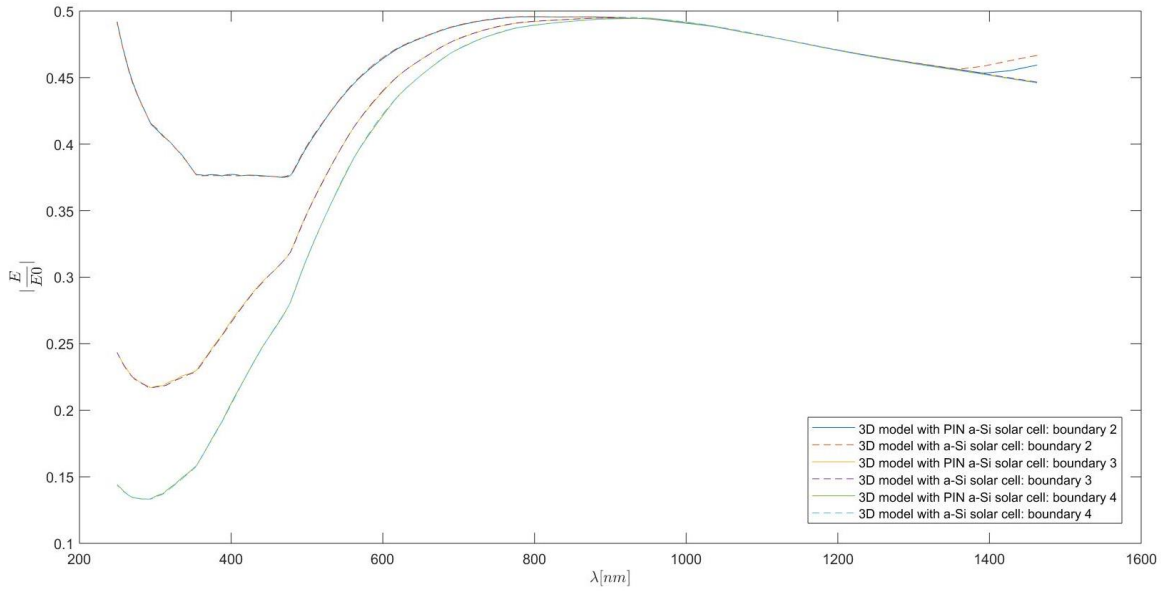

Figure 5. 25 - Optical response of the 3D a-Si PIN solar cell structure vs the 3D a-Si solar cell structure.

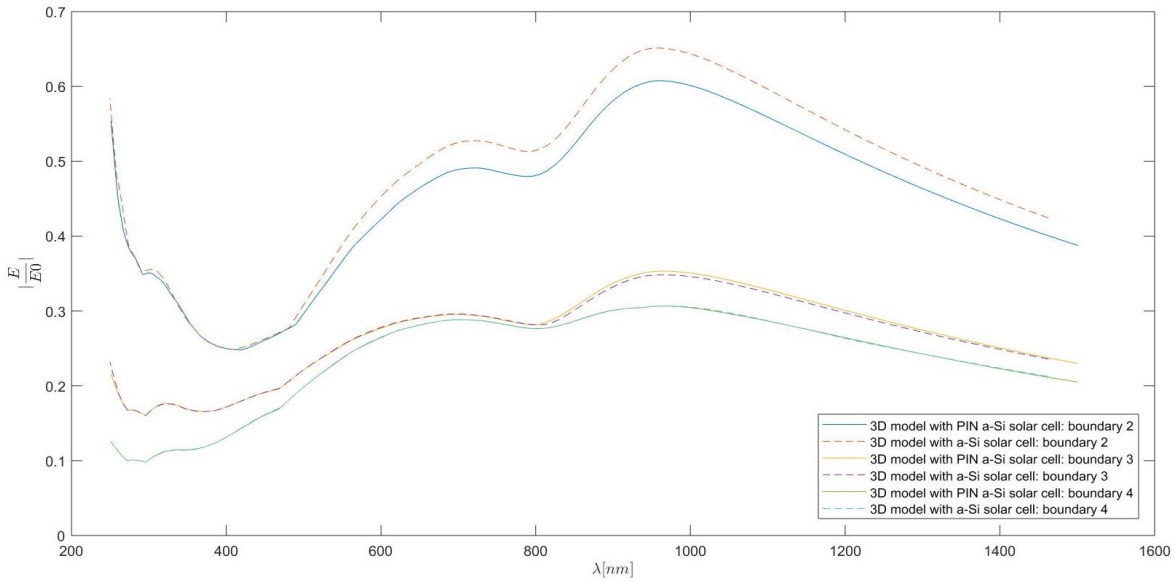

Figure 5. 26 - Optical response of the 3D a-Si PIN solar cell structure with nanoantenna vs the 3D a-Si solar cell structure with nanoantenna.

A similar situation can be observed in figure 5.26, illustrating the comparison between the output optical response of the a-Si PIN solar cell structure and the output optical response of the a-Si solar cell structure, both with nanoantenna. Although in this case the results obtained by boundary probes 2 and 3 slightly vary between the two models, this difference can be considered negligible.

It should be noted that the results produced by boundary probe 1 were not included in the simulation results, as seen in both figures 5.25 and 5.26. Taking into account the fact that the first boundary probe is located between the air layer and the solar cell, it is possible to remove it from the simulations in order to simplify and ease the procedure in question, without affecting the analysis of the absorption taking place within the cell.

Overall, the results obtained by the simulations using both models, with and without nanoantenna, are quite similar. Therefore, although the optical responses of the two models are not exactly equal, they corroborate the idea that the majority of light absorption occurs in the intrinsic layer of a solar cell, validating the decision to consider the structure composed of intrinsic a-Si as an actual a-Si PIN solar cell in order to simplify the performed simulations.

5.2.3. CIGS Solar Cell Structure

The procedures necessary to simulate the CIGS solar cell structure, characterized in 4.3.3, are identical to those defined in all previous simulations. Nevertheless, the simulations performed regarding this particular model measure the maximum absolute values of the normalized electric field over five, instead of four, different boundary probes located at the end of each layer of the structure. This is obviously due to the fact that the CIGS cell defined in this structure has one more layer than the a-Si solar cell used in the other models. Figure 5.27 illustrates the output optical response of the CIGS solar cell 3D structure without nanoantenna and, additionally, figure 5.28 shows the normalized electric field for that particular model, for an incident wavelength of 775 nm. On the other hand, the output optical response of the model with the integration of the nanoantenna is represented in figure 5.29. Furthermore, figure 5.30 illustrates the normalized electric field distribution for the situation with the nanoantenna.

By examining figure 5.27, it is possible to observe that, for the first three boundary probes, the normalized electric field reaches values equal to 1 or higher even without the presence of a nanoantenna, especially in the infrared region of the spectrum. This gain is typically associated to the material of the structure in question, which in this case corresponds to the materials present in the first two layers of the CIGS solar cell: ZnO and Cds. If the dielectric function of a certain material has an imaginary part greater than zero then it would be possible to find electric field amplification within that material, possibly obtaining values bigger than 1 for the normalized electric field, even without the presence of any type of subwavelength aperture. However, it is important to note that almost no absorption occurs throughout these first layers of the cell, as verified in figure 5.31. Absorption of photons does occur in the layer between boundary probe 3 and boundary probe 4, where the difference in the normalized electric field values is quite

accentuated, mainly in the infrared region. This specific layer corresponds to the cell's third layer (layer 3), the CIGS layer, and results in figure 5.31 confirm that this is the only layer where absorption occurs in a significant manner. The absorption is focused on the infrared region since CIGS cells typically absorb radiation consistent with that exact region of the spectrum, as their energy band gap can be tuned roughly from 1.01eV to 1.68eV corresponding approximately to 1230 nm and 740 nm, respectively.

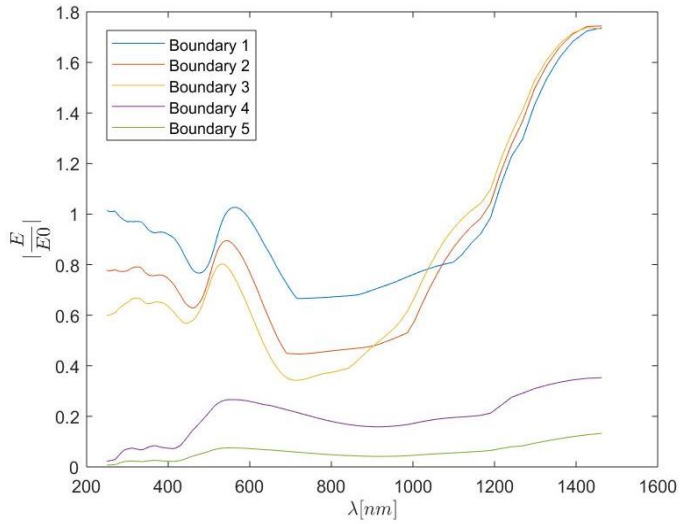

Figure 5. 27 - Optical response of the 3D CIGS solar cell structure.

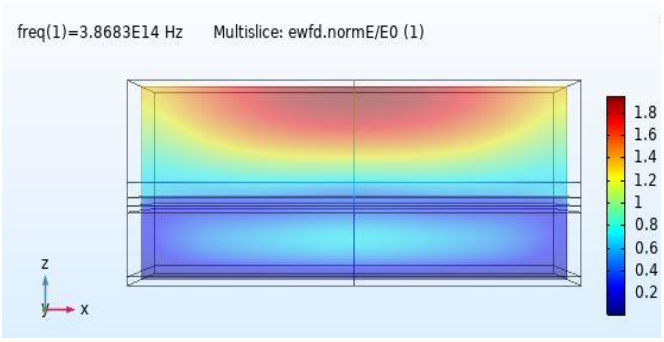

Figure 5. 28 - Electric field of the 3D CIGS solar cell structure for an incident wavelength of 775 nm.

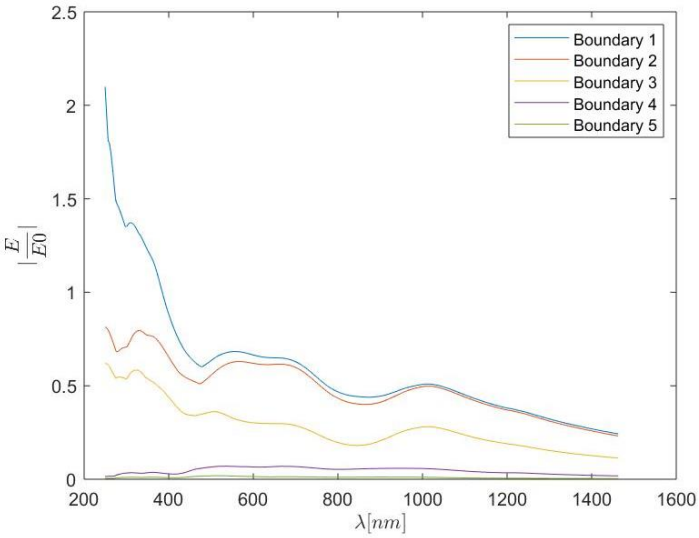

Figure 5. 29 - Optical response of the 3D CIGS solar cell structure with nanoantenna.

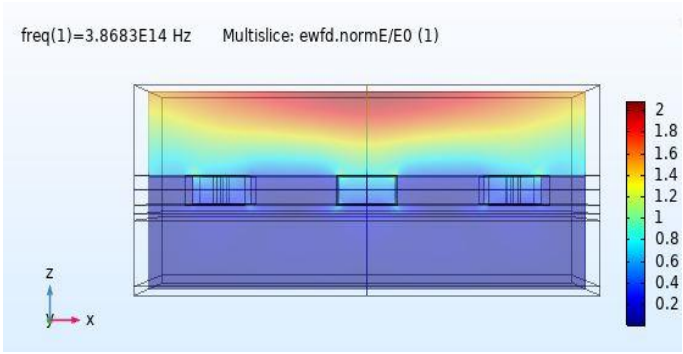

Figure 5. 30 - Electric field of the 3D CIGS solar cell structure with nanoantenna for an incident wavelength of 775 nm.

When the implementation of the nanoantenna occurs on top of the CIGS solar cell, the obtained optical response, represented in figure 5.29, is quite underwhelming when it comes to the observation of the EOT phenomenon. The values obtained for the normalized electric field are quite low in the first boundary probes if compared to those obtained without the nanoantenna. However, in boundary probe 1, a peak in the normalized electric field can be observed around the 250 nm mark, in the UV zone of the light spectrum, and EOT is present until 400 nm. Also, although the simulation wavelength range starts at 250 nm, the results suggest that perhaps greater field amplification occurs for even smaller incident wavelengths, since the normalized electric field values seem to be decreasing along the wavelength spectrum.

According to figure 5.32, the absorption of photons in the CIGS layer (layer 3) is significantly inferior in this scenario when compared to the model without the nanoantenna. Nevertheless, absorption did increase in the second layer of the cell (Cds layer) and specially in the first layer of the cell (ZnO layer). Plus, throughout all layers, the majority of absorption now concerns photons in the UV region of light spectrum.

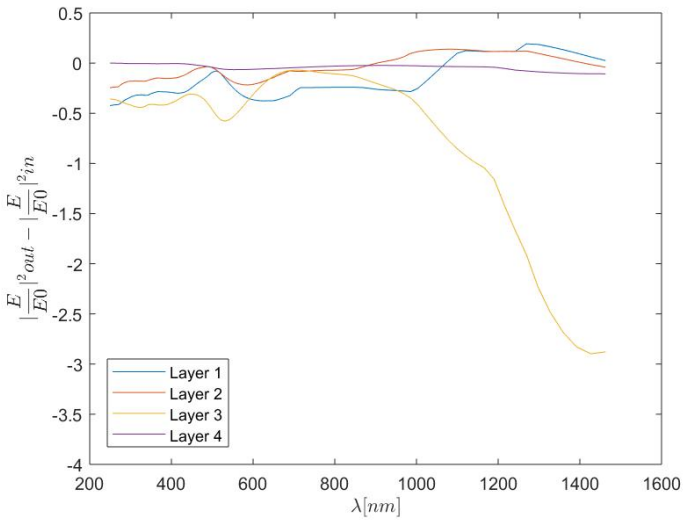

Figure 5. 31 - Absorption curves of the 3D CIGS solar cell structure without nanoantenna.

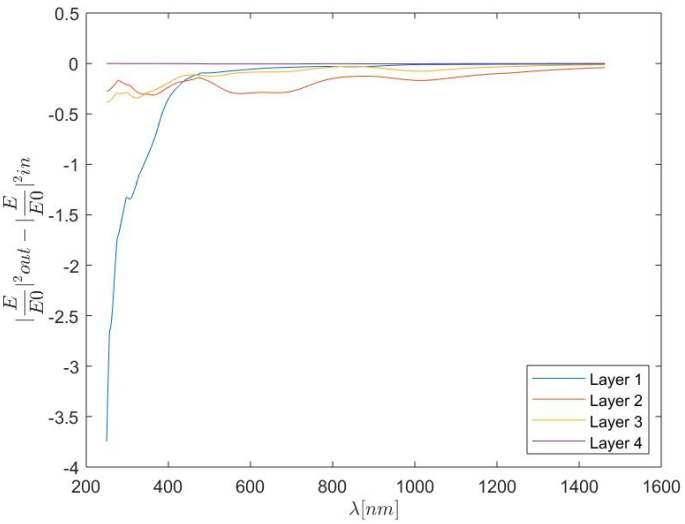

Figure 5. 32 - Absorption curves of the 3D CIGS solar cell structure with nanoantenna.

6. Conclusions

The main goal of this dissertation is to study the behaviour of a solar cell with the integration of an optical nanoantenna. The coupling of nanoantennas to solar cells could eventually constitute a breakthrough regarding solar harvesting on PV panels, due to the concentration and amplification of solar irradiance, resulting in more incident energy and, therefore, more generation of output power.

In an initial stage, it was important to understand the state of affairs at a global level regarding renewable energy. Focusing more on photovoltaics, different types of PV technologies were reviewed, and it became clear that the first and second generation of photovoltaic solar cells currently dominate the market. The life cycle of a standard PV solar cell was analysed, and some of the different approaches that are currently available to deal with the disposal of these devices in a sustainable manner were explored and discussed.

In chapter 2, extensive research on the subject of nanoantennas was completed, focusing mainly on solar harvesting purposes. The concept of an optical rectenna system illustrates how nanoantennas fit into the generation of electric power from the collection of solar energy. The ability to control and manipulate optical radiation at subwavelength scales associated to these devices can depend on technical specifications such as the type of rectifier system used in the structure or the design and material of the nanoantenna itself. The practical use of subwavelength apertures to enhance light-matter interaction in the context of PV technology has shown promising results. More specifically, using an array design with a periodic pattern can provide additional coupling abilities, hence the decision to study a nanometric structure featuring a nanoantenna array with subwavelength holes coupled to a solar cell.

In chapter 3, various diffraction theories are reviewed as well as some light-matter interactions in the subwavelength and optical domain, such as the generation of surface plasmon polaritons (SPP's) and the extraordinary optical transmission (EOT). It becomes clear that the classical diffraction theories do not comprise the existence of these subwavelength optical phenomena. Wave propagation theories such as the surface plasmon theory are currently the most accurate and appropriate manner to describe and understand the overall phenomenon. Although the use of optical nanoantennas to concentrate and amplify electromagnetic energy is a topic that has seen an increase in interest, it still lakes in depth studies regarding different designs, materials, and final applications. One of these applications is the coupling of optical nanoantennas into solar cells, to focus and increase radiation incident to the active area of the cell and, as a result generate more energy. This possibility is the focus of the work completed in the course of this dissertation.

Using *COMSOL Multiphysics*® software, different 2D and 3D solar cell structures were developed and described in detail in chapter 4. The subwavelength nanoantenna array that is implemented in all models is an aluminum (Al) nanoantenna, since this material type has shown promising results regarding the transmittance of light in orders of magnitude greater than predicted by standard aperture theory, mainly due to its complex dielectric function values. Several simulations were then carried out by implementing boundary probes in different sections

of each structure, to observe and assess how the optical response of such structures is influenced by the presence of a nanoantenna and if extraordinary optical transmission (EOT) occurs.

In chapter 5, the results of the simulations were demonstrated and analysed. Based on 2D and 3D simulation results regarding the a-Si solar cell structure, simulated from 5.1 to 5.2.1.1, it can be confirmed that EOT does always occur when an Al nanoantenna is present in the solar cell structure, which ultimately implies that these structures were able to transmit more light than its incidence. The results have also proven that this phenomenon is linked to the generation and propagation of SPP's, since high amplification and concentration of the electromagnetic field near the dielectric-metal interfaces is always verified, constituting clear evidence of the presence of surface plasmon polaritons. Additionally, an increase in absorption is noticeable when the nanoantenna is coupled to the cell, especially in the first layer (between boundary probe 1 and boundary probe 2). These results are quite promising since the more photons are absorbed by the cell, the more electron-hole pairs are generated by the photovoltaic effect, and more electric power will be made available by the cell, for a certain operation point. It is also noteworthy that in both 2D and 3D simulation scenarios, the obtained optical responses for the models with nanoantennas, showed peak normalized electric field values for incident wavelengths in the visible and infrared regions. These findings indicate that the implementation of nanoantennas in solar cells can be pertinent for applications using different parts of the light spectrum.

Furthermore, the influence that the position of the nanoantenna within the structure may have on the generated optical response was also studied. The results in 5.2.1.2 showed that the extraordinary transmission and field amplification were limited to the infrared section of the incident wavelength range, suggesting that the position of the nanoantenna in the structure can affect the light spectrum region where EOT takes place. This trait might prove to be useful for certain applications functioning at night or in places with little sunlight, since infrared radiation is still present.

The shape of the holes in the nanoantenna array can also have an impact in the optical response. Hence, this was a matter that was also examined by simulating a 3D model with conical holes in the nanoantenna instead of cylindrical (subchapter 5.2.1.2). The spectra obtained were, overall, quite similar to those obtained by the 3D model with a nanoantenna with cylindrical holes, except when it came to the normalized electric field values, mainly in boundary probe 1 located directly beneath the nanoantenna. In this first probe the model with cylindrical holes did present, for the entire wavelength range, higher electric field values signaling to the fact that EOT is more accentuated in this type of model, therefore leading to the conclusion that this type of hole geometry is perhaps unsuitable.

Additionally, simulation results were able to substantiate that the majority of the electric field absorption by the solar cell takes place in the intrinsic layer, as had already been speculated. The optical responses obtained for the models with an a-Si solar cell and with a PIN a-Si solar cell are analogous, with or without the implementation of the nanoantenna. Therefore, the decision made to proceed with simulations with a solar cell composed entirely of intrinsic a-Si is supported.

Finally, the impact that the coupling of a nanoantenna array could have in the optical response of a CIGS solar cell was also explored. The simulations illustrated underwhelming results regarding the occurrence of EOT in this particular model, where evidence of extraordinary transmission was only found in boundary probe 1 for a very small range of incident wavelength. Nevertheless, the field amplification that did occur was focused on the UV region of the light spectrum, which can prove useful for certain applications within that range of incident wavelength.

Overall, it was demonstrated that extraordinary optical transmission (EOT) does occur when an aluminum nanoantenna is coupled with a solar cell and, more importantly, that the structure produces promising results regarding field amplification and increase in absorption of photons throughout the solar cell. However, it is important to reference that the assessment of the results is somehow conditioned by the purpose of the structure in question. The intended results can vary, depending on the applications that the nanoantenna structure can have. In this dissertation, the study is focused on the integration of nanoantennas in solar cells to improve solar energy harvesting and, consequently, increase electric power production. Taking this into account, the original 3D a-Si solar cell structure with nanoantenna, characterised in subchapter 4.3.1, illustrated in figure 4.9, and simulated in subchapter 5.2.1.1, is the most suitable and optimized option for that specific purpose, since it presented field amplification along the entire incident wavelength spectrum and greater absorption of photons mainly in the first layer of the cell. Nevertheless, the remaining models that were studied presented slight variations that might prove useful under different conditions or for other applications.

6.1. Future Work

Nanoantennas constitute a crucial element in understanding the interaction of light with matter at a nanoscale. Although a great amount of research has been done regarding this matter in recent years, future growth requires more in-depth studies and experiments, involving different aspects of the devices such as materials, designs, and manufacture methods.

Depending on the intended application area, the approach to take regarding future work may vary. Focusing on the subject of this dissertation, the coupling of nanoantennas to solar cells, one of the topics that could be further investigated is the use of different nanoantenna designs and materials. Throughout this dissertation all the simulations considered a metallic aperture nanoantenna however, conducting an equivalent study using dielectric nanoantennas would be interesting and would allow to draw a comparison between the two kinds. As discussed in subchapter 2.4.2, dielectric materials are characterized by low dissipative losses in the optical range plus, materials like silicon have high permittivity values in the optical range, allowing electric and magnetic resonant responses which can lead to promising results when coupled with a solar cell.

Moreover, the study of imperfections and defects in the manufacture of nanoantennas for photovoltaic applications may also be of interest. The 3D model with a nanoantenna with conical holes, simulated in subchapter 5.2.1.3, could be included in this category since conical holes

could be interpreted as a manufacture defect in the development of cylindrical holes in nanoantennas.

Finally, all the simulated models were studied by resorting to the optical properties of the materials of each structure, to obtain the resulting electromagnetic field profile which was then analysed and discussed. In addition, it would be interesting to compute the optical power of the cell with and without the nanoantenna and compare the results, to ultimately evaluate the impact that the nanoantenna can have in the performance of the solar cell. Furthermore, by resorting to the semiconductor module of *COMSOL Multiphysics*® the electrical properties of the simulated models, such as certain currents or voltages, could be characterized. This would allow the estimation of the conversion efficiency of the cell, with and without the nanoantenna, which could also be used to evaluate and compare the performance of the cell in both situations.

References

[1] U. E. I. Administration, “International Energy Outlook 2019”, 2019.

[2] R. Castro, "Uma Introdução Às Energias Renováveis: Eólica, Fotovoltaica e Mini-hídrica", 2nd ed., IST- Instituto Superior Técnico, p. 309, 2012.

[3] D. K. Kotter, S. D. Novack, W. D. Slafer and P. Pinhero, “SOLAR NANTENNA ELECTROMAGNETIC COLLECTORS”, in *Proceedings of the 2nd International Conference on Energy Sustainability*, Jacksonville, Florida, USA, 2008.

[4] A. M. Sabaawi, C. C. Tsimenidis and B. S. Sharif, “Analysis and Modeling of Infrared Solar Rectennas”, *IEEE Journal on Selected Topics in Quantum Electronics,* vol. 19, no. 3, 2013.

[5] V. U. Hoffmann and A. Goetzberger, “What Is Photovoltaics?”, in *Photovoltaic Solar Energy Generation*, Spring, pp. 1-10, 2005.

[6] S. Thomas and A. Thankappan, “Introduction: Why Perovskite and Perovskite Solar Cells?”, in *Perovskite Photovoltaics: Basic to Advanced Concepts and Implementation*, Academic Press, pp. 1-24, 2018.

[7] J. A. Luceño-Sánchez, A. M. Díez-Pascual and R. P. Capilla, “Materials for Photovoltaics: State of Art and Recent Developments”, *International Journal of Molecular Sciences,* vol. 20, no. 4, 2019.

[8] S. P. Philipps, A. W. Bett, K. Horowitz and S. Kurtz, “CURRENT STATUS OF CONCENTRATOR PHOTOVOLTAIC (CPV) TECHNOLOGY,” 2015.

[9] A. W. Ho-Baillie, J. Hohl-Ebinger, D. H. Levi, E. D. Dunlop, Y. Hishikawa and M. A. Green, “Solar cell efficiency tables (version 54),” *Progress in Photovoltaics,* vol. 27, no. 7, July 2019.

[10] G. Conibeer, “Third-generation photovoltaics,” *materialstoday,* vol. 10, no. 11, November 2007.

[11] Y. J. Cheng, S. H. Yang and C. S. Hsu, “Synthesis of Conjugated Polymers for Organic Solar Cells Applications,” 2009.

[12] E. Spooner, “Organic Photovoltaics: An Introduction,” [Online]. Available: https://www.ossila.com/pages/organic-photovoltaics-introduction. [Accessed March 2020].

[13] E. Spooner, “Organic Photovoltaics vs 3rd-Generation Solar Cell Technologies,” [Online]. Available: https://www.ossila.com/pages/organic-photovoltaics-vs-3rd-gen-solar-tech. [Accessed March 2020].

[14] A. Fell, D. Walter and S. W. Glunz, “A fast and easy Perovskite solar cell simulation tool featuring ion migration,” 2017.

[15] L. E. Mundt, “High-Resolution Analysis of Perovskite Absorbers in Photovoltaics,” 2018.

[16] C. Hagendorf, M. Ebert, M. Raugei, D. Lincot, J. Bengoechea, M. J. Rodríguez and A. R. Lagunas, “Assessment of performance , environmental , health and safety aspects of First Solar's CdTe PV technology,” 2017.

[17] S. Weckend, A. Wade and G. Heath, “End-of-life management: Solar Photovoltaic Panels,” IRENA: International Renewable Energy Agency; IEA: International Energy Agency , 2016.

[18] P. Dias, S. Javimczik, M. Benevit, H. Veit and A. Moura Bernardes, “Recycling WEEE: Extraction and concentration of silver from waste crystalline silicon photovoltaic modules,” *Waste Management,* vol. 57, pp. 220-225, November 2016.

[19] M. S. Chowdhury, K. S. Rahman, T. Chowdhury, N. Nuthammachot, K. Techato, M. Akhtaruzzaman, S. K. Tiong, K. Sopian and N. Amin, “An overview of solar photovoltaic panels’ end-of-life material recycling,” *Energy Strategy Reviews,* vol. 27, January 2020.

[20] V. Savvilotidou, A. Antoniou and E. Gidarakos, “Toxicity assessment and feasible recycling process for amorphous silicon and CIS waste photovoltaic panels,” *Waste Management,* vol. 59, pp. 394-402, January 2017.

[21] F. Corcelli, M. Ripa, E. Leccisi, V. Cigolotti, V. Fiandra, G. Graditi, L. Sannino, M. Tammaro and S. Ulgiati, “Sustainable urban electricity supply chain - Indicators of material recovery and energy savings from crystalline silicon photovoltaic panels end-of-life,” *Ecological Indicators,* vol. 94, pp. 37-51, 2018.

[22] M. Gallo, L. Mescia, O. Losito, M. Bozzetti and F. Prudenzano, “Design of optical antenna for solar energy collection,” *Energy,* vol. 39, pp. 27-32, 2012.

[23] D. K. Kotter, S. D. Novack, W. D. Slafer and . P. J. Pinhero, “Theory and manufacturing processes of solar nanoantenna electromagnetic collectors,” *Journal of Solar Energy Engineering, Transactions of the ASME,* vol. 132, no. 1, pp. 141-149, 2010.

[24] B. Berland, “Photovoltaic Technologies Beyond the Horizon: Optical Rectenna Solar Cell,” Littleton, Colorado, 2001.

[25] L. Novotny and N. F. Van Hulst, “Antennas for light,” *Nature Photonics,* vol. 5, no. 2, pp. 83-90, 2011.

[26] A. M. A. Sabaawi, C. C. Tsimenidis and B. S. Sharif, “Infra-red nano-antennas for solar energy collection,” in *Loughborough Antennas and Propagation Conference*, Loughborough, UK, 2011.

[27] National Academy of Engineering, "Frontiers of Engineering: Reports on Leading Edge Engineering from the 1999 NAE Symposium on Frontiers of Engineering", 2000.

[28] M. Ameziane, “SOLAR NANOANTENNA ELECTROMAGNETIC”, 2015.

[29] R. Corkish, M. A. Green and T. Puzzer, “SOLAR ENERGY COLLECTION BY ANTENNAS,” *Solar Energy,* vol. 73, no. 6, pp. 395-401, 2002.

[30] S. Yan, B. Tumendemberel, X. Zheng, V. Volskiy, G. A. Vandenbosch and V. V. Moshchalkov, “Optimizing the bowtie nano-rectenna topology for solar energy harvesting applications,” *Solar Energy,* vol. 157, pp. 259-262, November 2017.

[31] L. Mescia and A. Massaro, “New Trends in Energy Harvesting from Earth Long-Wave Infrared Emission,” *Advances in Materials Science and Engineering,* 2014.

[32] I. S. Maksymov, “Magneto-plasmonic nanoantennas: Basics and applications,” *Reviews in Physics,* vol. 1, pp. 36-51, 2016.

[33] . Z. Zhu, S. Joshi, B. Pelz and G. Moddel, “Overview of optical rectennas for solar energy harvesting,” *Next Generation (Nano) Photonic and Cell Technologies for Solar Energy Conversion IV,* vol. 8824, 2013.

[34] W. T. Sethi, “Optical antennas for harvesting solar,” 2018.

[35] A. Krasnok, I. Maksymov, A. Denisyuk, P. Belov, A. Miroshnichenko, . C. Simovski and Y. S. Kivshar, “Optical nanoantennas,” *Physics-Uspekhi,* vol. 56, no. 6, pp. 539-564, 2013.

[36] B. Rolly, B. Stout and N. Bonod, “Boosting the directivity of optical antennas with magnetic and electric dipolar resonant particles,” *OSA Publishing,* 2012.

[37] Q.-H. Park, “Optical antennas and plasmonics,” *Contemporary Physics,* pp. 1-20, 2009.

[38] J. Wenger, “Aperture optical antennas,” *Optical Antennas,* pp. 369-386, 2014.

[39] F. J. Garcia-Vidal, L. Martin-Moreno, T. W. Ebbesen and L. Kuipers, “Light passing through subwavelength apertures,” *Reviews of Modern Physics,* vol. 82, no. 1, pp. 729-787, 2010.

[40] S. Grover and G. Moddel, “Applicability of Metal/Insulator/Metal (MIM) diodes to solar rectennas,” *IEEE Journal of Photovoltaics,* pp. 78-83, 2011.

[41] J. Alda, J. M. Rico-García, J. M. López-Alonso and . G. Boreman, “Optical antennas for nano-photonic applications,” *Nanotechnology,* vol. 16, no. 5, 2005.

[42] “Canon Science Lab,” Canon Global, [Online]. Available: https://global.canon/en/technology/s_labo/light/001/11.html. [Accessed 08 2020].

[43] M. Niaz, “Wave–Particle Duality: De Broglie, Einstein, and Schrödinger,” in *Critical Appraisal of Physical Science as a Human Enterprise*, pp. 159-165, 2009.

[44] B. Kapralos, M. Jenkin and E. Milios, “Acoustical diffraction modeling utilizing the Huygens-Fresnel principle,” in *IEEE International Workshop on Haptic Audio Visual Environments and their Applications*, Ottawa, Ont., Canada, 2005.

[45] R. A. Lameirinhas, J. P. N. Torres and A. Baptista, “Sensors Based on Nanoantennas: Fundamentals,” *European Journal of Applied Physics,* vol. 2, no. 3, 2020.

[46] A. Hamer, “The Double-Slit Experiment Cracked Reality Wide Open,” [Online]. Available: https://curiosity.com/topics/the-double-slit-experiment-cracked-reality-wide-open-curiosity/. [Accessed April 2020].

[47] R. D. F. R. Gomes, M. J. Martins, . A. Baptista and J. P. N. Torres, “Study of a nano optical antenna for intersatellite communications,” *Optical and Quantum Electronics,* vol. 49, no. 4, pp. 1-22, 2017.

[48] J. Weiner, “The physics of light transmission through subwavelength apertures and aperture arrays,” *Reports on Progress in Physics,* no. 6, 2009.

[49] L. Novotny and B. Hecht, "Principles of Nano-Optics", 2006.

[50] R. D. F. R. Gomes, “Estudo de uma antena ótica para comunicação inter-satélites,” 2016.

[51] W. L. Barnes, A. Dereux and T. W. Ebbesen, “Surface plasmon subwavelength optics,” *Nature,* vol. 424, no. 6950, pp. 824-830, 2003.

[52] T. Kalkbrenner, U. Håkanson, A. Schädle, . S. Burger, C. Henkel and V. Sandoghdar, “Optical microscopy via spectral modifications of a nanoantenna,” *Physical Review Letters,* vol. 95, no. 20, pp. 1-4, 2005.

[53] H. A. Atwater and A. Polman, “Plasmonics for improved photovoltaic devices,” *Nature Materials,* vol. 9, no. 10, pp. 205-213, 2010.

[54] T. W. Ebbesen, H. J. Lezec, H. F. Ghaemi, T. Thio and . P. A. Wolff, “Extraordinary optical transmission through sub-wavelength hole arrays,” *Nature,* vol. 391, no. 6668, pp. 667-669, 1998.

[55] “Electrical 4 U,” 1 April 2020. [Online]. Available: https://www.electrical4u.com/solar-cell/. [Accessed 15 May 2020].

[56] I. Massiot, “Design and fabrication of nanostructures for light-trapping in ultra-thin solar cells,” Paris, 2013.

[57] J. M. T. Pereira and J. P. N. Torres, “Frequency Response Optimization of Dual Depletion InGaAs/InP PIN Photodiodes,” *Photonic Sensors,* vol. 6, no. 1, pp. 63-70, 2016.

[58] S. Shamim, S. Islam, A. A. Jobair and H. Fazlul , “Design, performance analysis and efficiency optimization of copper indium gallium selenide (CIGS) solar cell,” *European Scientific Journal,* vol. 11, no. 6, pp. 156-163, 2015.

[59] Comsol, “multiphysics cyclopedia: The finite element method (FEM),” 21 February 2017. [Online]. Available: https://br.comsol.com/multiphysics/finite-element-method. [Accessed 07 2020].

[60] E. J. Dickinson, H. Ekström and E. Fontes, “COMSOL Multiphysics®: Finite element software for electrochemical analysis. A mini-review.,” *Electrochemistry Communications,* vol. 40, pp. 71-74, 2014.

[61] Comsol Multiphysics, “Wave Optics Module User’s Guide,” 2018.

[62] W. Frei, “COMSOL Blog: Guide to Frequency Domain Wave Electromagnetics Modeling,” Comsol, June 2015. [Online]. Available: https://br.comsol.com/blogs/guide-to-frequency-domain-wave-electromagnetics-modeling/. [Accessed July 2020].

[63] P. Arora, “MULTIPHYSICS SIMULATION OF PV MODULES,” Lisbon, 2016.

[64] “RefractiveIndex.INFO: Refractive index database,” [Online]. Available: https://refractiveindex.info/. [Accessed September 2020].

[65] R. A. M. Lameirinhas, J. P. N. Torres and A. Baptista, “A Sensor Based on Nanoantennas,” *MDPI: applied sciences,* 2020.

[66] S. Shongwe and M. Hanif, “Comparative Analysis of Different Single-Diode PV Modeling Methods,” *IEEE Journal of Photovoltaics,* vol. 5, no. 3, pp. 938-946, 2015.

[67] “Best Research-Cell Efficiency Chart,” [Online]. Available: https://www.nrel.gov/pv/cell-efficiency.html. [Accessed March 2020].

[68] W. Chen, “Characterization of new materials for capacitor formation in integrated circuit technology,” *The Boolean,* pp. 34-39, 2010.

[69] . N. S. Sariciftci, C. J. Brabec and J. C. Hummelen, “Plastic Solar Cells,” *Advanced Functional Materials,* vol. 11, no. 1, 2001.

[70] E. KLUGMANN-RADZIEMSKA , “CURRENT TRENDS IN RECYCLING OF PHOTOVOLTAIC SOLAR CELLS AND MODULES WASTE,” *Chemistry-Didactics-Ecology-Metrology,* pp. 89-95, 2013.

[71] A. Sharma, V. Singh, T. L. Bougher and B. A. Cola, “A Carbon Nanotube Optical Rectenna,” Atlanta, Georgia, USA, 2015.

[72] G. Moddel and S. Grover, "Rectenna Solar Cells", pp. 246-247, 2013.

[73] F. J. González and G. D. Boreman, “Comparison of dipole, bowtie, spiral and log-periodic IR antennas,” *Infrared Physics and Technology,* vol. 46, no. 5, pp. 418-428, 2005.

[74] E. T. Hashim and A. A. Abbood, “Temperature Effect on Photovoltaic Modules Power Drop,” *Al-Khawarizmi Engineering Journal,* vol. 11, no. 2, pp. 62-73, 2015.

[75] Fraunhofer Institute for Solar Energy Systems, ISE, “Photovoltaic Report,” September 2020.

[76] . G. M. Albuquerque, “Theoretical limit for efficiency of silicon solar cells: The Shockley-Queisser Limit and Beyond”, 2019.

Appendix A

A.1 Solar Cell Model and Parameters

A current-voltage characteristic curve (I-V curve) is a graphic representation of the relationship between the voltage applied to a certain electronic device and the current flowing through it. Crucial properties of an electronic device can be extracted from the shape and details of the curve, giving great insight about the operation of the device.

In order to define the I-V curve of a solar cell it is necessary to represent the cell by means of a circuit equivalent model. The most adopted model is the single diode model, represented in figure A.1.

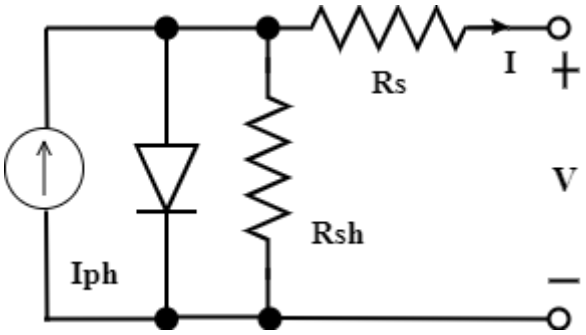

Figure A. 1 - Equivalent circuit for a single-diode model.

The relationship between the current and the voltage at the terminal of a PV solar cell can be represented by equation A.1

$$I = I_{ph} - I_0 \left[exp\left(\frac{V + IR_s}{N_s V_t}\right) - 1 \right] - \frac{V + IR_s}{R_{sh}} \quad \text{(A.1)}$$

where I is the model current, V is the model voltage, I_{ph} is the photogenerated current, I_0 is the diode reverse saturation current, R_s is the series resistance, R_{sh} is the shunt resistance, N_s is the number of series connected cells in the module and V_t is the junction thermal voltage [66]. V_t is defined by A.2

$$V_t = \frac{k * A * T}{q} \quad \text{(A.2)}$$

where k is the Boltzmann's constant equal to $1.38\ x\ 10^{-23}$ J/K, q is the electron charge equal to $1.602\ x\ 10^{-19}$ C, and A is the diode ideality constant [66].

The parameters I_{ph}, I_0, R_s , R_{sh} , and A can be obtained using different estimation methods. N_s is always easily available in PV module datasheets, valid under STC[8] (standard test conditions). To estimate the five parameters, one must consider three different modes of operation of a solar cell: open-circuit condition, short-circuit condition and maximum power point [66].

In the **open-circuit condition** the PV module terminals are not connected, meaning that the output current is zero and the generated voltage by the cell under STC, open-circuit voltage (V_{oc}), is at its highest at this point. On the other hand, in the **short-circuit condition** the PV module terminals are connected, meaning that the generated voltage is zero and the current flowing across the cell under STC, short-circuit current (I_{sc}), is at its highest at this point. Finally, at the **maximum power point** operation mode, the current flowing across the PV module is equal to I_{mp} and the generated voltage is equal to V_{mp}. P_{mp} is the maximum power that can be delivered by the cell under STC and the point in the I-V curve in which the maximum power is reached is called the maximum power point (MPP) [66].

$$P_{mp} = V_{mp} * I_{mp} \quad \text{(A.3)}$$

In figure A.2, the characteristic curves I-V and P-V of a mono-crystalline silicon solar cell are represented, along with the most relevant points obtained from it, such as the V_{oc}, I_{sc}, V_{mp}, I_{mp} and M_{PP} .

[8] STC stands for standard test conditions:
Cell temperature: θ^r=25°C
Incident irradiance on the cell: G^r=1000 W/m^2
Spectral distribution of solar radiation: AM 1.5

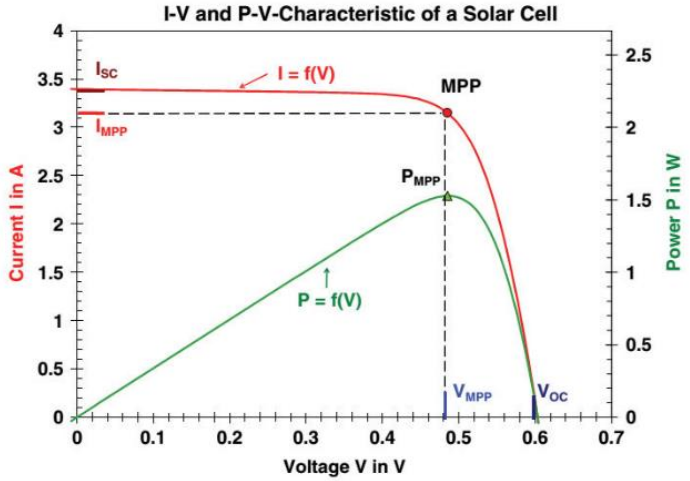

Figure A. 2 - Characteristic curves I-V and P-V of a mono-crystalline silicon solar cell with a cell area of 102m^2, under STC conditions (Adapted from [74]).

Other important parameters can be calculated from the I-V and P-V curves of a solar cell. The **fill factor (FF)** represents the relation between the I_{sc}, V_{oc}, V_{mp} and I_{mp} and is defined by A.4. This parameter can provide information about the quality of the cell, with typical values around 0.7 and 0.8, the closer the value is to 1 the more power the cell can provide.

$$FF = \frac{I_{mp} * V_{mp}}{I_{sc} * V_{oc}} \tag{A.4}$$

The efficiency of the cell is another parameter that can be obtained using information

from the I-V curve. The efficiency is defined by equation A.5 where A_{cell} is the cell's area and G is the value of the irradiance.

$$\eta = \frac{I_{mp} * V_{mp}}{A_{cell} * G} \tag{A.5}$$

Appendix B

B.1 Complex Refractive Index

In this appendix the complex dielectric functions of the materials that constitute the different layers of the CIGS solar cell are presented. The complex refractive index function $(n + ik)$ of ZnO, Cds, CIGS and Mo are represented in figures B.1, B.2, B.3 and B.4, respectively. As previously mentioned, n is the refractive index and k the extinction coefficient. The refractive index is indicative of the phase velocity, *i.e.,* the rate at which the wave propagates in a certain medium, and the extinction coefficient is directly proportional to the absorption coefficient.

The window plot in each function was adjusted to the wavelength simulation range, *i.e.,* $[250\ 1500]$ nm, to display the wavelength values that are going to influence the simulations. The models used for each material are retrieved from an online database [64], which presents the same models as the ones available on *COMSOL Multiphysics*®.

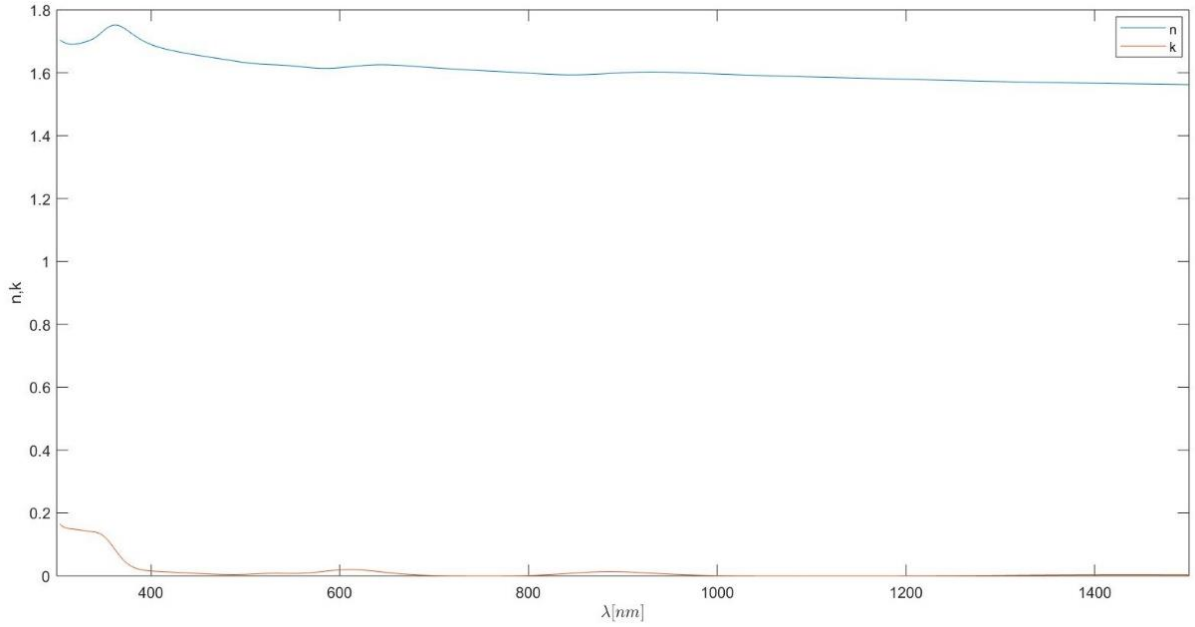

Figure B. 1 – Complex refractive index function of zinc oxide (ZnO).

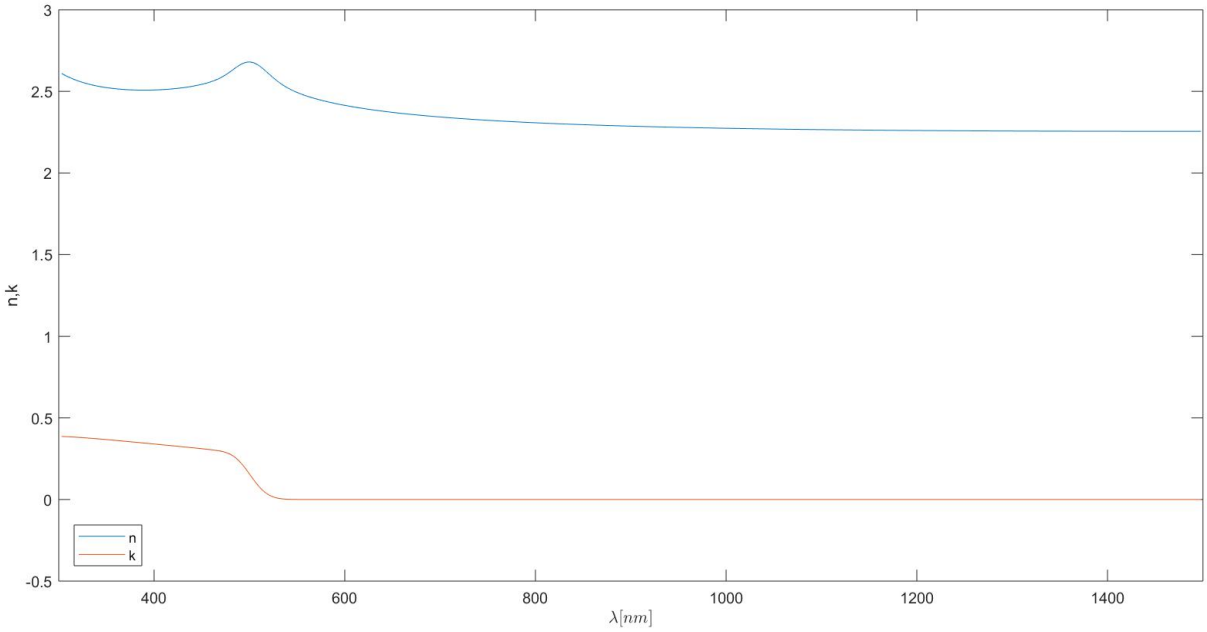

Figure B. 2 - Complex refractive index function of cadmium sulphide (Cds).

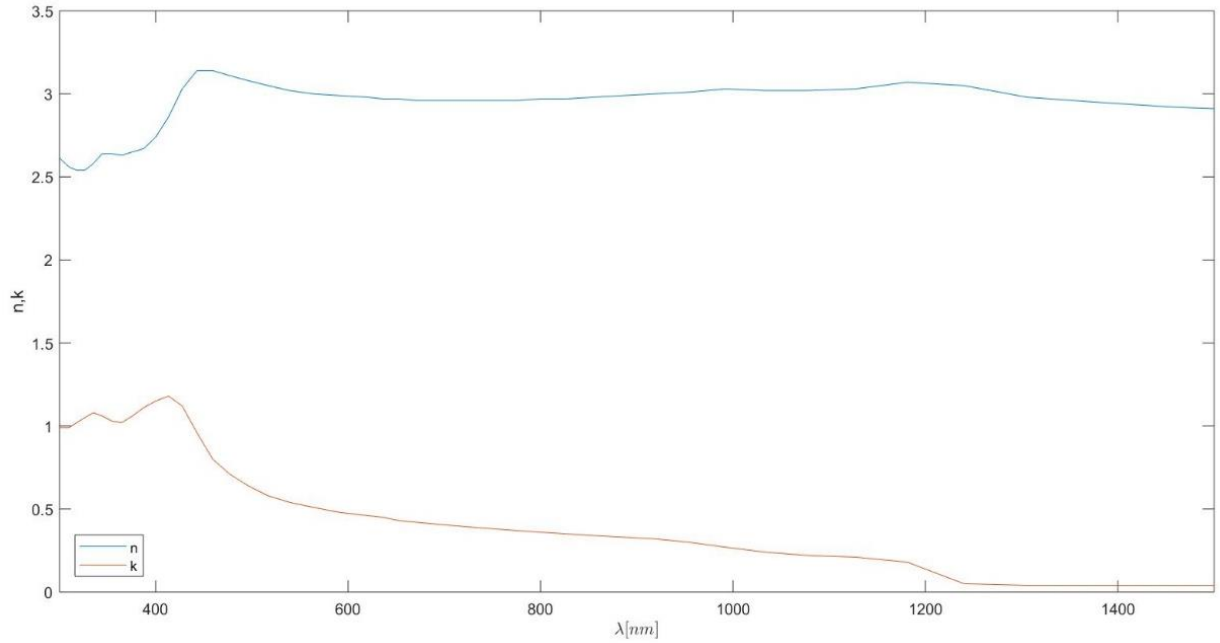

Figure B. 3 - Complex refractive index function of copper indium gallium selenide (CIGS).

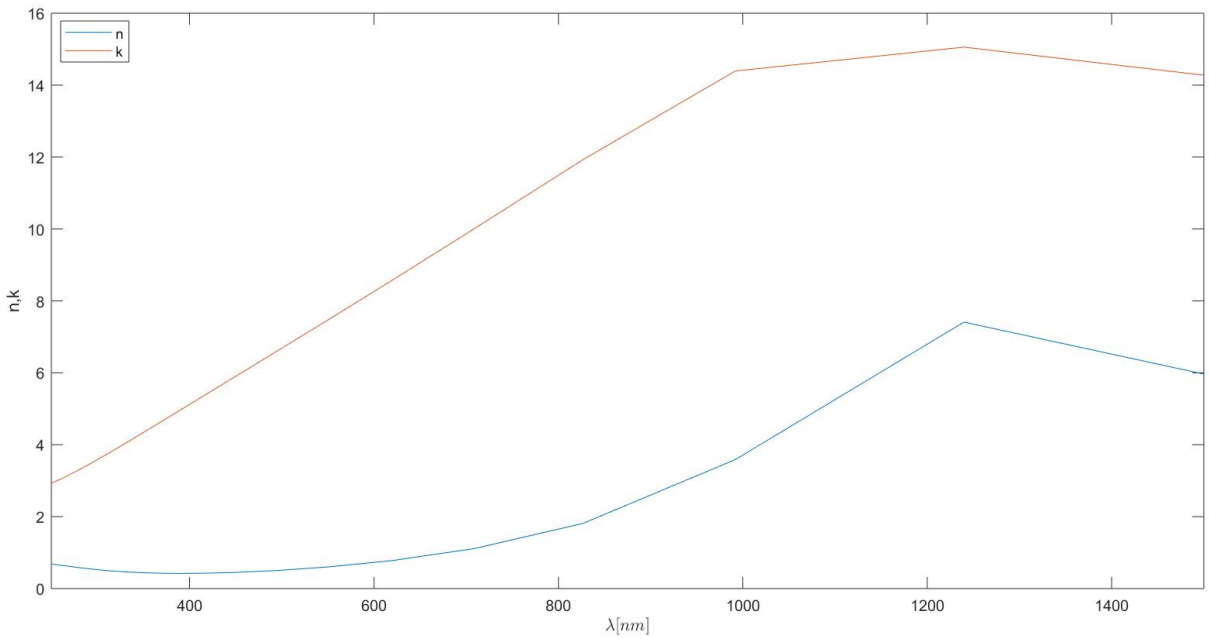

Figure B. 4 - Complex refractive index function of molybdenum (Mo).